Improved Wideband Spectrum Sensing Methods for Cognitive Radio

by

Yasin Miar

M.Sc., Amirkabir University of Technology (Tehran Polytechnic), 2002

A thesis submitted to the Faculty of Graduate Studies and Research

in partial fulfillment of the requirements for the degree of

Doctor of Philosophy in

Electrical and Computer Engineering

Ottawa-Carleton Institute for Electrical and Computer Engineering

School of Electrical Engineering and Computer Science

University of Ottawa

Ottawa, Ontario, Canada

September 24, 2012

Abstract

Cognitive Radio (CR) improves the efficiency of spectrum utilization by allowing non-licensed users to utilize bands when not occupied by licensed users. In this thesis, we address several challenges currently limiting the wide use of cognitive radios. These challenges include identification of unoccupied bands, energy consumption and other technical challenges. Improved accuracy edge detection techniques are developed for CR to mitigate both noise and estimation error variance effects. Next, a reduced complexity Simplified DFT (SDFT) is proposed for use in CR. Then, a sub-Nyquist rate A to D converter is introduced to reduce energy consumption. Finally, a novel multi-resolution PSD estimation based on expectation-maximization algorithm is introduced that can obtain a more accurate PSD within a specified sensing time.

Acknowledgments

First and foremost I would like to express my deep gratitude and sincere thanks to my supervisors, Dr. Tyseer Aboulnasr and Dr. Claude D'Amours, for their immense guidance, support, and encouragement during the course of my thesis. Moreover, my gratitude goes to Dr. Abbas Yongacoglu for all his guidance and support during my graduate studies. Thanks to them, I learned the skills necessary to conduct research in a professional manner. This work would not have been possible without their continuous direction and feedback.

I am thankful to the members of the examining board of my thesis, Dr. Saeed Gazor of Queen's University, Dr. Ian Marsland of Carleton University, Dr. Eric Dubois and Dr. Martin Bouchard of University of Ottawa, for their helpful comments and suggestions.

I would also like to extend my thanks to all of my friends especially Dr. Reza Yazdani, Dr. Arash Shokrani, Ms. Shabnam Mizani, Ms. Kimia Ansari, Dr. Sebastian

Szyszkowicz, Dr. Hadi Baligh, Dr. Alireza Mirzaee, Mr. Nerva Joachim, Mr. Kaveh Shahbaz, Ms. Saideh Ashtarifar, Mr. Amir Afrasiabi, Dr. Mehdi Fallahpour, and Dr. Hamid Ebrahimzad who have provided me with invaluable assistance, support, and inspiration throughout the course of my studies.

Last, and definitely most, I want to thank my family, especially my lovely parents. Although they were not here, their encouragement, support, and many sacrifices have allowed me to reach this stage in my life.

.

This work was supported by Natural Sciences and Engineering Research Council (NSERC) of Canada.

To my lovely Family

Contents

List of Tables

List of Figures

List of Acronyms

ADC	Analog to Digital Converters
CAF	Cyclic Autocorrelation Function
CCC	Common Control Channel
CDMA	Code Division Multiple Access
CR	Cognitive Radio
CS	Compressive Sensing
CWT	Continuous Wavelet Transform
DFT	Discrete-time Fourier Transform
EM	Expectation-Maximization
FCC	Federal Communications Commission
FFT	Fast Fourier Transform
MTM	Multi-Taper Method
MUSIC	MUltiple SIgnal Classification
OMP	Orthogonal Matching Pursuit
SNR	Signal to Noise Ratio

UWB	Ultra Wide Band
WiMax	Worldwide Interoperability for Microwave Access

Chapter 1

Introduction to Cognitive Radio and Wideband Spectrum Sensing

The ever-increasing demand for wireless communications has created a scarcity of available spectrum that can be licensed for use by these applications. While most portions of the spectrum have been licensed to different services such as radio, TV, satellite services and so on, the assigned licensed spectrum has not been utilized efficiently. The Federal Communications Commission (FCC) has released a report showing that the licensed spectrum is underutilized even in a dense urban environment [1]. For instance, measurements taken in downtown Berkeley show spec- trum utilization of around 30% below 3 GHz, and 0.5% in 3-6 GHz frequency range [2]. Figure 1.1 presents spectrum utilization measurements averaged over 6 different locations [3] showing that most of the licensed spectrum is underutilized. This inefficient use of

licensed spectrum coupled with the huge demand for wireless services have motivated researchers to find methods that will increase spectrum utilization efficiency.

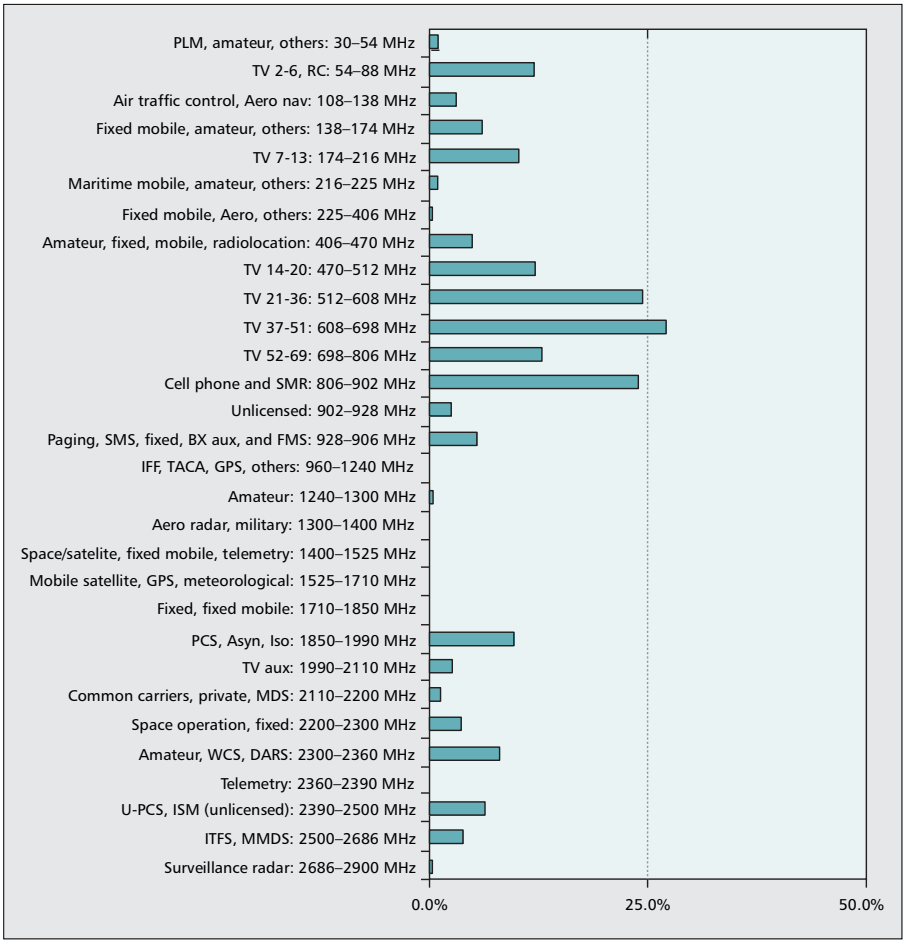

Figure 1.1: Spectrum occupancy measurements averaged over 6 locations [3].

Mitola proposed Cognitive Radio (CR) in [4] as a means of allowing unlicensed users to share underutilized spectrum with licensed users in order to improve licensed

spectrum utilization. CR is a software-defined radio system that adapts its parameters such as transmission frequency, power, modulation type, etc based on real time assessment of its spectral environment [4, 5, 6, 7]. CR users are secondary users coexisting in the frequency band of licensed users (primary users), when the frequency band is unoccupied by the primary users provided that they do not cause noticeable interference to the primary users communication.

The first standard based on cognitive radio is IEEE 802.22 [8] that shares the digital TV bands to provide Internet access for rural areas [9]. Worldwide Interoperability for Microwave Access (WiMAX) users operate in the 3 to 10 GHz band. Ultra Wide band (UWB) cognitive radios also operate in that band using the detect-and-avoid algorithm [10]. In that algorithm, the CR user detects the vacant spectrum and avoids interference to the primary users. Thus, the key functionality of CR is spectrum sensing that detects unused or unoccupied subbands of spectrum called spectrum holes [11].

Conventional spectrum sensing methods [12, 13] can be categorized into three major groups [14]: Energy detection [15], cyclostationary feature detection, [16] and pilot detection [17]. In energy detection, the energy of the received signal in each subband is calculated, and then compared to a properly chosen threshold. If it is greater than the threshold, the subband is declared as occupied. Energy detection [15] is the simplest method that does not require any information about the primary user, but it requires the noise energy level information to set the threshold. Pilot

detection [17] detects the presence of the signal by synchronizing the receiver to the carrier of the received signal. Pilot detection is the optimal method when the information of the licensed signal is available. Cyclostationary feature detection [16] exploits the inherent periodicity in the modulated signal to detect the presence of the signal. Feature detection is much more complex and requires more sensing time to detect the signal. In this thesis, we focus on energy detection spectrum sensing.

1.1 Wideband Spectrum Sensing for Cognitive Radios

Although spectrum sensing is a problem that has been studied for decades, research in spectrum sensing techniques designed specifically for CR is in its infancy. One important characteristic of the signal received by the CR receiver is that the primary (licensed) signal spectrum occupancy is usually low. This inherent nature of primary signal spectrum, for instance, motivates us to find spectrum sensing methods specifically designed for lowly occupied wideband spectrum.

Consider the UHF television band which resides in the 470 to 806 MHz range. Each TV transmission requires 6 and 8 MHz for analog and digital transmission, respectively. The UHF TV can accommodate 56 analog or 42 digital UHF TV signals. However, the occupancy is usually far from the capacity. The goal of the CR user is to find the vacant subbands and must sense some or all of the 336 MHz range in

order to accomplish this.

To detect potential vacant subbands for opportunistic access of a CR user, wideband spectrum sensing is required for the following reasons:

- The determination of the underlying noise level is a challenge in energy detection techniques. When using wideband spectrum sensing, the most frequent level is declared to be the noise level based on the assumption that the primary signal spectrum is mostly vacant.

- In cooperative spectrum sensing, a CR user relies on information from other users who can detect bands inaccessible to this user. Wideband sensing allows CR users to detect multiple vacant subbands to share this information with other users.

Although, spectrum sensing has been well developed, its challenges in case of wideband spectrum sensing have not been well investigated. While a limited number of wideband spectrum sensing methods have been introduced so far [18, 19, 20, 21, 22, 23], this is still an active area of research. In [18], a multi- resolution technique is proposed while a multiband joint detection technique is developed in [19] using different thresholds for different subbands to optimize the performance. An optimal algorithm is proposed in [20] to improve the throughput of the sensor. In another work [21], the continuous wavelet transform is used to find the frequency edges of the estimated power spectral density (PSD). This work has some drawbacks when

various subbands exhibit very different signal strengths. In [22], multiple subbands of a wide band of interest are exploited to estimate the noise threshold necessary to decide if a band is occupied. In [23], a spectrum sensing algorithm is proposed to decrease the effects of energy leakage and adjacent channel interference by using multitap windowing and constant false-alarm-rate (CFAR) method.

1.2 Challenges in Wideband Spectrum Sensing

1.2.1 Wideband Spectrum Sensing System Model

Figure 1.2 shows the block diagram of a typical wideband spectrum sensor based on energy detection. The received signal is filtered by a bandpass filter with the bandwidth of interest and down-converted. After sampling with analog to digital converter (A/D), the N point segments of the received signal are converted to the frequency domain using N point DFTs. The PSD is then calculated by averaging the magnitude squared of the frequency bins over some consecutive segments using Welch's method [24, 25]. The transition between occupied and unoccupied spectrum and vice versa is called a spectrum edge. Spectrum edges are defined as the frequency where the PSD suddenly rises above the noise floor. Finally, depending on the level of energy in each subband, the decision is made on whether the subband is occupied or vacant.

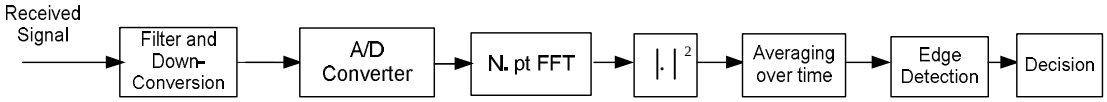

Figure 1.2: Wideband spectrum sensor block diagram.

In CR, the PSD is generally assumed to have the shape shown in Figure 1.3 where the PSD has areas of high concentration followed by areas where its power spectral density abruptly changes at the spectrum edges [21].

The key operation in the spectrum sensing model shown is the detection of the band edges in the PSD after first approximating it. It is shown in [21] that the edges can be detected by finding the local extrema of the first derivative of the Continuous Wavelet Transform (CWT) of the PSD with respect to frequency. Alternatively, the edges can be detected by differentiating the PSD with respect to frequency. Since the abrupt change in the PSD happens in the edge locations, the first derivative of the PSD exhibits local extremum at the edge locations.

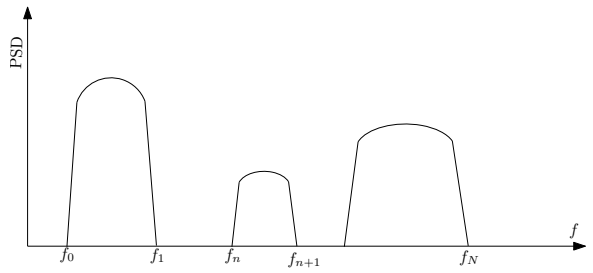

Figure 1.3: Frequency subbands with piecewise smooth PSD

1.2.2 Challenges in Wideband Spectrum Sensing

Some of the most important challenges of spectrum sensing are summarized below.

1.2.2.1 Effects of noise level and estimation error variance

In IEEE 802.22 [8], the FCC provided the required signal to noise ratio (SNR) levels for licensed users as -10 dB for wireless microphones and -22 dB for Digital TV (DTV) signals [26]. The sensing SNR can be as low as -35 dB for a CR sensor [2, Page 43]. This low SNR level makes noise determination a challenge for designing the spectrum sensing methods.

Moreover, most of spectrum sensing techniques suffer from the SNR wall problem [27]. SNR wall is defined as the SNR level below which the primary signal cannot be discriminated from noise even by increasing the sensing time.

In [27], it is shown that if the noise power is calculated exactly, the primary signal with any SNR can be detected by increasing the sensing time. However in reality, the noise power is approximated with some uncertainty leading to situations where the primary signal may not be detected and the band may be erroneously identified as unoccupied. On the other hand, the PSD estimation error variance causes fluctuations in estimated PSD. PSD estimation error variance is defined as the variance of the estimated PSD with respect to its actual value. Since, the estimation error variance is proportional to the signal strength, the stronger subbands show stronger ripples than the weaker ones. This effect may mislead the spectrum sensor so that the ripples

of the stronger subbands might be treated as edges of the PSD.

1.2.2.2 Complexity of PSD estimation for CR purposes

PSD estimation is an important step for spectrum sensing. In order to detect the vacant subbands, first the received signal is converted from time domain to frequency domain. The most widely used methods in PSD estimation are still DFT- based techniques [28], of which Welch's method is the most widely used one [24, 25, 14]. In Welch's method, the signal is split into segments. The PSD is then obtained via linearly averaging the periodogram of each windowed segment [25]. Another important PSD estimation method is Multitaper Method (MTM) [29]. In MTM PSD estimation, the periodograms are averaged not only along consecutive segments but also along various orthogonal tapers [30] within each segment.

In the context of CR, it is the location of the transition between occupied and vacant subbands that is important, rather than the exact detailed PSD. The location of the transition is referred to as PSD edges. This characteristic in CR can be considered to reduce the complexity of spectrum sensing methods for CR.

1.2.2.3 A/D conversion sampling rate

Normally, the band of interest is sampled at Nyquist rate to be processed by spectrum sensor. However, recall that for CR a typical wideband of interest may be as large as 336 MHz for the UHF TV band requiring a sampler of 672 Msps (Mega samples/sec).

This high sampling rate is a significant challenge in spectrum sensing.

Now, we take a look at the practical range of wideband A to D converters [31]. Flash converters can offer sampling rates of about 1 Gsps, but they consume higher power due to their parallel structure. With Sigma-Delta converters, the available sampling rate is less than 100 Msps. Because of their low power consumption, these A/D converters are suitable to be implemented in mobile CR devices [32], [33, Pages 99-126]. By decreasing the required sampling rates in CR, the lower power A/D converters can be utilized for spectrum sensing purposes.

Compressive sensing has been proposed in [34], [35] to address this challenge. Compressive sensing is a method by which a compressible signal is sampled at sub-Nyquist rates and is later reconstructed. A compressible signal is a signal that has very little information in time, frequency or another domain. Considering the lowly occupied nature of the signals frequency response in CR, compressive sensing may be successfully applied to the received signal leading to lower required sampling rates. In [36], the concept of compressive sensing has been applied to wideband spectrum sensing for various compression ratios.

1.2.2.4 Hidden node problem

Various network architectures have been suggested for CR platform including centralized and ad-hoc architectures depending on the presence or absence of a center to communicate to the CR users [37]. Moreover, the network can be categorized as

cooperative when information about spectrum holes is shared among all CR network [37, 38] and non-cooperative when each user independently identifies the spectrum holes.

The scenario of a hidden node problem is shown in Figure 1.4. The problem occurs when the CR device is under shadowing and/or severe fading from primary transmitter side. This misleads the spectrum sensor of the CR user and may result in an occupied subband being wrongly declared as vacant. The CR transmitter starts transmission in that subband interfering with the primary communication link.

To combat this problem, cooperative spectrum sensing has been developed [2, 37, 38]. Through cooperation, the users share the decision information with one another. Since the probability of having severe fading for multiple CR users simultaneously is much less than for a single user, this cooperation results in more accurate spectrum sensing at the expense of more complex communication protocol [2]. We do not address this challenge in the thesis.

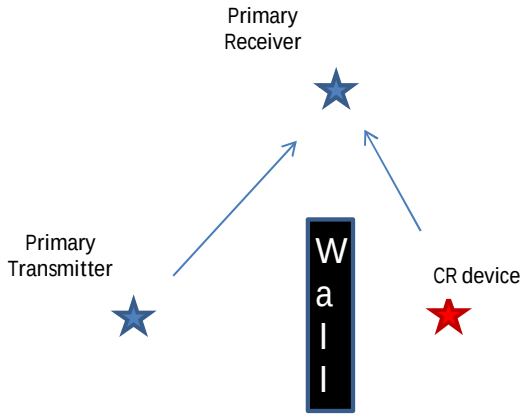

Figure 1.4: Hidden node problem scenario.

1.3 Organization of the Thesis and our Contributions

This thesis is organized as follows.

In Chapter 2 we review cognitive radio and spectrum sensing literature.

In Chapter 3, current spectrum edge detection techniques are reviewed. It is emphasized that current edge detection techniques, in certain conditions are not capable of accurately detecting spectral edges especially when the PSD levels in various subbands are very different. These signal level differences in different subbands cause higher estimation error variances in stronger subbands resulting in higher fluctuations in stronger subbands. We will show through simulation that in current edge detection techniques, these higher fluctuations maybe falsely detected as the presence of edges in certain conditions. To combat this problem, first we propose to apply the dB-scale values of PSD instead of linear scale values in current edge detection methods. We show that this modification results in almost the same estimation error variance in different subbands with various levels of energy. Then we propose a new edge detection method based on the window averaging of the estimated PSD that reduces the fluctuations. Simulation results show better performance for the proposed methods compared to the current edge detection methods. Some of the results from this part of research were presented in [39].

In Chapter 4, we consider methods for reducing the high computational complexity

of wideband spectrum sensing by introducing simplified DFT (SDFT)-based spectrum sensing methods. In the proposed methods, SDFT is proposed for time-to-frequency conversion process instead of DFT. SDFT-based PSD estimation techniques can be used to reduce the complexity of spectrum sensing methods. The SDFT techniques are less computationally complex than DFT techniques since no multiplications are required in the time-to-frequency domain transformation. Simulation results and mathematical analysis indicate that the performance of the SDFT-based spectrum sensing method is comparable to that of the DFT-based one especially when the received signal spectrum is mostly vacant. Some of the results from this part of research were presented in [40], [41].

In Chapter 5, it is proposed to apply sub-Nyquist non-uniform sampling for spectrum sensing to reduce the power consumption. We propose to estimate the missing samples due to sub-Nyquist A/D converter by applying the expectation-maximization (EM) algorithm [42, 43, 44]. It is shown that the combined subNyquist sampling and EM algorithm consumes less power than A/D converter at the Nyquist rate thus making the proposed algorithm a viable low- power solution for spectrum sensing. Moreover, it is shown by simulations that the proposed sub-Nyquist rate non-uniform sampler accurately detects the edges of the estimated PSD. We presented some of the results from this work in [44].

In Chapter 6, we propose a method based on expectation-maximization (EM) algorithm that allows both a better resolution and a lower estimation error variance for

the same observation (sensing) time. The idea is based on multi-resolution processing. Assuming the same number of received signal samples, first a PSD with higher resolution and thus higher estimation error variance is obtained. Using the same received signal samples, another PSD is estimated with lower estimation error variance but lower frequency resolution. The expectation-maximization (EM) technique is used to estimate the missing frequency bins of the lower resolution PSD using the PSD with higher resolution. It is shown by simulation that the proposed method improves both the resolution and estimation error variance. Thus the proposed method requires less sensing time than the conventional Welch's method to have a better estimation error variance. Simulation results show the ability of the proposed method to improve the edge detection performance. The results of this work are being considered for a patent application.

Finally, some concluding remarks and suggestions for future research are given in Chapter 7.

Chapter 2

Overview of Cognitive Radio and Spectrum Sensing Techniques

2.1 Overview of Cognitive Radio

Software-defined radio (SDR) [45] is a highly reconfigurable system that can change its parameters such as transmission power, modulation type, frequency of transmission, coding type and so on. SDR by itself is not aware of the environment, thus it can not change its parameters automatically and intelligently.

Cognitive radio is an SDR-based system that senses the environment and selects parameters accordingly. To exploit the unused portions of the licensed spectrum, CR senses the spectrum and adapts its carrier frequency and transmission power while causing negligible interference to the primary users.

The CR senses the environment via spectrum sensing functionality, and thus the spectrum holes are determined. Finally, the spectrum manager chooses some spectrum holes to exploit.

For spectrum sensing purposes, there is a silence period in which no CR is allowed to transmit in order not to be confused as primary radios. The spectrum management and silence period synchronization are major tasks that are controlled by Common Control Channel (CCC) within the Medium Access Control (MAC) layer [46, 47].

2.1.1 Performance Metrics

The following metrics are the most common metrics for spectrum sensing performance analysis:

- False alarm rate: P_{fa} is the probability of falsely declaring a subband to be occupied while it is in fact vacant.

- Misdetection rate: P_{md} is the probability of falsely declaring a subband to be vacant while it is in fact occupied by a primary user.

- Detection rate: P_d is the probability of declaring a subband to be occupied while it is actually occupied by a primary user. We have:

$$P_d = 1 - P_{md}. \tag{2.1}$$

The performance metrics are defined pictorially in Figure 2.1 over the PSD of a single subband. Similarly, the performance metrics for several subbands can be derived by accumulating the ones of each subband.

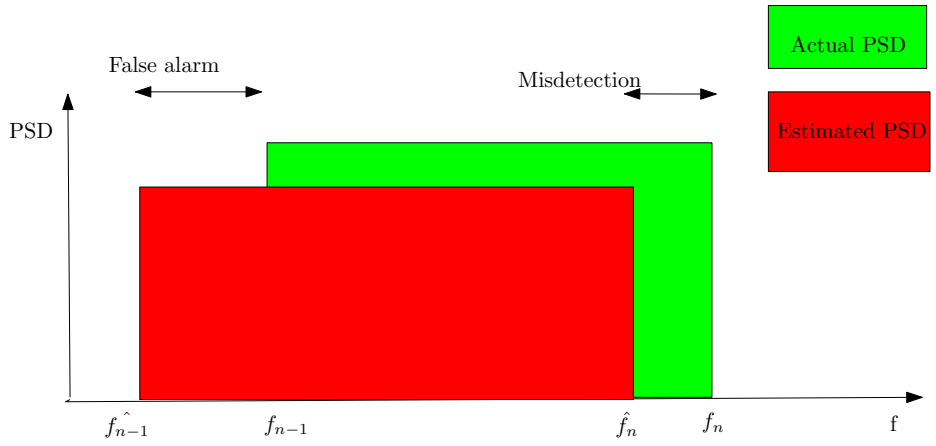

Figure 2.1: Performance metrics for a single subband.

2.2 Spectrum Sensing Methods

Spectrum sensing can be centralized or distributed. In centralized networks [48], the decision on spectrum holes is taken by a central agent, such as a base station or network controller. On the other hand, the spectrum sensing can be implemented in a distributed network [49, 50]. In this model, the decisions on the vacancy of the spectrum subbands are made at each CR node.

In terms of cooperation, spectrum sensing can be done in a cooperative way in which the spectrum hole decision information is shared among a group of CR nodes [51]. In non-cooperative method [52], each CR node decides on the spectrum status

independently. It has been shown that cooperative spectrum sensing is more powerful in combating the shadowing and fading effects especially due to hidden node problem at the expense of more complex networking protocol and longer communication delay [14].

Spectrum sharing techniques can be categorized into three different methods of underlay, overlay, and interweave spectrum sharing methods [53, 54]. In underlay spectrum sharing method [53], the secondary user can transmit under the noise level over a very wide band without sensing the presence of a primary user. It can be done with spread spectrum techniques such as code division multiple access (CDMA) [55]. Ultra wide band (UWB) techniques [56] are based on the underlay spectrum sharing techniques. In an overlay spectrum sharing method [53], the cognitive radio has some knowledge of primary user's signal. Using that knowledge, it combats the interference seen at cognitive and primary receivers. The cognitive user utilizes those information to relay the primary user's signal when required. Since having the knowledge of primary user signal is not easy, this method is not the best option for most of CR applications. In an interweave spectrum sharing method [53], the secondary user senses the spectrum to find the spectrum holes and transmits within the spectrum hole(s). In this thesis, our scenario is based on distributed non-cooperative interweave spectrum sensing method.

There are three major methods of spectrum sensing [14]: Energy detection [15], cyclostationary feature detection [16], [57] and pilot detection [17].

2.2.1 Energy Detection

In energy detection [14], [15], [25], the energy of the received signal in each subband is calculated, and then compared to a properly chosen threshold. If it is greater than the threshold, the subband is declared as occupied. Energy detection is the simplest method that does not require any information of the primary user, but it requires the noise energy level information to set the threshold.

The energy detection block diagram is shown in Figure 2.2. The received signal is filtered by a bandpass filter and down-converted. Then, the signal is transformed to frequency domain by DFT transformation. The magnitude squared of the signal in frequency domain is calculated. The energy of the signal is calculated by

$$T = \int |X(f)|^2 \, df, \tag{2.2}$$

where T is the energy of the received signal and $X(f)$ is the signal in frequency domain. The detection of the spectrum holes (white space) is highly related to appropriate choice of the threshold λ as follows:

$$\begin{aligned} T > \lambda \quad & \text{Primary signal is present.} \\ T < \lambda \quad & \text{Primary signal is absent.} \end{aligned} \tag{2.3}$$

The threshold level λ should be chosen above noise power as

$$\lambda \geq \sigma_n^2. \tag{2.4}$$

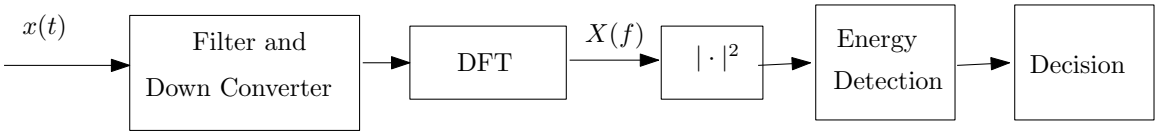

Figure 2.2: Energy detection block diagram.

The performance of the system is represented by the pair results of the probabilities of false alarm P_{fa} and detection P_d, which are derived for a single user as follows [58]:

$$P_{fa} = Q\left(\frac{\lambda - N\sigma_n^2}{\sqrt{2N\sigma_n^4}}\right). \tag{2.5}$$

$$P_d = Q\left(\frac{\lambda - N(\sigma_n^2 + \sigma_s^2)}{\sqrt{2N(\sigma_n^2 + \sigma_s^2)^2}}\right), \tag{2.6}$$

where $Q(\cdot)$ represents the Q function [59]. σ_n^2 and σ_s^2 are the variance of the noise and the signal respectively.

2.2.2 Cyclostationary Feature Detection

Feature detection [16], [57] exploits the inherent periodicity in the modulated signal to detect the presence of the signal. This fact can be exploited to detect the presence of the primary signals. Cyclostationary signals have periodic autocorrelation function of time.

The block diagram of feature detection technique is shown in Figure 2.3. The received signal is first filtered by a bandpass filter and down-converted. Then the cyclic autocorrelation function (CAF) of the signal $x(t)$ is calculated by

$$R_x(\tau, \alpha) = E[x(t+\tau)x(t-\tau)e^{-j2\pi\alpha t}], \tag{2.7}$$

where $E[\cdot]$ is the expected value function, and α is the cyclic frequency. The DFT of the CAF gives the cyclic spectrum $S(f, \alpha)$. The cyclic spectrum and CAF are two dimensional functions.

In the cyclic spectrum plane, the maximum of the cyclic frequency happens at the inherent frequency of the cyclostationary signal. Noise has the cyclic frequency with a peak at zero frequency. If the cyclic frequency is detected at a frequency other than zero, a primary signal is present.

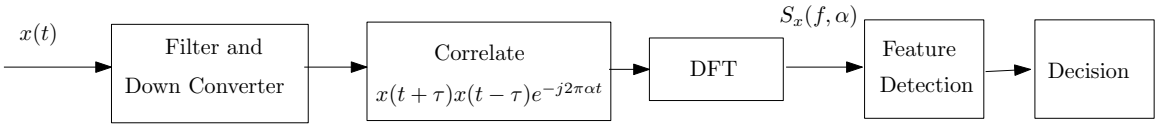

Figure 2.3: Feature detection block diagram.

Feature detection is much more complex and requires more sensing time to detect the signal.

2.2.3 Pilot Detection

Pilot detection (matched filter detection) detects the presence of the signal by correlating the received signal spectrum to its known carrier frequency. If the received signal spectrum is highly correlated to its known carrier frequency, the primary signal is most probably present.

The drawback of applying pilot detection in CR is that in CR, the information of the primary signal is not always available. Still, it can be applied to specific applications such as detecting the presence of digital TV signals.

Pilot detection is the optimal method when the information of the licensed signal is available.

2.3 Non-Parametric Methods of Power Spectral Density Estimation Techniques

In non-parametric methods, the PSD can be obtained by observing the finite samples of the signal itself. The most common techniques are periodogram [25], Welch's method [24, 25], or the multi-taper method (MTM) [29, 25]. These methods are the simplest methods of PSD estimation, and thus are proposed for PSD estimation in CR [14, 29].

2.3.0.1 Periodogram

The periodogram of an N-point segment of the signal can be calculated as

$$\mathbf{S_m} = \frac{|\mathbf{X_m}|^2}{N} \tag{2.8}$$

where $\mathbf{S_m}$ is the m^{th} segment's periodogram and $\mathbf{X_m}$ is the DFT of the signal.

The PSD is obtained over a finite number of samples N, which is equivalent to applying a rectangular window over an infinite number of samples in the time domain. This windowing effect causes spectral leakage. Increasing the window length results in a narrower spectral response, and thus less spectral leakage. Moreover, increasing the length of the window results in a higher frequency resolution [25].

Periodogram is an asymptotically unbiased estimator; because, as the window length tends to infinity, the rectangular window spectral shape tends to a Dirac delta function. Therefore, as the window length increases, the estimator mean tends to the actual mean of the PSD. However, periodogram is an inconsistent estimator of the PSD due to the fact that its estimation error variance does not tend to zero as the window length tends to infinity [25].

2.3.0.2 Welch's Method

In order to combat the inconsistency problem of periodogram, Welch proposed a method of averaging periodograms to estimate PSD. In Welch's method [24], the

PSD is achieved by linearly averaging the periodograms of all segments given by

$$\mathbf{S} = \frac{1}{M} \sum_{m} \mathbf{S_m}, \tag{2.9}$$

where M is the number of segments contributing in Welch's method and $\mathbf{S_m}$ is the m^{th} segment's periodogram.

Welch's method is also asymptotically unbiased as its mean tends to the actual mean by increasing the number of segments and samples. Its variance tends to zero as the number of segments goes to infinity due to the fact that the estimator variance is inversely proportional to the number of segments. This makes Welch's method a consistent estimator.

In order to decrease the effects of spectral leakage due to rectangular windowing, other windows such as Hanning, Hamming, Kaiser, etc. have been used [25]. These windows offer lower spectral leakage at the expense of information loss at the edges of the window. To mitigate the effects of information loss due to windowing, the overlapping segments averaging has been proposed. In case of overlapping Welch's method, the number of segments M is given by [60]

$$M = 1 + (N_t - N)/(N - N_p), \tag{2.10}$$

where N_t is the total number of samples, N is the number of samples in each segment, and N_p is the number of overlapping samples between consecutive segments. In

overlapping methods, 50% of overlapping is the often preferred.

2.4 Edge Detection

The second step in wideband spectrum sensing after PSD estimation is to detect the PSD edges (the starting/ending points of the vacant subbands). The PSD level changes abruptly at the PSD edges. Edge detection techniques have been used in many applications of signal processing notably in image processing in which an edge is the point where the image brightness changes abruptly. These discontinuities of the signal can be treated as an edge.

A simple method of detecting an edge of a signal is to take its first derivative. The edges are located at the local extrema of the first derivative or the zero-crossings of the second derivative. A typical edge and its first derivative are shown in Figure 2.4 where the edge can be seen at the local maxima of the first derivative of the signal. We will see that the first derivative is simply a Haar wavelet transform at the first level. Thus wavelets are important tools to detect the edges. By choosing an appropriate wavelet function, the wavelet transform can represent the sharp transitions in terms of different dilated and scaled versions of the wavelet function.

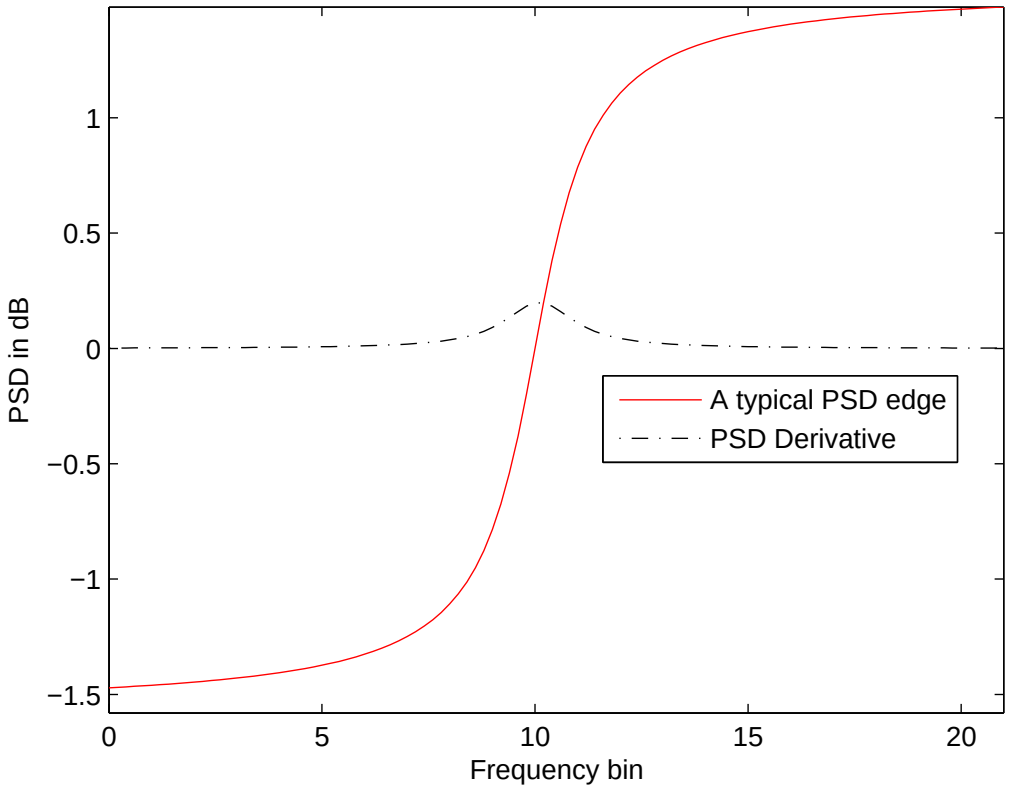

Figure 2.4: A typical edge in the PSD of a signal and its associated derivative.

2.5 Compressive Sensing

It has been proven that if the signal is (nearly) sparse in some domain (time, frequency, wavelet, etc.), it can be sampled with sub-Nyquist rates by applying compressive sampling [34, 35]. A signal vector is nearly sparse when most of its elements have small magnitudes while only a few of its elements have large magnitudes. If a signal vector is sparse in some domain, it can be represented in terms of a few basis functions in that domain. For example, a Kronecker delta function which has only one non-

zero value in the time domain, is represented by an infinite number of values in the frequency domain. Therefore, a Kronecker delta function is sparse in the time domain.

A Nyquist rate sampled signal $x(t)$ is represented in the time domain by N samples as $\{x(n)|_{n=0,\cdots,N-1}\}$. We have

$$x(t) = \sum_n \psi(t-n)x(n), \tag{2.11}$$

where $\psi(\cdot)$ represents the sampling function. The sampling function in the time domain is periodic train of Kronecker delta function as follows:

$$x(t) = \sum_n \delta(t-n)x(n). \tag{2.12}$$

In another domain, it may be represented by

$$y_k = < \mathbf{x}, \varphi_{\mathbf{k}} > \quad k = 0, \cdots, P-1, \tag{2.13}$$

where $< \cdot, \cdot >$ is the inner product operand and y_k is the signal value component obtained by projecting the signal in the direction of the basis vector $\varphi_{\mathbf{k}}$. In matrix form, we have

$$\mathbf{y} = A \cdot \mathbf{x}, \tag{2.14}$$

where A is a $P \times N$ sensing matrix consisting P bases ($P \preceq N$) and is given by

$$A = \begin{pmatrix} \varphi_{\mathbf{1}}^{*} \\ \varphi_{\mathbf{2}}^{*} \\ \vdots \\ \varphi_{\mathbf{P}}^{*} \end{pmatrix}. \tag{2.15}$$

The relation in Equation 2.14 is ill-posed, and thus there are many solutions. But, it is assumed that the signal vector y in (2.14) is nearly sparse. Therefore, the answer to the relation results in a minimum in the signal's l_1 norm [34, 35]. l_1 norm is defined as

$$||\mathbf{x}||_{l_1} = \sum_i |x_i|. \tag{2.16}$$

The following relation exists between the cardinality of the signals in two domains [34, 35].

$$P \geq 4 \cdot \mu^2 \cdot S \cdot \log N, \tag{2.17}$$

where S represents the sparsity of the signal, and μ is the coherence coefficient that represents the coherence between two domains given by

$$\mu = \sqrt{N} \cdot \max_{k,j} | < \varphi_{\mathbf{k}}, \psi_{\mathbf{j}} > | \tag{2.18}$$

where $\varphi_{\mathbf{k}}$ is the basis functions in the transformed domain and $\psi_{\mathbf{j}}$ is the sampling

basis functions that can be Kronecker delta functions. The lower the incoherence, the less number of samples are required.

By applying compressive sampling, a sparse signal which is represented by N samples in the time domain and is represented by $P \preceq N$ samples in another domain, can be reconstructed even by sampling with sub-Nyquist rates; i.e. by $P \preceq N$ samples [34, 35].

Chapter 3

New Spectrum Edge Detection Techniques in Wideband Spectrum Sensing of Cognitive Radio

3.1 Introduction

The first step in spectrum sensing is power spectral density (PSD) estimation. Discrete Fourier transform (DFT)-based PSD estimation methods are the most widely used [28]. Welch's method [24],[25] is an example of DFT-based PSD estimation. It is proposed for spectrum sensing for CR in [14].

The second step in spectrum sensing is to detect the PSD edges. PSD edges are the start and end points of unused subbands. To simplify the analysis, as is done

in [21], it is assumed that the PSD of the received signal in CR has a piecewise rectangular-like shape as is shown in Figure 1.3. In [21], the edges are detected as the local extrema of the first derivative of the product of various scales of continuous wavelet transform (CWT) of the PSD with respect to frequency. Alternatively, the edges can be detected by locating the local extrema of the first derivative of the PSD with respect to the frequency.

The spectrum of the signal received by secondary user (SU) consists of subbands with various energy levels. In the process of PSD estimation, the stronger subbands exhibit higher estimation error variances leading to more fluctuations in those subbands [25]. The estimation error variance is the variance of the estimated PSD around its actual PSD values. By applying the current wavelet-differentiation-based methods in edge detection [21], these fluctuations may be detected as edges resulting in an incorrect decision on the location of the edges. Conversely, if the received power from an occupied subband is low, the edges may be obscured by noise and difficult to detect. Therefore, there is a need for new techniques that mitigate the effects of estimation fluctuations and low-level primary users on the performance of edge detection.

In this chapter, the current edge detection methods are modified by applying the dB-scale values of estimated PSD instead of linear values. It is shown that the variance of the dB-scale values of estimated PSD does not change significantly by an increase in the level of energy in the subbands while the variance of the linear scale

values of the estimated PSD is proportional to the level of energy in each subband [25] resulting in stronger fluctuations in the stronger subbands.

Next, it is proposed to apply a normalization technique to mitigate the effects of fluctuations in PSD edges. Normalization reduces the fluctuations due to noise and estimation error variance. This method is called window-normalization based edge detection technique.

Finally, we propose a method that smooths the fluctuations and detects the noise level. First by averaging the PSD over a window, the PSD fluctuations are smoothed. Then, the integer part of the filtered PSD is taken for smoother PSD. A change in the level of the integer part of window-averaged PSD may indicate the presence of an edge in the PSD. The most frequent level is considered to be the noise level. This method is called window-averaging based edge detection technique. Simulation results show better performance for the proposed method compared to the current wavelet-differentiation-based edge detection methods.

3.2 Spectrum Edge Detection System Model

In Welch's method, the received signal samples are segmented into M segments of length N. The estimated PSD (S) is achieved by linearly averaging the periodograms of all segments as

$$\mathbf{S} = \frac{1}{M} \sum_{m} \mathbf{S_m}, \tag{3.1}$$

where $\mathbf{S_m}$ is the m^{th} segment's periodogram. The periodogram of each segment is given by

$$\mathbf{S_m} = \frac{|\mathbf{X_m}|^2}{N}, \tag{3.2}$$

where $\mathbf{X_m}$ is the DFT sequence of the m^{th} segment. $|\cdot|^2$ is an element-wise operand. We have

$$|\mathbf{X_m}|^2 = \left[|X_{m1}|^2, |X_{m2}|^2, \cdots, |X_{mN}|^2\right]. \tag{3.3}$$

After PSD estimation, the edges are detected. The edges of the PSD occur at the local extrema points of the first derivative of the PSD in a noise-free scenario.

3.2.1 Continuous Wavelet Transform-Based Edge Detection

The CWT of the PSD is used for edge detection purposes [21] due to its ability to find the irregularities and singularities of the signal [61].

In [21], it is shown that the edges exhibit local extrema in the first derivative of various scales of CWT of PSD. Thus, the first derivative of the product of various scales of CWT of PSD exhibits local extrema at the edge locations as well.

3.2.2 Spectrum Sensing by Differentiating the PSD

Alternatively, the edges can be obtained by differentiating the PSD with respect to frequency. We have

$$z(k) = S(k+1) - S(k), \tag{3.4}$$

where k is the frequency bin, $S(k)$ is the estimated PSD, and $z(k)$ represents the first derivative of the PSD. At the edge points, $z(k)$ exhibits a local extremum as the PSD level changes significantly at those points.

3.3 Modification to Current Edge Detection Techniques

There are at least two important characteristics concerning the estimated PSD in CR as follows:

1- The variance of the PSD estimation error is proportional to the signal strength [25]. This variance causes some large ripples in the stronger subbands of the estimated PSD.

2- The signal strength varies significantly in different subbands.

The fluctuations due to estimation error in stronger subbands may be larger than the edges of the weaker subbands. By applying edge detection techniques mentioned in previous section, the strong ripples of the stronger subbands may be considered to be the edges and/or the edges of the weaker subbands may be considered to be noise.

Let the time-domain signal in one subband, x_1, be m times stronger than the one in another subband, x_2. We have

$$\mathbf{x_1} = m \cdot \mathbf{x_2}. \tag{3.5}$$

Their DFT vectors have the following relation

$$\mathbf{X_1} = m \cdot \mathbf{X_2}. \tag{3.6}$$

Their estimated PSD obeys:

$$\mathbf{S_1} = m^2 \cdot \mathbf{S_2}. \tag{3.7}$$

Therefore based on the fact that estimation error variance is proportional to the signal strength, their estimation error variances have the following relation:

$$\sigma^2_{S_1} = m^2 \cdot \sigma^2_{S_2}. \tag{3.8}$$

Now, consider that $\mathbf{S_{dB}} = 10\log_{10}(\mathbf{S})$ represents the associated dB-scale values of the estimated PSD. The estimation error variances of two PSDs have the following relation

$$10\log_{10}(\mathbf{S_1}) = 10\log_{10}(m^2\mathbf{S_2}) = 20\log_{10}(m) + 10\log_{10}(\mathbf{S_2}). \tag{3.9}$$

Since, $20\log_{10}(m)$ is added as a constant in the above equation, it will not contribute to increase the estimation error variance. Therefore in dB-scale, the estimation error variances of two signals are equal. We have

$$\sigma^2_{S_{dB_1}} = \sigma^2_{S_{dB_2}}. \tag{3.10}$$

Thus, by applying the dB-scale values of the estimated PSD, we face almost the same estimation error variances in various subbands regardless of their levels of energy at the expense of additional computational complexity due to linear to dB-scale conversion.

To understand the effect of various levels of energy on the estimation error variances in both linear scale and dB-scale, the following simulation result is presented in Figure 3.1 (SNR= 10, 6, and 0 dB for three occupied subbands). SNR is calculated individually over various subbands and is defined as the ratio of the signal power in each subband to the noise power in that subband. In the simulations, the PSD is estimated by Welch's method using 100 segments of 1024 points each. The estimated PSD in linear scale is shown at the top and the one in dB-scale is shown at the bottom. As can be seen in Figure 3.1, the stronger subbands in the linear scale subplot have larger fluctuations than the weaker subbands. Whereas in dB-scale subplot, the fluctuations have almost the same variance in various subbands regardless of their individual signal strengths.

3.4 The New Edge Detection Technique Based on Window-Normalization

Fluctuations in the edge vector due to both estimation error variance and noise may increase the probability of edge misdetection. Normalization techniques decrease the

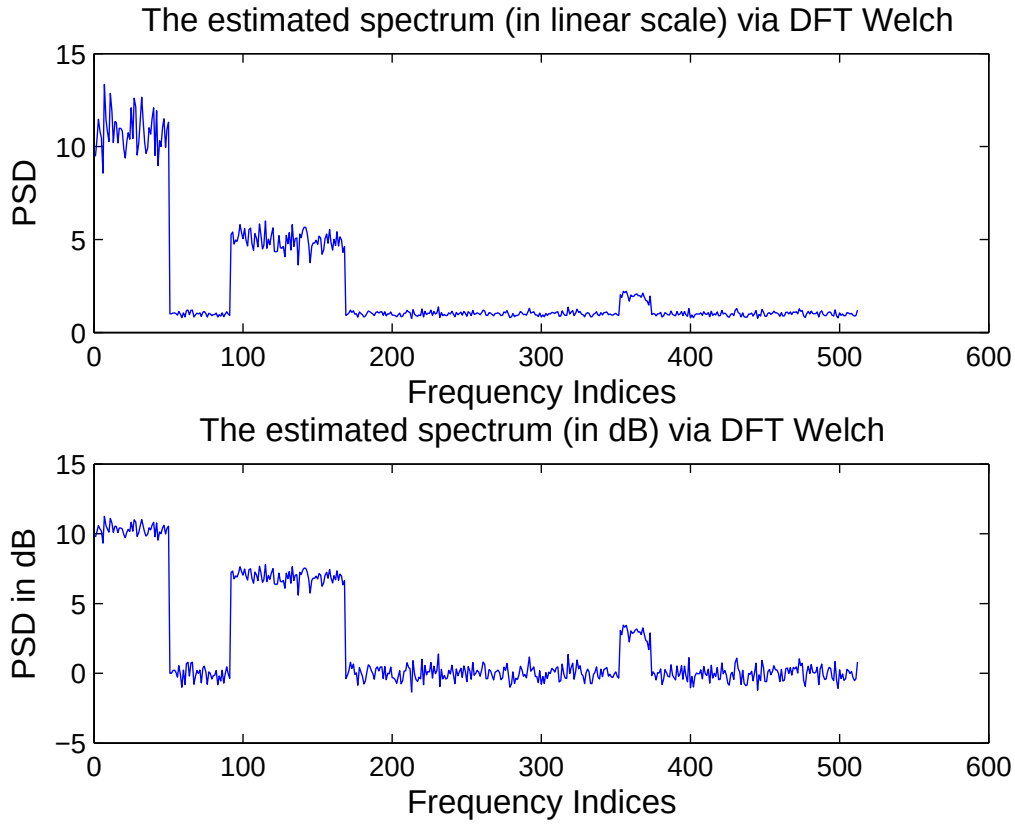

Figure 3.1: Estimated PSD in linear scale (top) and dB scale (bottom). SNR=10, 6 and 0 dB for three occupied subbands. 100 segments of 1024 points each are used for estimation using Welch's method.

fluctuations of a data vector. For example, the coefficient of variation has been used as a measure of dispersion. The coefficient of variation of a vector is given by

$$c = \left| \frac{\sigma}{\mu} \right| \tag{3.11}$$

where μ is the arithmetic mean of the data vector and σ is its standard deviation.

In this chapter, it is proposed to calculate the coefficients of variation over consecutive non-overlapping windows of an appropriate size. The normalized data vector is

obtained by dividing the windowed data $\mathbf{z_p}$ over the associated window's coefficient of variation; i.e., we have

$$\mathbf{z_{np}} = \frac{\mathbf{z_p}}{c_p} \tag{3.12}$$

where $\mathbf{z_p}$ is the edge vector over the p^{th} window, c_p is the window's coefficient of variation, and $\mathbf{z_{np}}$ is the normalized edge vector in that window. We have

$$\mathbf{c_p(n)} = \left| \frac{\sqrt{\frac{1}{K}\sum_{j=n-K}^{n-1} \mathbf{z_p^2(n)} - \frac{1}{K^2}\left(\sum_{j=n-K}^{n-1} \mathbf{z_p(n)}\right)^2}}{\frac{1}{K}\sum_{j=n-K}^{n-1} \mathbf{z_p(n)}} \right|, \quad n = mK+1; \quad m = 1, 2, ..., \tag{3.13}$$

in which K is the window size.

In Figure 3.2, the simulation result of the effect of window-normalization is shown. The first derivative of an estimated PSD (shown at top subplot) is shown in the middle. The normalized edge vector derived over a window of size 5 frequency bins is shown at the bottom. It can be seen that fluctuations are smoother in the normalized edge vector.

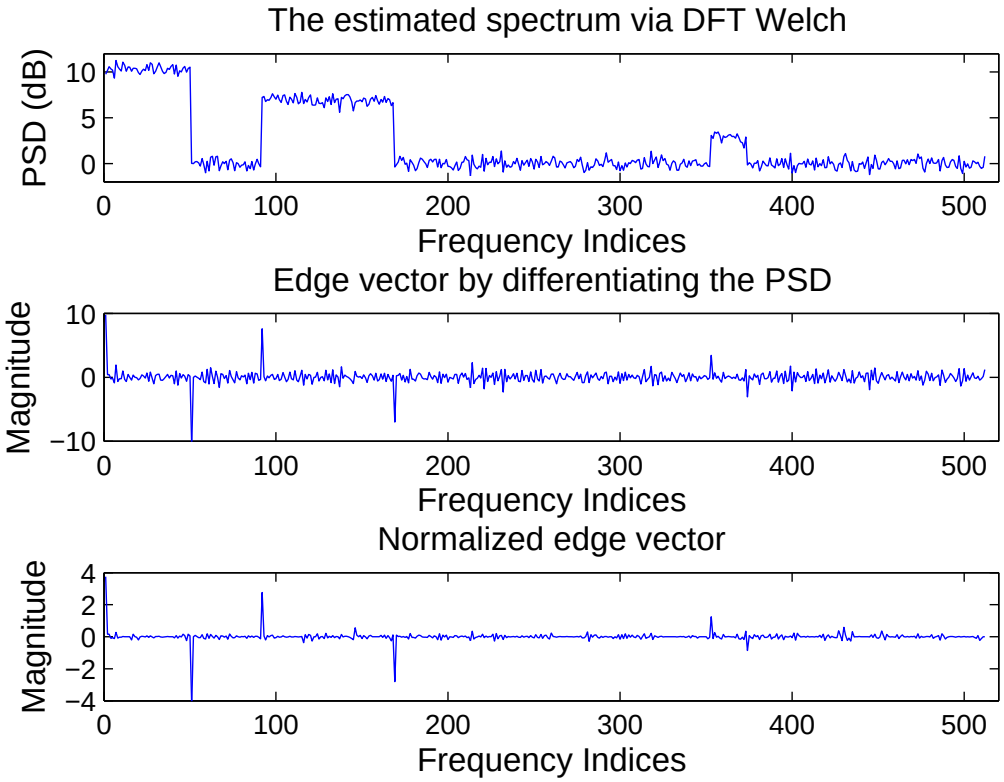

Figure 3.2: The estimated PSD in dB scale (top) and its first derivative shown in the middle along with the window-normalized edge vector (bottom). SNR=10, 6 and 0 dB for three occupied subbands. 100 segments of 1024 points each are used for estimation using Welch's method.

3.5 The New Edge Detection Technique Based on Window Averaging of PSD

In the proposed edge detection technique, the estimated PSD (in dB scale) is averaged over consecutive non-overlapping windows of an appropriate size. We have

$$\alpha(n) = \frac{1}{K} \sum_{j=n-K}^{n-1} S(j), \quad n = mK + 1; \quad m = 1, 2, ..., \tag{3.14}$$

where $\alpha(n)$ is the window-averaged PSD at the n^{th} point of the estimated PSD, $S(j)$ is the estimated PSD, and K is the window length over which the estimated PSD is averaged. The size of the window should not be very small, as a small window does not average the PSD well, while a large window may include two or more edges.

The window-averaged PSD can be seen in Figure 3.3 where the signal spectrum shaper filter is shown at the top, the estimated PSD is shown in the middle, and the window-averaged PSD is shown at the bottom. The PSD is estimated by Welch's method using 100 segments of 1024 points each. It can be seen in Figure 3.3 that the window-averaged PSD shows smoother variations compared to the estimated PSD because by averaging the PSD information, noise and estimation error pass through a low-pass filter.

It can be seen from Figure 3.3 that there is small variations in the window-averaged PSD. The amount of variations is proportional to the variance of estimation. In a practical system, the estimation error variance should be as low as possible. There are several ways to decrease estimation error variance. For instance, by increasing the number of segments in Welch's method, better PSD averaging is obtained which results in lower estimation error variance. In order to ignore the small variations due to estimation error variance, the integer part of the window-averaged PSD is considered. We have

$$\widehat{\alpha}(n) = \text{Round}(\alpha(n)) \tag{3.15}$$

where Round(.) gives the closest integer of a real number. In Figure 3.4, the signal

shaper filter is shown at the top along with the window-averaged PSD integer graph shown at the bottom. It can be seen from that figure that the approximate location of edges can be found by the integer part of the window-averaged PSD information.

The following points should be considered in the decision making algorithm.

1. In CR, it is assumed that there are enough spectrum vacancies. Moreover, the noise exhibits almost the same level of window-averaged PSD integer in vacant subbands. Therefore, we can assume that the most frequent window-averaged PSD integer (the mode) is the one representing the vacant subband. We have

$$\widetilde{\alpha} = \text{Mode}(\widehat{\alpha}(n)), \tag{3.16}$$

   where $\widetilde{\alpha}$ is the most frequent window-averaged PSD integer that represents the vacant subband level. Mode($\mathbf{V}$) gives the most frequent member of vector $\mathbf{V}$.

2. The window-averaged PSD integer level changes whenever an edge appears.

The decision making algorithm to find the approximate location of the edges is as follows:

1. If the window-averaged PSD integer increases from the noise level in consecutive windows, an ending point of a vacant subband is possibly in one of those windows where the increase happened.

2. If the window-averaged PSD integer decreases to the noise level in consecutive

windows, a starting point of a vacant subband is possibly in one of those windows where the decrease happened.

Equivalently, we have

if $\widehat{\alpha}(n) > \widehat{\alpha}(n-K)$ and $\widehat{\alpha}(n-K) \leq \widetilde{\alpha}$ **then**

an ending edge of a vacant subband is within the two windows. K is the window length.

else

if $\widehat{\alpha}(n) < \widehat{\alpha}(n-K)$ and $\widehat{\alpha}(n) \leq \widetilde{\alpha}$ **then**

a starting edge of a vacant subband is within the two windows.

end if

end if.

Now that the approximate location of an edge within a window is estimated, the exact edge location can be detected by locating the extremum of the first derivative of the PSD within the specified windows.

The proposed algorithm can be summarized as follows

1. The estimated PSD (in dB scale) is averaged over consecutive non-overlapping windows.

2. The integer part of the window-averaged PSD is calculated.

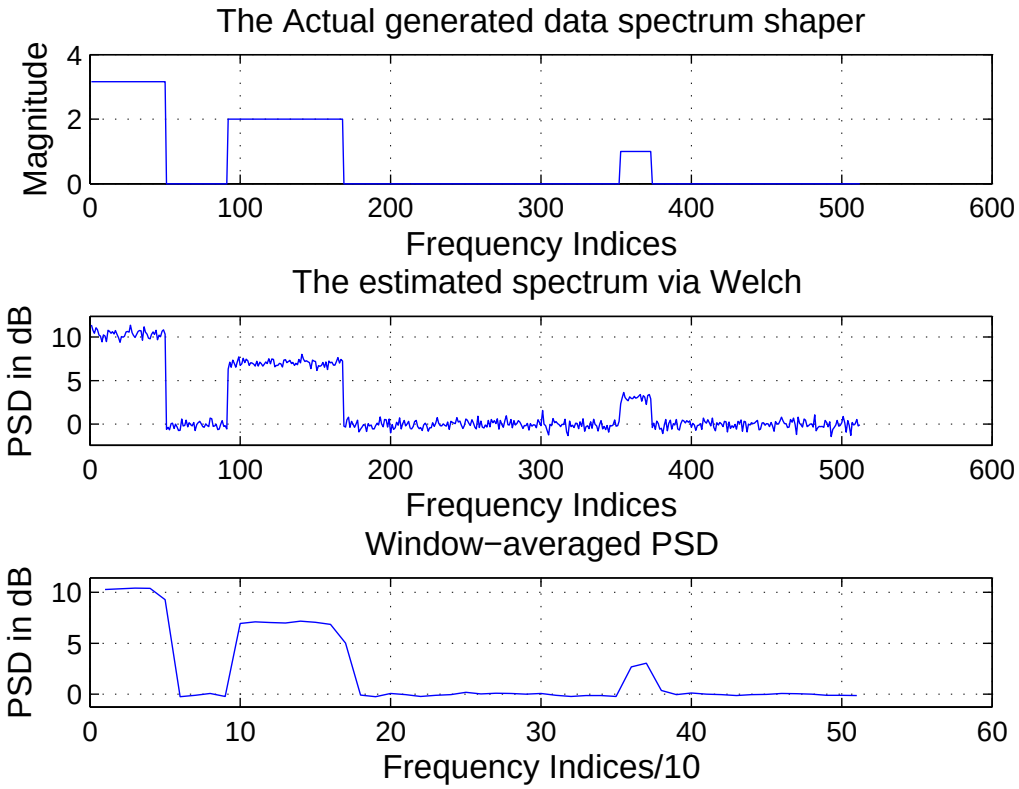

Figure 3.3: The window-averaged PSD. The PSD is estimated by Welch's method using 100 segments of 1024 points each. SNR=10, 6 and 0 dB for three subbands.

3. With the decision making algorithm, a window that most probabely has an edge, is specified.

4. The exact edge location can be detected by locating the extremum of the first derivative of the PSD within that specified window.

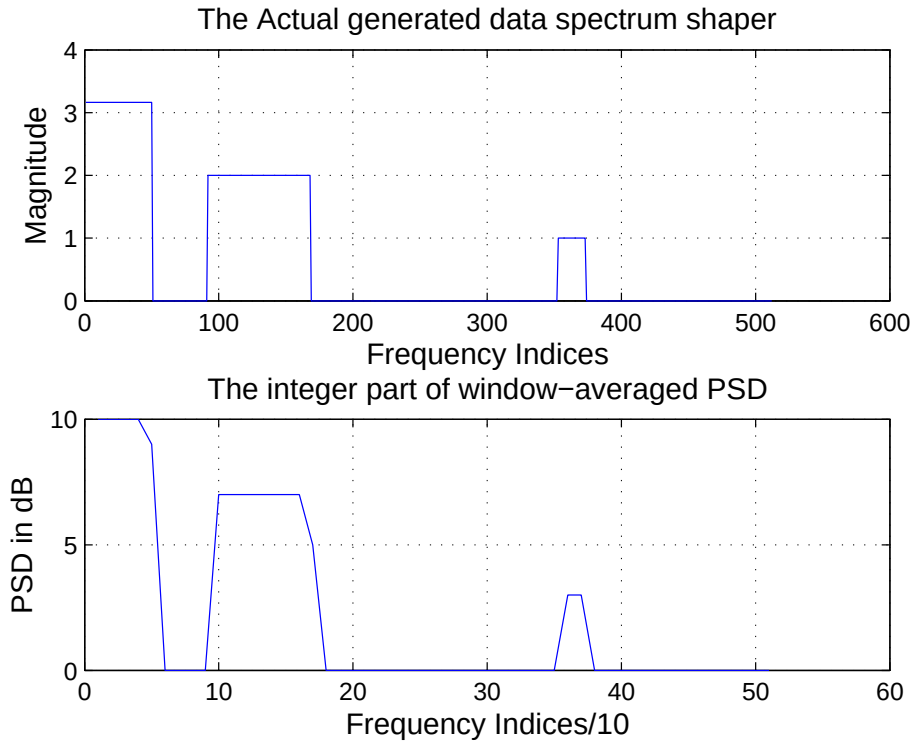

Figure 3.4: The window-averaged PSD integer with window size of $K = 10$ frequency bins. The PSD is estimated by Welch's method using 100 segments of 1024 points each. SNR=10, 6 and 0 dB for three subbands.

3.6 Simulation Results

3.6.1 Simulation Methodology

Simulations were run in MATLAB. To generate the received data with a specified spectrum, a white Gaussian noise process $w(n)$ is converted to the frequency domain to obtain $W(k)$. The frequency domain white Gaussian process is multiplied by a given spectrum shaping filter $F(k)$. This constructs the frequency domain samples of the cognitive radio received signal with a given spectrum shaping filter. The

result is then converted to the time domain by taking inverse DFT (IDFT). This procedure is shown in Figure 3.5. Then noise is added to the constructed signal to introduce a specific signal to noise ratio. The PSD can be estimated using Welch's method for both DFT and SDFT techniques. The edges can be obtained based on the proposed edge detection technique. The detection rate of the proposed techniques can be obtained by comparing the estimated edge locations to the actual ones. The simulations are run several times to get an accurate detection rate using Monte-Carlo simulation technique.

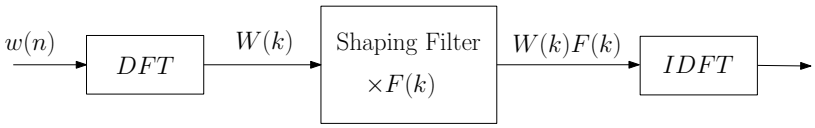

Figure 3.5: Creating a signal with a given spectrum shaping filter for the simulations.

3.6.2 Detection Rate Simulation Results

In this section, some simulation results are provided showing the superiority of the proposed methods in detecting the edges especially in the case where the signal levels have very different energy levels in various subbands. The signal with PSD shown in Figure 3.3 is used for these simulations.

Figure 3.6 shows the detection rate of two current edge detection methods (mentioned in Section 3.2) along with the modified edge detection method. In the modified one, the derivative of the dB-scale values of PSD has been employed instead of the linear scale values. The PSD is estimated by Welch's method using 100 segments of

1024 points each. The SNR is the SNR of the strongest subband. The other two subbands are 4 and 10 dB weaker. SNR is calculated individually over various subbands and is defined as the ratio of the signal power in each subband to the noise power in that subband. For the CWT-based edge detection used in these simulations, the product of first 8 scales of Haar-CWT is used.

It can be seen from Figure 3.6 that by employing the linear scale values of PSD, the edges cannot be detected accurately because the large fluctuations within the stronger subbands are wrongly detected as edges while the weaker subbands edges are treated as noise. Simulation results show the ability of the modified method to detect the edges of the vacant subbands especially in the case where the subbands have shown very different levels. That is due to the fact that by employing the dB-scale values of PSD, various subbands show almost the same variances regardless of their levels of energy.

Figure 3.7 shows the detection rate of the new edge detection methods along with the one for the modified wavelet-differentiation-based and differentiation-based methods. The dB-scale modification introduced earlier has been applied to all methods. The simulation results are derived from 100 non-overlapping segments of 1024 samples each using Welch's method. The length of the window is considered to be 10 frequency bins for averaging-based technique and 5 for the normalization-based edge detection method. The SNR is the SNR of the strongest subband. The other two subbands are 4 and 10 dB weaker. For the CWT-based edge detection used in this simulation, the

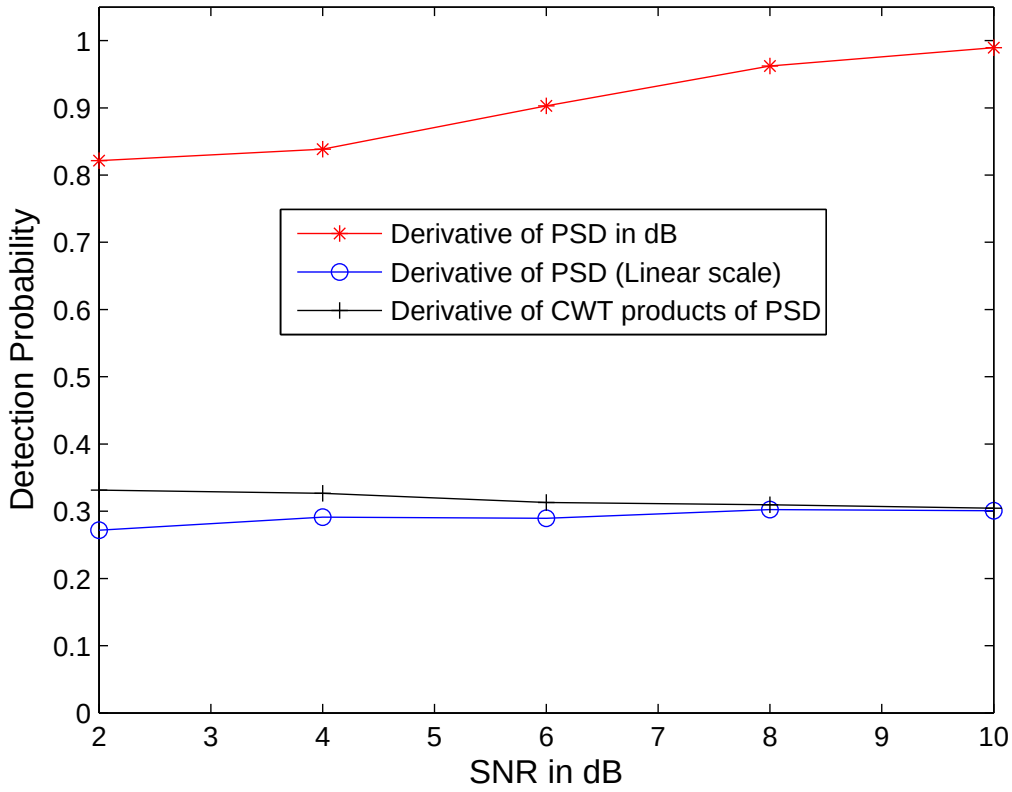

Figure 3.6: The detection rate for two edge detection methods using linear scale PSD values and the modified edge detection method using dB-scale PSD values. The SNR is the SNR of the strongest subband.

product of the first 8 scales of Haar-CWT is used. To compare the computational complexity of the edge detection methods of this simulation, their CPU processing times on a personal computer using MATLAB are derived. The wavelet-based one was run in 0.25 seconds, the new averaging-based technique needed 0.062 sec., the new normalization-based method required 0.046 sec., and the simple differentiation was run in 0.031 sec.

It can be seen in Figure 3.7 that the new averaging-based edge detection method

exhibits better detection rate compared to the other edge detection methods even after applying the proposed modification. Moreover, the normalization-based technique increases the detection rate of the derivative-based method. However its detection capability is not as good as the averaging-based edge detection method nor the CWT-based one, it is less computationally complex than those methods.

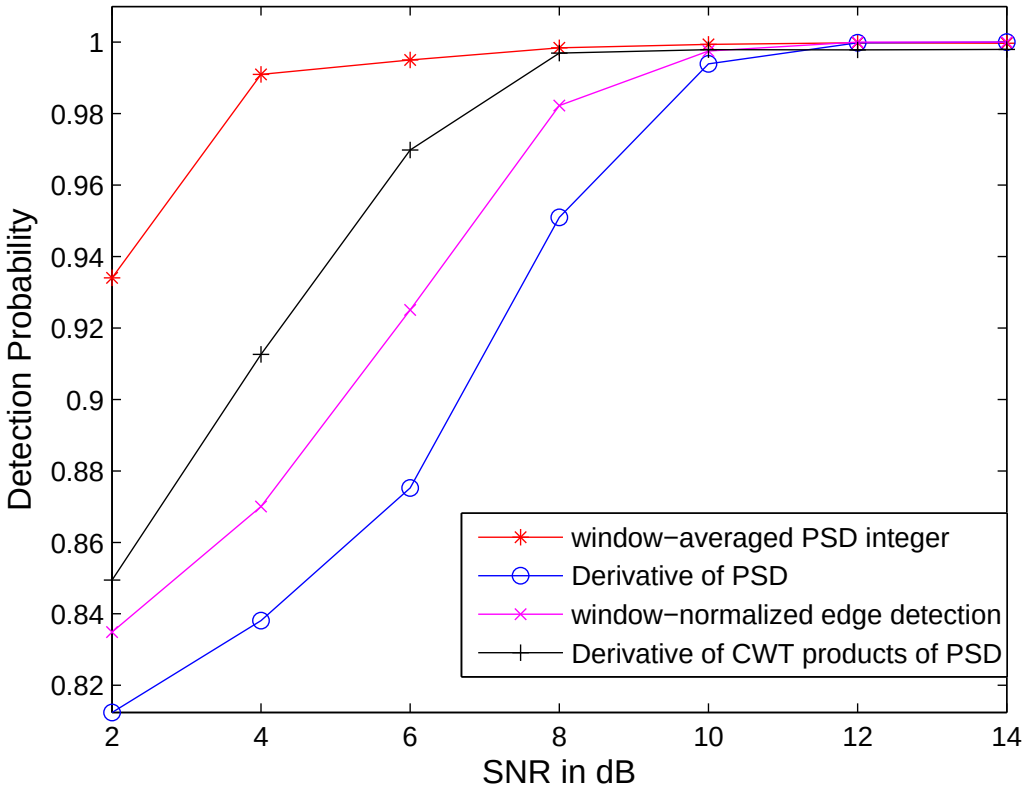

Figure 3.7: The detection rate for different edge detection methods. The proposed new methods are compared to the modified current methods. The SNR is the SNR of the strongest subband.

3.7 Conclusion

In this chapter, we have shown the drawbacks of current methods in spectrum sensing when levels of signal are (very) different in various subbands. Stronger subbands have higher estimation error variances resulting in large fluctuations within the estimated PSD. In current edge detection methods, these large ripples may be detected as edges. Especially when the levels of signal are significantly different, current methods of spectrum sensing are not capable of detecting the presence of a signal even in high SNR scenario. It is proposed to employ the dB-scale values of PSD instead of the linear scale values so that the estimation error variance does not change significantly by the level of energy in different subbands. The simulation results show improved performance by applying this modification. Also, we propose a new edge detection technique based on window-normalization that exhibits better detection rate compared to the conventional methods even after applying the dB-scale modification. Finally, another new edge detection method is proposed that smooths the fluctuations and detects the noise level of the estimated PSD. This method utilizes the integer part of window-averaged PSD as its metric to detect presence of an edge. The proposed method shows the best detection rate.

Chapter 4

Simplified DFT PSD Estimation Techniques

4.1 Introduction

The first step in spectrum sensing is PSD estimation. Discrete Fourier transform (DFT)-based PSD estimation methods are the most widely used [28]. Though widely used, DFT-based PSD estimation is complex because the received signal samples are multiplied by a number of complex DFT coefficients to find an accurate PSD shape. To reduce computational complexity of spectrum sensing for CR, different PSD techniques are investigated. For example, the wavelet packet transform (WPT) has also been proposed for PSD estimation [62, 63]. WPT-based PSD estimation methods are less computationally complex since a reduced number of multiplications are required

for the time-to-frequency domain conversion process. For instance, Haar-WPT-based PSD estimation requires no multiplications in the time-to-frequency conversion step.

The second step in spectrum sensing is to detect the PSD edges. To simplify the analysis, as is done in [21], it is assumed that the received signal PSD in CR has a piecewise rectangular-like shape. In [21], the edges are detected as the local extrema of the first derivative of the product of various scales of continuous wavelet transform (CWT) of the PSD with respect to frequency. Alternatively, the edges can be detected by locating the local extrema of the first derivative of the PSD with respect to the frequency.

In this chapter, 4 simplified DFT-based spectrum sensing methods are presented. We investigate the accuracy of these methods by comparing their edge detection capabilities compared to more computationally complex spectrum sensing methods. This is done using Monte Carlo simulation methods as well as analytically. The proposed methods are less computationally complex than DFT-based methods while maintaining a comparable edge detection performance. When compared to the Haar-WPT-based PSD estimation methods, our proposed SDFT-based methods show an improved edge detection performance while being similar in computational complexity. Moreover, a Sinc squared shape PSD is used for simulations and a new edge detection technique is proposed. It is shown both by simulations and mathematical analysis that the performance of the proposed method is comparable to that of the DFT-based method especially under low spectrum occupancy conditions; a reason-

able assumption in CR networks. Preliminary performance results were published in [40, 41].

4.2 System Model of Simplified DFT-based PSD Estimation Techniques

In CR, the PSD is assumed to have the shape in which each subband has a rectangular-like shape and its level abruptly changes at the starting/ending points of the subband as is done in [21]. Meanwhile, the narrowest subband is assumed to have enough frequency bins so that each subband has two edges as its starting and ending points.

Our goal in spectrum sensing is to detect the edges of the PSD after approximating the PSD. Different methods of edge detection has been introduced in [39]. Assuming the rectangular-like shape of PSD, the PSD edges can be detected by differentiating the PSD with respect to frequency. The edges are located at the local extrema of the first derivative of PSD. Alternatively, the edges can be found by locating the local extrema of the first derivative of the product of various scales of CWT of the PSD as discussed in [21].

4.2.1 Welch's method for PSD estimation

In Welch's algorithm, the received signal samples are split into segments and the periodogram of each segment is calculated. The average segment periodogram is

then obtained. Let $\mathbf{x_m}$ be the received signal samples vector of the m^{th} segment given by

$$\mathbf{x_m} = \begin{bmatrix} x_m(0) & x_m(1) & \cdots & x_m(N-1) \end{bmatrix}^H \tag{4.1}$$

where H denotes the vector Hermitian transpose and N is the number of points in the segment.

$\mathbf{X_m}$ is the DFT vector of that segment and can be obtained by

$$\mathbf{X_m} = D \cdot \mathbf{x_m} \tag{4.2}$$

where D is the DFT matrix. An N by N DFT matrix is given by

$$D = \begin{pmatrix} 1 & 1 & 1 & \cdots & 1 \\ 1 & d & d^2 & \cdots & d^{N-1} \\ 1 & d^2 & d^4 & \cdots & d^{2(N-1)} \\ \vdots & \vdots & \vdots & \ddots & \vdots \\ 1 & d^{N-1} & d^{2(N-1)} & \cdots & d^{(N-1)(N-1)} \end{pmatrix} \tag{4.3}$$

where

$$d = \exp(-j2\pi/N). \tag{4.4}$$

Then, the periodogram of each segment can be calculated as

$$\mathbf{S_m} = \frac{|\mathbf{X_m}|^2}{N} \tag{4.5}$$

where $\mathbf{S_m}$ is the m^{th} segment's periodogram vector and $|\cdot|^2$ is operated on each element of the vector. We have

$$|\mathbf{X_m}|^2 = \left[|X_{m1}|^2, |X_{m2}|^2, \cdots, |X_{mN}|^2\right]. \tag{4.6}$$

The PSD estimation is then achieved by linearly averaging the periodograms of all segments as,

$$\mathbf{S} = \frac{1}{M}\sum_{m} \mathbf{S_m} \tag{4.7}$$

where M is the number of segments contributing in Welch's method.

After PSD estimation, the edges are detected. Different methods of edge detection for wideband spectrum sensing are developed in [39]. The simplest edge detection method implies that edges of the PSD occur at the local extrema points of the first derivative of the PSD in noise free scenario. The edges (k') satisfy,

$$\Delta\mathbf{S}(k)\Big|_{k=k'} = \text{Local Extrema}\left(\mathbf{S}(k+1) - \mathbf{S}(k)\right) \tag{4.8}$$

where k indicates the frequency bin.

A modified version of window-averaging based edge detection technique proposed

in [39] (and discussed in Chapter 3) has also been applied for some simulations in this chapter. The proposed algorithm can be summarized as follows

1. The estimated PSD (in dB scale) is averaged over consecutive non-overlapping windows.

2. The integer part of the window-averaged PSD is calculated.

3. Based on the low spectrum occupancy assumption in CR, the most frequent integer of window-averaged PSD (the mode) is assumed to be the most probable noise level. The edges are located in the cross section of the noise level and the PSD curve.

4. The area under the PSD curve (the integral of the PSD) between two consecutive edges (detected in the previous step) gives the energy level of that subband.

5. A subband with energy level above the noise level determined in the previous step is assumed to be an occupied subband. Therefore their edges are rough estimates of the edges of the PSD.

6. The exact edge location can be detected by locating the extremum of the first derivative of the PSD within that specified window.

Steps 4 and 5 in the above algorithm are modifications to the window-averaging based edge detection algorithm presented in [39].

4.2.2 Simplified DFT-based PSD estimation

By modifying the DFT matrix, we derive some less complex methods for PSD estimation. Four simplified methods presented are named as sign, sign-sign, round, and round-round. The following points are used for simplification.

- In two of the SDFT methods, only the real part of the DFT matrix is used. This simplification is inspired from the discrete cosine transform (DCT) in which the real part of the DFT matrix is used.

- The sign or round of the DFT matrix elements are used to approximate the DFT elements. The sign-SDFT leads to a conversion matrix with +1 and -1 while the round-SDFT results in a conversion matrix with +1, -1 and 0 elements.

For sign-SDFT method, we have

$$D_s = \text{sgn}(\text{Re}(D)) \tag{4.9}$$

where sgn(.) denotes the sign function, Re(.) takes the real part of a complex value, D is the DFT matrix, and D_s is the sign-SDFT matrix. The sign function is defined as

$$\text{sgn}(f(u)) = \begin{cases} +1 & f(u) > 0 \\ \text{sign}(f(u+\varepsilon)) & f(u) = 0 \\ -1 & f(u) < 0 \end{cases} \tag{4.10}$$

in which ε is a very small positive increment and $\text{sign}(f(u))$ is defined as

$$\text{sign}(f(u)) = \begin{cases} +1 & f(u) > 0 \\ 0 & f(u) = 0 \\ -1 & f(u) < 0 \end{cases} \tag{4.11}$$

where $f(u)$ is either $\sin(u)$ when $\text{Im}(D)$ is taken into account or $\cos(u)$ when $\text{Re}(D)$ is considered.

For sign-sign-SDFT method, we have

$$D_{ss} = \text{sgn}(\text{Re}(D)) + j\text{sgn}(\text{Im}(D)) \tag{4.12}$$

where Im(.) takes the imaginary part of a complex value. For round-SDFT method, we have

$$D_r = \text{Round}(\text{Re}(D)) \tag{4.13}$$

where Round(.) rounds a real number to its closest integer. For round-round-SDFT method, we have

$$D_{rr} = \text{Round}(\text{Re}(D)) + j\text{Round}(\text{Im}(D)). \tag{4.14}$$

In the above equations, D_s is the sign-SDFT matrix, D_{ss} is the sign-sign-SDFT matrix, D_r is the round-SDFT matrix and D_{rr} is the round-round-SDFT matrix.

4.2.3 Mathematical Analysis of sign-SDFT-based Spectrum Sensing Method

To demonstrate the performance of the proposed methods, the sign-SDFT and round-SDFT methods are analyzed. The same procedure can be applied to analyze the other simplified methods.

Based on (4.9) and (4.3), an 8 by 8 sign-SDFT matrix is given by,

$$D_s = \begin{pmatrix} +1 & +1 & +1 & +1 & +1 & +1 & +1 & +1 \\ +1 & +1 & +1 & -1 & -1 & -1 & -1 & +1 \\ +1 & +1 & -1 & -1 & +1 & +1 & -1 & -1 \\ +1 & -1 & -1 & +1 & -1 & +1 & +1 & -1 \\ +1 & -1 & +1 & -1 & +1 & -1 & +1 & -1 \\ +1 & -1 & +1 & +1 & -1 & +1 & -1 & -1 \\ +1 & -1 & -1 & +1 & +1 & -1 & -1 & +1 \\ +1 & +1 & -1 & -1 & -1 & -1 & +1 & +1 \end{pmatrix}. \tag{4.15}$$

As can be seen from the above example, the sign-SDFT requires only additions and subtractions to be performed, thus making the whole procedure of spectrum sensing less complex.

From (4.5), (4.7) and (4.9), the PSD obtained by sign-SDFT-based Welch's method

in each frequency bin k is calculated as,

$$S(k) = \frac{1}{NM} \sum_{m=1}^{M} \left| \sum_{n=0}^{N-1} \text{sgn}\left(\cos(2\pi kn/N)\right) \cdot x_m(n) \right|^2 . \tag{4.16}$$

(4.16) can be expanded as

$$\begin{aligned}
&S(k) = \frac{1}{NM} \sum_{m=1}^{M} (\\
&x_m^2(0) + x_m^2(1) + \ldots + x_m^2(N-1) + \\
&2\text{sgn}\left(\cos\left(\frac{2\pi k}{N}\right)\right) x_m(0)x_m(1) + 2\text{sgn}\left(\cos\left(\frac{2\pi(2k)}{N}\right)\right) x_m(0)x_m(2) + \ldots + \\
&2\text{sgn}\left(\cos\left(\frac{2\pi k}{N}\right)\right) \text{sgn}\left(\cos\left(\frac{2\pi(2k)}{N}\right)\right) x_m(1)x_m(2) + \\
&2\text{sgn}\left(\cos\left(\frac{2\pi k}{N}\right)\right) \text{sgn}\left(\cos\left(\frac{2\pi(3k)}{N}\right)\right) x_m(1)x_m(3) + \ldots + \\
&2\text{sgn}\left(\cos\left(\frac{2\pi(2k)}{N}\right)\right) \text{sgn}\left(\cos\left(\frac{2\pi(3k)}{N}\right)\right) x_m(2)x_m(3) + \\
&\ldots) \cdot
\end{aligned} \tag{4.17}$$

The autocorrelation function of the received signal at lag L ($R(L)$) can be obtained by

$$\begin{aligned}
&R(L) \simeq \frac{1}{M} \sum_{m=1}^{M} x_m(n)x_m(n+L), \qquad \forall n, \\
&L = 0, \cdots, N-1.
\end{aligned} \tag{4.18}$$

For the sign-SDFT, by substituting (4.18) into (4.17) and performing some alge-

bra, we have

$$S(k) = \frac{2}{N} \sum_{L=0}^{N-1} R(L) \times \sum_{l=0}^{N-L-1} \operatorname{sgn}\left(\cos\left(\frac{2\pi kl}{N}\right)\right) \operatorname{sgn}\left(\cos\left(\frac{2\pi k(l+L)}{N}\right)\right). \tag{4.19}$$

Similarly, for the round-SDFT, (4.16) can be written as:

$$S(k) = \frac{2}{N} \sum_{L=0}^{N-1} R(L) \sum_{l=0}^{N-L-1} \operatorname{Round}\left(\cos\left(\frac{2\pi kl}{N}\right)\right) \operatorname{Round}\left(\cos\left(\frac{2\pi k(l+L)}{N}\right)\right). \tag{4.20}$$

We consider a rectangular shape PSD with an autocorrelation function given as

$$R(L) = \frac{\sin(2\pi k' L/N)}{\pi L} + \delta(L) \cdot \sigma_n^2, \tag{4.21}$$

where k' is the edge location of the rectangular shape PSD, σ_n^2 is the noise power and $\delta(\cdot)$ is the Kronecker delta function.

The analysis of (4.19), (4.20), and (4.21) is difficult. However, they can be computed numerically. As an example, the PSDs of a received signal spectrum with cut-off frequency bin of $k' = 200$ and $N = 1024$ have been derived and plotted in Figure 4.1 and Figure 4.2 for different SNRs using both round and sign-SDFT methods. These figures show that SDFT methods are capable of detecting edges without estimating the exact shape of the PSD. Since PSD of white Gaussian noise is a constant, it can be seen that noise shifts all the values of PSD equally.

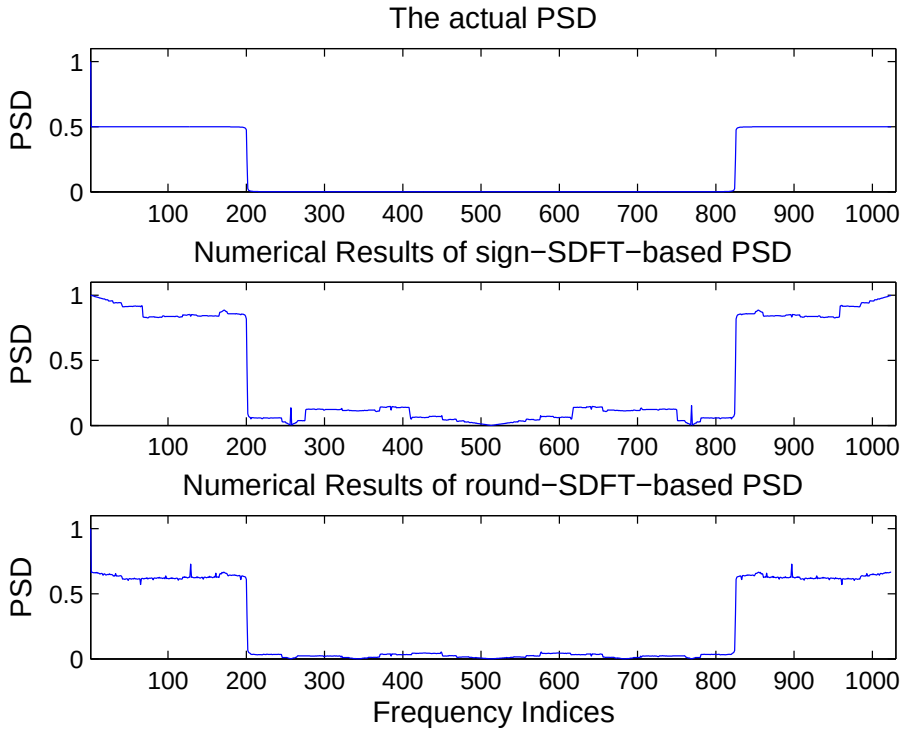

Figure 4.1: Numerical results of Equation 4.19 (top) and Equation 4.20 (bottom) by applying the actual spectrum with cut-off frequency bin of $k' = 200$ and $N = 1024$. $SNR = \infty$.

4.2.4 Statistical Analysis of SDFT

The SDFT methods can be interpreted as the coefficient quantization techniques in which the nonlinear relationships of both Round and Sign functions are shown in Figure 4.3. The statistical model of DFT coefficient quantization error [25] is shown in Figure 4.4. The output of the model is given as follows:

$$X'(k) = \sum_{n=0}^{n=N-1} (x(n)d^{nk} + e(n,k)). \tag{4.22}$$

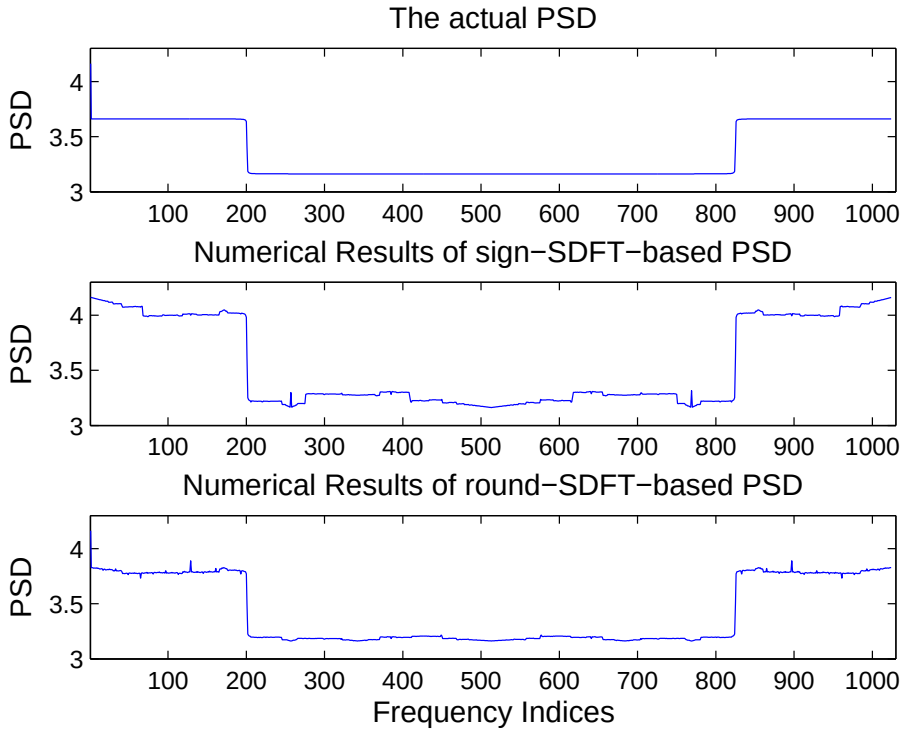

Figure 4.2: Numerical results of Equation 4.19 (top) and Equation 4.20 (bottom) by applying the actual spectrum with cut-off frequency bin of $k' = 200$ and $N = 1024$. $SNR = -10dB$.

where $e(n,k)$ is the error due to quantizing the DFT coefficients to the nearest integers of $\{-1, 0, +1\}$ in rounding process or taking the sign of the DFT coefficients from the set $\{-1, +1\}$ in sign methods. We have

$$e(n,k) = x(n)(d^{nk} - Q(d^{nk})). \tag{4.23}$$

where $Q(.)$ is the quantization function. For complex values, we define

$$Q(x + jy) = Q(x) + jQ(y). \tag{4.24}$$

Assuming that the DFT coefficient quantization errors are uncorrelated and independent of the input signal and of each other [25], then those errors are given as

$$g(k) = d^{nk} - Q(d^{nk}). \tag{4.25}$$

The total error is calculated as

$$E(k) = \sum_{n=0}^{N-1} e(n,k). \tag{4.26}$$

It can be shown that the variance of the total error is [25]

$$\sigma_E^2 = 4N\sigma_x^2\sigma_g^2, \tag{4.27}$$

where σ_x^2 is the input signal power and σ_g^2 is the DFT coefficient quantization error variance. The coefficient 4 in (4.27) is due to four components of the complex multiplications. Since the coefficient quantization error is assumed to follow the uniform distribution [25], σ_g^2 is constant and depends only on the quantization step size. Therefore, the total error is a function of the input signal power.

Moreover, based on Parseval's theorem, the input signal power is a function of spectrum occupancy in the frequency domain. We have

$$\sum_{n=0}^{N-1} |x(n)|^2 = \frac{1}{N} \sum_{k=0}^{N-1} |X(k)|^2. \tag{4.28}$$

As the occupancy of the spectrum increases, σ_x^2 increases which leads to an increase in σ_E^2. Therefore, the SDFT-based PSD estimates are more suitable for spectrum sensing when the spectrum occupancy is low such as CR.

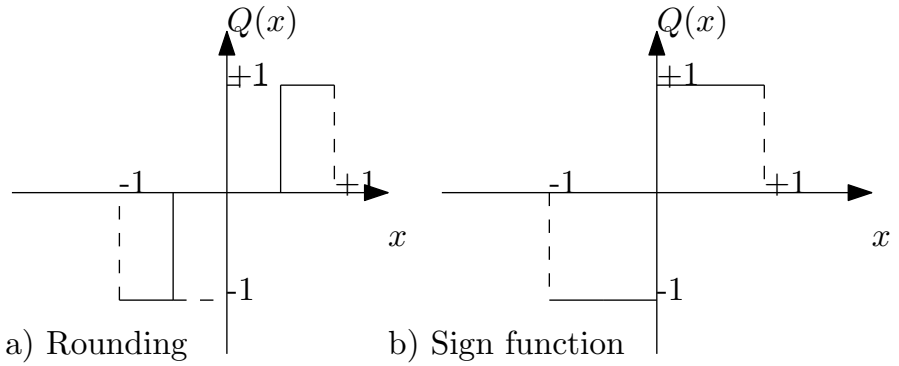

Figure 4.3: Quantization functions of SDFT methods.

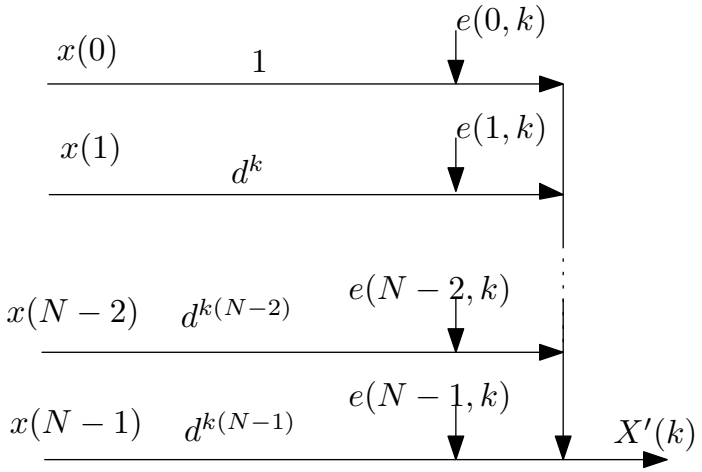

Figure 4.4: Statistical model for DFT coefficient quantization errors in DFT implementation.

4.2.5 Estimation Error Variance and Performance Analysis

Bias and variance are two important metrics of estimation. Welch's method is an estimation method that is asymptotically unbiased [25]. The other very important

metric for all estimation techniques is estimation error variance. The lower the variance, the better the estimation. In this subsection, the estimation error variance for both DFT-based and SDFT-based spectrum sensing methods are given.

The received signal sample DFT and SDFT coefficients $\mathbf{X}$ have two components of real and imaginary parts with Gaussian distribution in each segment. For DFT-based PSD estimation and at frequency bin k_0, we have:

$$X_r(k_0) = \frac{1}{\sqrt{N}} \sum_{n=0}^{N-1} x(n) \cos\left(\frac{2\pi k_0 n}{N}\right) \tag{4.29}$$

and

$$X_i(k_0) = \frac{1}{\sqrt{N}} \sum_{n=0}^{N-1} x(n) \sin\left(\frac{2\pi k_0 n}{N}\right). \tag{4.30}$$

where $\mathbf{X_r}$ and $\mathbf{X_i}$ are the real and imaginary components of the frequency coefficients of the received signal, respectively. For sign-sign SDFT-based PSD estimation, we have:

$$X_r(k_0) = \frac{1}{\sqrt{N}} \sum_{n=0}^{N-1} x(n)\text{sgn}\left(\cos\left(\frac{2\pi k_0 n}{N}\right)\right) \tag{4.31}$$

and

$$X_i(k_0) = \frac{1}{\sqrt{N}} \sum_{n=0}^{N-1} x(n)\text{sgn}\left(\sin\left(\frac{2\pi k_0 n}{N}\right)\right). \tag{4.32}$$

For round-round SDFT, the sign functions in the above equations are replaced by round functions.

4.2.5.1 Periodogram-based Estimation Error Variance

In periodigram-based estimation, there are two Gaussian components with zero mean and variance σ_a^2. We have

$$\mathbf{X_r} \sim N(0, \sigma_a^2), \quad \mathbf{X_i} \sim N(0, \sigma_a^2), \tag{4.33}$$

where $N(0, \sigma_a^2)$ represents Gaussian distribution with zero mean and variance σ_a^2. The variance of them are given as follows: For DFT-based components, from (4.29), we have

$$\sigma_{X_r}^2 = \frac{1}{N} \sum_{n=0}^{N-1} \sigma_n^2 \cos^2 \left(\frac{2\pi k_0 n}{N} \right) \tag{4.34}$$

Since $\sum_{n=0}^{N-1} \cos^2 \left(\frac{2\pi k_0 n}{N} \right) = N/2$, we have [59], [64]

$$\sigma_{a-DFT}^2 = \sigma_{X_r}^2 = \sigma_n^2/2, \tag{4.35}$$

where σ_{a-DFT}^2 is the estimation error variance of the PSD obtained by DFT-based periodogram PSD estimation technique. For sign-SDFT-based components, from (4.31), we have

$$\sigma_{X_r}^2 = \frac{1}{N} \sum_{n=0}^{N-1} \sigma_n^2 \mathrm{sgn}^2 \left(\cos \left(\frac{2\pi k_0 n}{N} \right) \right) \tag{4.36}$$

Since $\mathrm{sgn}^2(.) = 1$, we have

$$\sigma_{a-ss-SDFT}^2 = \sigma_n^2, \tag{4.37}$$

where $\sigma^2_{a-ss-SDFT}$ is the estimation error variance of the PSD obtained by sign-sign-SDFT-based periodogram PSD estimation technique and σ^2_n is the variance of noise. Since $\sum_{n=0}^{N-1} \text{Round}^2\left(\cos^2\left(\frac{2\pi k_0 n}{N}\right)\right) = \frac{4\pi/3}{2\pi}N = \frac{2}{3}N$, for round-SDFT-based components, we have

$$\sigma^2_{a-rr-SDFT} = \frac{2}{3}\sigma^2_n, \tag{4.38}$$

where $\sigma^2_{a-rr-SDFT}$ is the estimation error variance of the PSD obtained by round-round-SDFT-based periodogram PSD estimation technique.

In the case where no signal is present, the periodogram-based estimated PSD consists of two (real and imaginary) Gaussian distribution variables with zero mean, and thus follows a central chi-square distribution [65] given by

$$P_n(u) = \frac{1}{2\sigma^2_{S_0}} e^{-u/2\sigma^2_{S_0}} \quad , u \geq 0, \tag{4.39}$$

where $P_n(u)$ is the probability density function of the periodogram-based estimated PSD, subscript n represents noise only scenario, $\sigma^2_{S_0}$ is its variance in the absence of signal. The estimation error variance of the central chi-square distribution with $n = 2$ Gaussian contributors is given by [65]

$$\sigma^2_{S_0} = 2n\sigma^4_a = 4\sigma^4_a, \tag{4.40}$$

where σ^2_a are given in (4.35), (4.37) and (4.38) for different methods.

When the primary signal is present, these two components follow a Gaussian distribution with mean m_r and m_i and variance σ_a^2. We have

$$\mathbf{X_r} \sim N(m_r, \sigma_a^2) \quad \mathbf{X_i} \sim N(m_i, \sigma_a^2). \tag{4.41}$$

The periodogram-based estimated PSD follows a non-central chi-square distribution [65] given by

$$P_S(u) = \frac{1}{2\sigma_{S_1}^2} e^{-(c^2+u)/2\sigma_{S_1}^2} I_0\left(\sqrt{u}\frac{c}{\sigma_{S_1}^2}\right) \quad , u \geq 0, \tag{4.42}$$

where $P_S(u)$ is the probability density function of the periodogram-based estimated PSD, subscript S represents the presence of signal, $\sigma_{S_1}^2$ is its variance in the presence of signal. I_0 is the modified Bessel function of the first kind of order zero and c is the non-centrality parameter of the chi-square distribution given by

$$c = \sqrt{m_r^2 + m_i^2}. \tag{4.43}$$

The square of the non-centrality parameter of chi-square distribution shows the distance between the mean of the non-central chi-square distribution to the mean of the central one [65].

The estimation error variance of the non-central chi-square distribution with $n = 2$

Gaussian contributors is given by [65]

$$\sigma_{S_1}^2 = 2n\sigma_a^4 + 4\sigma_a^2 c^2 = 4\sigma_a^4 + 4\sigma_a^2 c^2, \tag{4.44}$$

where σ_a^2 is given in (4.35), (4.37) and (4.38) for different methods.

4.2.5.2 Periodogram-based single tone detection case

For simplicity, it is assumed that the primary signal consists of only a single tone at frequency bin k_0 and is given by

$$x(n) = \alpha \sin(2\pi k_0 n/N + \phi) + q(n), \tag{4.45}$$

where $q(n)$ is the noise sequence and the phase ϕ is uniformly distributed.

Assuming that the DFT coefficients are independent, the false alarm rate for periodogram-based PSD estimation in case of single tone detection is given by [64]

$$\begin{aligned} P_{fa} &= 1 - \left[\int_0^T P_n(u)\,\mathrm{d}u\right]^{N/2-1} \\ &= 1 - \left[1 - e^{-T/2\sigma_{S_0}^2}\right]^{N/2-1}, \end{aligned} \tag{4.46}$$

and the detection rate for periodogram-based PSD estimation in case of single tone

detection can be calculated as [64]

$$\begin{aligned} P_d &= 1 - \left[\int_0^T P_n(u)\,\mathrm{d}u\right]^{N/2-2} \int_0^T P_S(u)\,\mathrm{d}u \\ &= 1 - \left[1 - e^{-T/2\sigma^2_{S_0}}\right]^{N/2-2} \left(1 - Q_1\left(\frac{c}{\sigma_{S_1}}, \frac{\sqrt{T}}{\sigma_{S_1}}\right)\right), \end{aligned} \tag{4.47}$$

where T denotes the decision threshold and Q_1 represents the generalized Marcum Q function of the first order [59].

In order to calculate the estimation error variance for DFT-based and SDFT-based PSD estimation, it is required to obtain the non-centrality parameter. From (4.29), (4.30), (4.43), and (4.45) for a single tone detection case by doing some calculations, we have [64]

$$c = \sqrt{(\mathrm{E}(X_r))^2 + (\mathrm{E}(X_i))^2} = \frac{\alpha}{2}\sqrt{N}. \tag{4.48}$$

The non-centrality parameters of chi-square distribution for different SDFT-based PSD estimation methods for a single tone detection case are given as follows (the detailed calculations are presented in the following subsection):

$$c_{ss-SDFT} = \frac{2\alpha}{\pi}\sqrt{N}, \tag{4.49}$$

$$c_{s-SDFT} = \frac{\alpha}{\pi}\sqrt{N}, \tag{4.50}$$

$$c_{rr-SDFT} = \frac{2\alpha \sin(\pi/3)}{\pi}\sqrt{N}, \tag{4.51}$$

$$c_{r-SDFT} = \frac{\alpha \sin(\pi/3)}{\pi}\sqrt{N}, \tag{4.52}$$

in which $(\pi/3)$ is related to rounding at the threshold level of $\cos(\pi/3) = 0.5$. The variances of all SDFT-based methods can be obtained by substituting the non-centralities into (4.44).

4.2.5.2.1 Calculations of the periodogram-based single tone SDFT non-centrality parameters

To obtain the non-centrality parameter for sign-sign SDFT, from (4.45), (4.48), (4.31), and (4.32), we have

$$\mathrm{E}(X_r(k_0)) = \frac{1}{\sqrt{N}} \sum_{n=0}^{N-1} \mathrm{E}\left(\left(\alpha \sin(2\pi k_0 n/N + \phi) + q(n) \right) \operatorname{sgn}\left(\cos\left(\frac{2\pi k_0 n}{N} \right) \right) \right) \tag{4.53}$$

In (4.53), since $\mathrm{E}(q(n)) = 0$ and by assuming that phase ϕ of the signal is independent from its frequency, we have

$$\begin{aligned} \mathrm{E}(X_r(k_0)) &= \frac{1}{\sqrt{N}} \sum_{n=0}^{N-1} \\ &\alpha \left(\sin(2\pi k_0 n/N) \operatorname{sgn}\left(\cos(2\pi k_0 n/N) \right) \right) (\cos(\phi)) \\ &+ \alpha \left(\cos(2\pi k_0 n/N) \operatorname{sgn}\left(\cos(2\pi k_0 n/N) \right) \right) (\sin(\phi)). \end{aligned} \tag{4.54}$$

in which, we have

$$\frac{1}{\sqrt{N}}\sum_{n=0}^{N-1}\Big(\sin(2\pi k_0 n/N)\text{sgn}\left(\cos(2\pi k_0 n/N)\right)\Big) = 0, \tag{4.55}$$

and

$$\frac{1}{\sqrt{N}}\sum_{n=0}^{N-1}\Big(\cos(2\pi k_0 n/N)\text{sgn}\left(\cos(2\pi k_0 n/N)\right)\Big) = \frac{2}{\pi}\sqrt{N}, \tag{4.56}$$

From the above equations, we have

$$\text{E}(X_r(k_0)) = \frac{2\alpha}{\pi}\sqrt{N}(\sin(\phi)) \tag{4.57}$$

With similar calculations, we have

$$\text{E}(X_i(k_0)) = \frac{2\alpha}{\pi}\sqrt{N}(\cos(\phi)) \tag{4.58}$$

Since $\sin^2(\phi) + \cos^2(\phi) = 1$, for the non-centrality parameter of sign-sign- SDFT we have

$$c_{ss-SDFT} = \sqrt{(\text{E}(X_r))^2 + (\text{E}(X_i))^2} = \frac{2\alpha}{\pi}\sqrt{N}. \tag{4.59}$$

The same procedure may be applied to obtain the non-centrality parameters of the other SDFT methods. However, the following equations are required to calculate

them. We have

$$\frac{1}{\sqrt{N}}\sum_{n=0}^{N-1}\Big(\sin(2\pi k_0 n/N)\text{Round}\left(\sin(2\pi k_0 n/N)\right)\Big) = \frac{\sqrt{3N}}{\pi}, \tag{4.60}$$

$$\frac{1}{\sqrt{N}}\sum_{n=0}^{N-1}\Big(\sin(2\pi k_0 n/N)\text{Round}\left(\cos(2\pi k_0 n/N)\right)\Big) = 0. \tag{4.61}$$

The proof for (4.60) is given as an example.

It can be seen pictorially in Figure 4.5 that the depicted area (A) over 2π (the whole cycle) gives the result in (4.60). We have

$$A = 2\int_{\pi/6}^{\pi-\pi/6} \sin(y)\,\mathrm{d}y = 2\sqrt{3}. \tag{4.62}$$

$A\sqrt{N}/2\pi$ gives the value shown in (4.60).

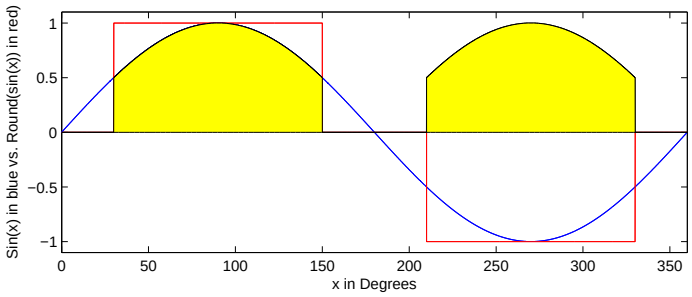

Figure 4.5: $\sin(x)$ vs. $\text{Round}(\sin(x))$ along with the area under their product.

4.2.5.3 Welch's-based estimation error variance

Welch's method is an averaging method in which periodograms of consecutive segments are linearly averaged to obtain a more accurate, asymptotically unbiased es-

timation of PSD with less estimation error variance. For M segments of N points each, the PSD obtained by Welch's method is given by

$$S(k) = \frac{1}{NM} \sum_{m=1}^{M} \left| \sum_{n=0}^{N-1} x(m,n) \exp(-2\pi i k n/N) \right|^2 . \tag{4.63}$$

which can be written as

$$S(k) = \frac{1}{M} \sum_{m=1}^{M} \left(X_{r,m}^2(k) + X_{i,m}^2(k) \right). \tag{4.64}$$

$X_{r,m}$ and $X_{i,m}$ are Gaussian random variables with variance σ_a^2 that are defined by (4.29) and (4.30) for DFT-based PSD estimation and by (4.31) and (4.32) for ss-SDFT-based one for the m^{th} segment.

In the absence of primary user signal, Welch's-based estimated PSD consists of $2M$ Gaussian distribution variables with zero mean, and thus follows a central chi-square distribution [65] given by

$$P_n^{Welch}(u) = \frac{1}{2^M \sigma_{w.S_0}^{2M} \Gamma(M)} u^{M-1} e^{-u/2\sigma_{w.S_0}^2} \quad , u \geq 0, \tag{4.65}$$

where $P_n^{Welch}(u)$ is the probability density function of the Welch's-based estimated PSD, subscript n represents the absence of signal, $\sigma_{w.S_0}^2$ is its variance in the absence of signal and $\Gamma(\cdot)$ is the Gamma function. The estimation error variance of the central

chi-square distribution with $n = M$ Gaussian contributors is given by [65]

$$\sigma^2_{w.S_0} = 2n\sigma^4_w, \tag{4.66}$$

where we have $\sigma^2_w = \sigma^2_a/M$ [59], [64]. Thus we have

$$\sigma^2_{w.S_0} = \sigma^4_a/M, \tag{4.67}$$

where σ^2_w is the estimation error variance of Welch's-based PSD and $\sigma^2_{w.S_0}$ is the estimation error variance of Welch's-based PSD in the absence of signal. σ^2_a is given in (4.35), (4.37) and (4.38) for different methods.

When the primary signal is present, the components follow a Gaussian distribution with mean m_r and m_i for real and imaginary components of the DFT coefficient in each segment. Welch's-based estimated PSD follows a non-central chi-square distribution [65] given by

$$P_S^{Welch}(u) = \frac{1}{2\sigma^2_{w.S_1}} \left(\frac{u}{c^2}\right)^{\frac{M-1}{2}} e^{\frac{-(c^2+u)}{2\sigma^2_{w.S_1}}} I_{M-1}\left(\sqrt{u}\frac{c}{\sigma^2_{w.S_1}}\right), \tag{4.68}$$

where $P_S^{Welch}(u)$ is the probability density function of the Welch's-based estimated PSD, subscript S represents the presence of signal, $\sigma^2_{w.S_1}$ is its variance in the presence of signal. The estimation error variance of Welch's method (when primary signal is

present) equals

$$\sigma^2_{w.S_1} = 2n\sigma^4_w + 4\sigma^2_w c^2 = \frac{4\sigma^4_a + 4\sigma^2_a c^2}{M}, \tag{4.69}$$

which equals to Equation 4.44 for periodogram's based method divided by number of periodograms M.

4.2.5.4 Welch's-based single tone detection case

False alarm rate for Welch's based PSD estimation for a single tone signal can be obtained by substituting (4.65) into (4.46). By doing repeated integration by parts, we have [65]

$$P_{fa-welch} = 1 - \left[1 - e^{-T/2\sigma^2_{w.S_0}} \sum_{l=0}^{M-1} \frac{1}{l!} \left(\frac{T}{2\sigma^2_{w.S_0}}\right)^l\right]^{N/2-1}, \tag{4.70}$$

where T denotes the decision threshold.

Detection rate for Welch's based PSD estimation for a single tone signal can be calculated by substituting (4.68) into (4.47). We have [65]

$$P_{d-welch} = 1 - \left[1 - e^{-T/2\sigma^2_{w.S_0}} \sum_{l=0}^{M-1} \frac{1}{l!} \left(\frac{T}{2\sigma^2_{w.S_0}}\right)^l\right]^{N/2-2} \times \left(1 - Q_M\left(\frac{c}{\sigma_{w.S_1}}, \frac{\sqrt{T}}{\sigma_{w.S_1}}\right)\right), \tag{4.71}$$

where Q_M represents the generalized Marcum Q function of the M^{th} order [59]. The

non-centrality parameter is given by

$$c = \sqrt{\frac{1}{M}\sum_{m=1}^{M}(\mathrm{E}(X_{r,m}))^2 + (\mathrm{E}(X_{i,m}))^2}. \tag{4.72}$$

By applying (4.48) into the above equation, we have

$$c_{welch-DFT} = \frac{\alpha}{2}\sqrt{N}, \tag{4.73}$$

which is equal to the one for periodogram-based method.

The analytical results of probability of detection (4.71) with respect to probability of false alarm (4.70) is shown in Figure 4.6 for different methods for single-tone detection. $M = 2$ segments of $N = 4$ points each along with $SNR = 0dB$ are considered. It can be seen that DFT-based method gives the best result followed by round-round SDFT and sign-sign-SDFT-based methods. sign-SDFT-based method exhibits the worst performance while round-SDFT is slightly better.

4.2.5.5 Welch's-based multi-tone detection case

A rectangular-like shape PSD is constructed by a multi-tone signal with the same sinusoid amplitudes (α in (4.45)) for all the tones. For a multi-tone signal with a

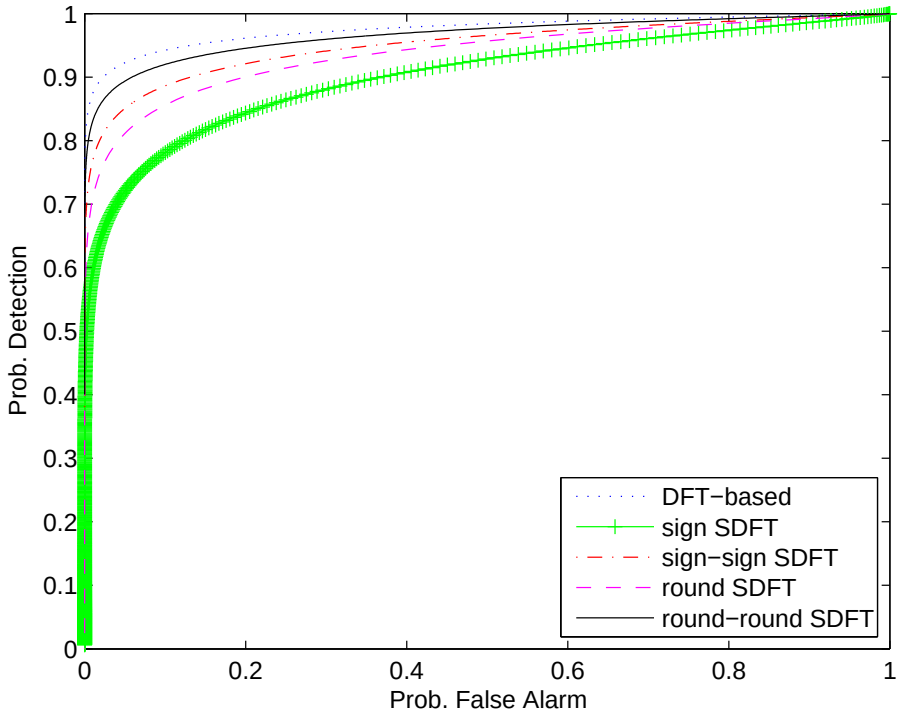

Figure 4.6: Numerical results of prob. detection vs. prob. of false alarm for single tone detection for all DFT and SDFT-based PSD estimation methods. $N = 4$. $M = 2.SNR = 0dB$.

total of K tones, (4.71) can be re-written as

$$P_{d-welch} = 1 - \left[1 - e^{-T/2\sigma^2_{w.S_0}} \sum_{l=0}^{M-1} \frac{1}{l!} \left(\frac{T}{2\sigma^2_{w.S_0}}\right)^l\right]^{N/2-1-K} \times \left(1 - Q_M\left(\frac{c}{\sigma_{w.S_1}}, \frac{\sqrt{T}}{\sigma_{w.S_1}}\right)\right)^K, \tag{4.74}$$

and (4.70) remains unchanged as the probability of false alarm is not a function of the presence of signal. Moreover, the non-centrality parameter is not a function of the number of signal, rather it is a function of its amplitude. Since the amplitudes of all the tones are the same in a signal with rectangular-like shape PSD, the non-centrality

of all the tones remain the same.

For $K = 2$ tones, $M = 2$ segments of $N = 4$ points each along with $SNR = 0dB$, the numerical results of probability of detection (4.74) with respect to probability of false alarm (4.70) are shown in Figure 4.7 for different methods. Still, it can be seen that DFT-based method gives the best result followed by round-round SDFT and sign-sign-SDFT-based methods. sign-SDFT-based method exhibits the worst performance while round-SDFT is slightly better.

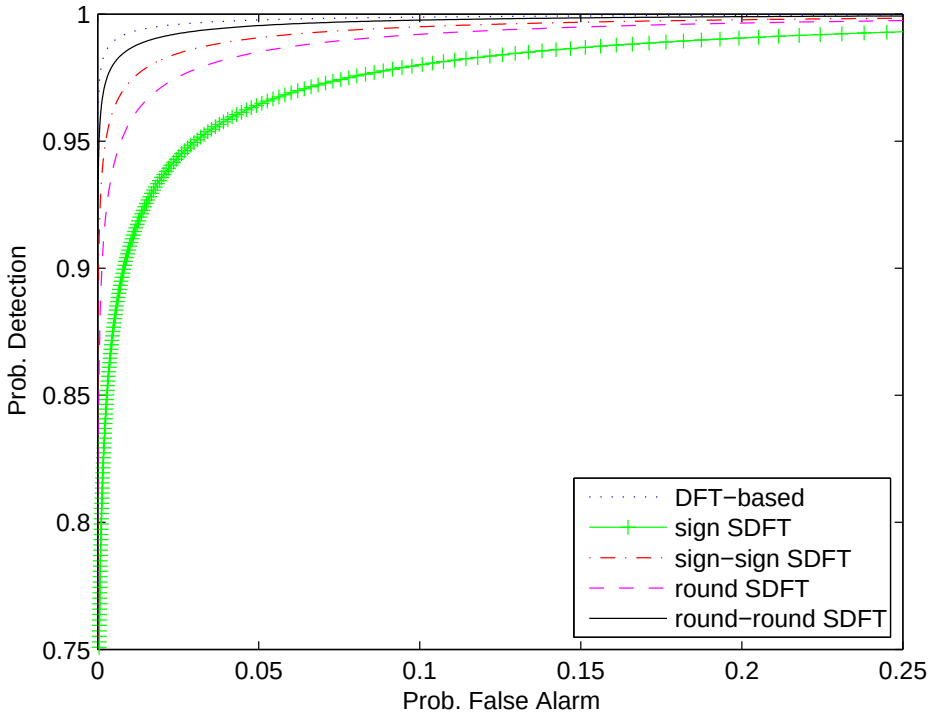

Figure 4.7: Numerical results of prob. detection vs. prob. of false alarm for multi-tone ($K = 2$ tones) detection for all DFT and SDFT-based PSD estimation methods. $N = 4$. $M = 2.SNR = 0dB$.

4.2.5.6 Optimum threshold for rounding function

Since it is desirable to reach the DFT-based PSD estimation performance, the best threshold level for rounding function (instead of traditional threshold level of 0.5) can be obtained by finding the best angle in which its associated non-centrality parameter (can be obtained with similar calculations as of the one for round-round SDFT method) equals to that of the DFT-based one.

$$\frac{2\alpha \sin(\theta)}{\pi}\sqrt{N} = \frac{\alpha}{2}\sqrt{N}, \tag{4.75}$$

or equivalently, we have

$$\sin(\theta) = \frac{\pi}{4}. \tag{4.76}$$

In this case, the associated Gaussian component variance is given by

$$\sigma^2_{a-opt-rr-SDFT} = \frac{2\theta}{\pi}\sigma_n^2 = 0.56\sigma_n^2, \tag{4.77}$$

which is closer to the one for DFT-based method ($0.5\sigma_n^2$) than the one for rr-SDFT-based method ($0.66\sigma_n^2$).

Therefore, the best angle in which the rounding function results in almost the same rr-SDFT-based PSD estimation error variance as of the DFT-based one is $\theta = 0.56\pi/2 = 0.28\pi = 52^o$ that gives a threshold level of $\cos(0.28\pi) = 0.6156$. Thus the

following optimum- rounding function (ORound(.)) is defined. We have

$$\text{ORound}(n) = \begin{cases} 1 & n \geq \cos(0.28\pi) = 0.6156 \\ 0 & \text{otherwise} \\ -1 & n \leq -0.6156 \end{cases} \tag{4.78}$$

4.2.6 WPT in PSD Estimation

The WPT and its applicability in PSD estimation is introduced in [62, 63]. The Haar-wavelet is the simplest wavelet transform that resembles SDFT transform because it is constructed by +1 and -1. All the other wavelet transforms are constructed by real numbers and thus their associated transform requires multiplications as well that makes them more complicated than both Haar-wavelet and SDFT conversions. The

Haar WPT matrix for an 8 by 8 matrix is given as

$$H_{8\times 8} = \begin{pmatrix} +1 & +1 & +1 & +1 & +1 & +1 & +1 & +1 \\ +1 & +1 & +1 & +1 & -1 & -1 & -1 & -1 \\ +1 & +1 & -1 & -1 & +1 & +1 & -1 & -1 \\ +1 & +1 & -1 & -1 & -1 & -1 & +1 & +1 \\ +1 & -1 & +1 & -1 & +1 & -1 & +1 & -1 \\ +1 & -1 & +1 & -1 & -1 & +1 & -1 & +1 \\ +1 & -1 & -1 & +1 & +1 & -1 & -1 & +1 \\ +1 & -1 & -1 & +1 & -1 & +1 & +1 & -1 \end{pmatrix}. \tag{4.79}$$

By swapping the rows of the Haar-WPT matrix, it can be re-ordered in terms of frequency. In this chapter, the frequency ordered version of Haar-WPT is applied for PSD estimation. The procedure of estimating the PSD is the same as the one using DFT and SDFT except for the fact that the frequency ordered WPT matrix is used instead of DFT and/or SDFT matrices in Welch's algorithm.

Simulation result of Haar-WPT-based PSD estimation is shown in Figure 4.8. As it can be seen from that figure, the WPT-based Welch's PSD estimation method does not accurately detect the actual edges of PSD. The simulations are performed using 100 segments of 1024 points each in noise free scenario. The estimated PSD of the signal spectrum is shown in the middle subplot while the actual signal spectrum shaper filter is shown at the top. It is compared with the PSD obtained by sign-SDFT

shown at the bottom. This figure shows how inferior WPT-based PSD estimation method is in locating the frequency edges regardless of the fact that it is less complex.

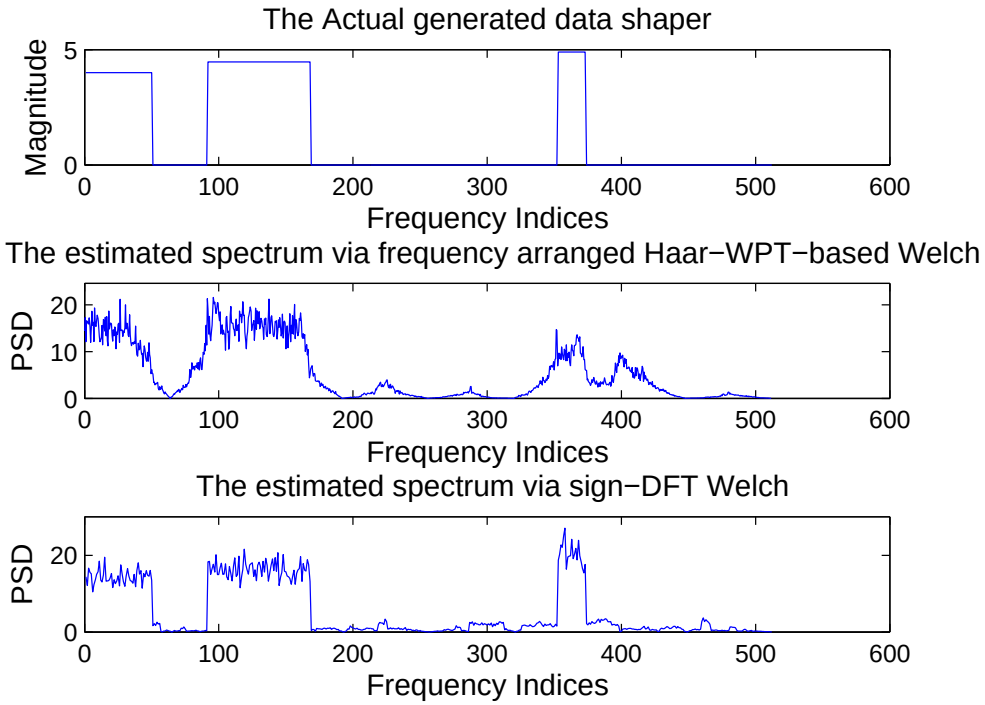

Figure 4.8: The actual signal spectrum shaper filter shown at the top and its estimated PSD shown in the middle using frequency ordered Haar-WPT-based Welch's algorithm. It is compared with the PSD obtained by sign-SDFT shown at the bottom. $SNR = \infty$.

It is worth noting that if we compare the sign-SDFT matrix to the Haar-WPT matrix, we can find an interesting relationship between them which is shown in Table 4.1 for the 8 by 8 matrices. By comparing the matrix in (4.79) and the one in (4.15), we can see that the matrices can be converted to each other based on Table 4.1. It shows that sign-SDFT can be seen as a modified version of Haar-WPT.

Table 4.1: Sign-SDFT to Haar-WPT Conversion Table

Haar WPT	**sign-SDFT**
Row 1	Row 1
Row 2	(1 column Shifted to the left) of row 2
Row 3	Row 3
Row 4	Row 8
Row 5	Row 5
Row 6	(2 columns Shifted to the left) of row 4
Row 7	Row 7
Row 8	(3 columns Shifted to the left) of row 6

It might seem to be confusing that even frequency re-ordered HWPT (which constructs Walsh matrices) does not outperform both DFT and SDFT in the edge detection procedure. By referring to Table 4.1 as an example, it can be seen that the problem arises due to miss-placement of the frequency bins in HWPT whereas both DFT and SDFT place the PSD energy levels at the right frequency.

4.2.7 Complexity Comparison

In the process of time to frequency domain conversion of SDFT methods, no multipliers are required. This results in a less computationally complex method for PSD estimation compared to DFT method. The complexity comparison table of converting a block of N samples from time domain to frequency domain for two methods of DFT and SDFT along with radix-2 FFT is provided in Table 4.2. Reduction of $N \times N$ complex multipliers for DFT method and $N \times \log_2(N)$ complex multi-

Table 4.2: Complexity Comparison Table of SDFT and DFT Conversions

Method	**No. (complex) Multiplications**	**No. (complex) Additions**
DFT	$N \times N$	$N \times N$
SDFT	0	$N \times N$
radix-2 FFT	$N \times \log_2(N)$	$N \times \log_2(N)$

plications for radix-2 FFT in the process of PSD estimation is obtained by SDFT method. Comparing SDFT by radix-2 FFT, we can conclude that although number of required additions in radix-2 FFT is lower than the one for SDFT method, the number of required multiplications is higher in radix-2 FFT. Since multiplication is generally more complex than addition, the complexity of SDFT methods can be lower than even FFT methods in certain conditions depending on the number of digits of each multiplicand and the chosen multiplication algorithm. One way to improve the complexity of SDFT methods compared to FFT method is to develop simplified FFT techniques that may be suggested as a future research subject. In the case of sign-sign, round-round SDFT and DFT, the operation (multiplication and addition) is complex. Each complex multiplication includes 4 real multiplications and 2 real additions while each complex addition requires 2 real additions.

4.3 Simulation Results

For a wideband signal with 29% of spectrum occupancy, the simulation results of obtaining the PSD and its edges using both sign-SDFT and DFT-based methods are

shown in Figures 4.9 and 4.10 respectively where the actual generated transmitted data shaper is shown at the top subplot, the estimated spectrum is shown in the middle and the first derivative of the obtained PSD which is used to detect the edge locations, is shown at the bottom subplot. The SNR of the strongest subband in these simulations is $SNR = 10$ dB and the other two subbands are 2 and 1 dB weaker than the strongest. SNR is calculated individually over various subbands and is defined as the ratio of the signal power in each subband to the noise power in that subband. The simulation results are derived from 100 non-overlapping frames of 1024 samples each using Welch's method.

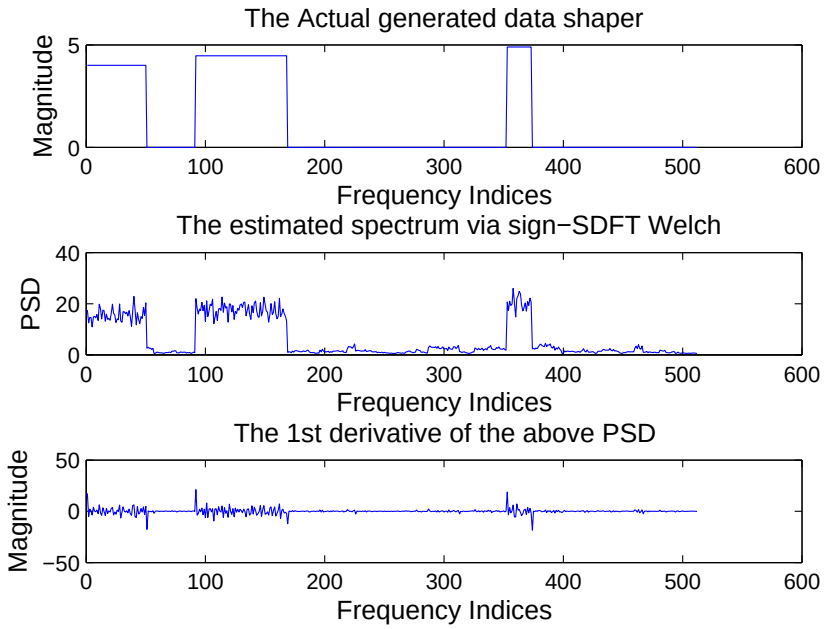

Figure 4.9: Spectrum sensing based on the sign-SDFT matrix. Strongest subband's $SNR = 10$ dB. Spectrum occupancy=29%.

For the signal whose PSD shaper is shown in top subplot of Figure 4.10, the edge

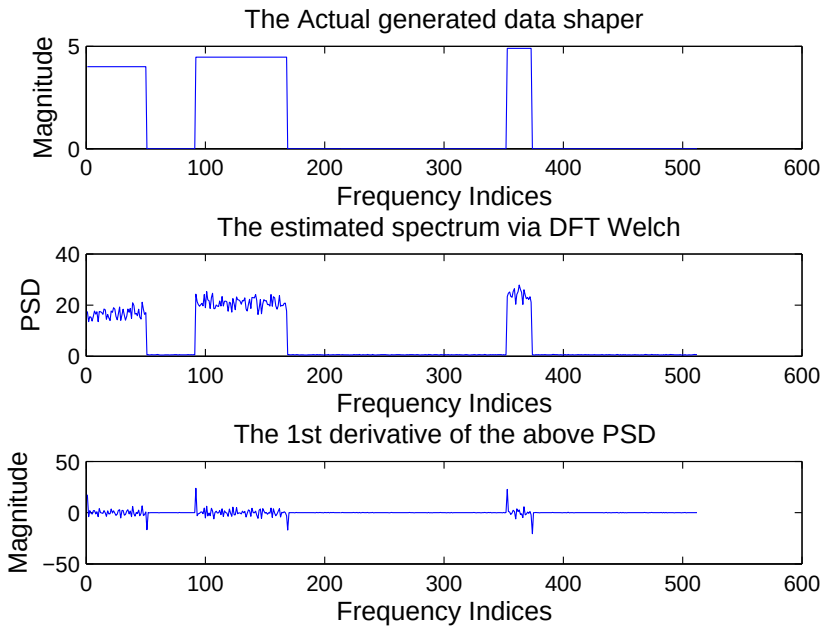

Figure 4.10: Spectrum sensing based on the DFT matrix. Strongest subband's $SNR = 10$ dB. Spectrum occupancy=29%.

detection rate curves of different SDFT-based methods along with the one for DFT-based method versus SNR are shown in Figure 4.11 for different SDFT-methods. The SNR is considered as the SNR of the strongest subband and the other two subbands are 2 and 1 dB weaker than the strongest one. The simulation results are derived from 100 non-overlapping frames of 1024 samples each using Welch's method.

In Figure 4.12, the detection rate curves are given for the case of 78% of spectrum occupancy instead of 29%. As can be seen from that figure, the performance degradation of SDFT gets higher when the spectrum occupancy increases. This fact shows that these methods show better performance in the case of low spectrum occupancy which is a reasonable premise of cognitive radio.

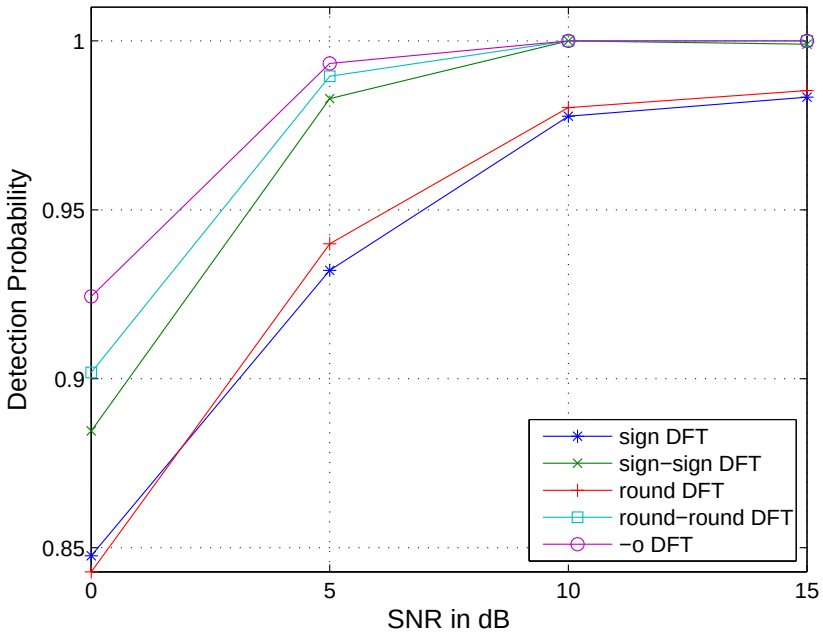

Figure 4.11: The detection rate w.r.t. the strongest subband's SNR for both DFT and SDFT methods using consecutive samples differentiation method. N=1024, M=100, Spectrum Occupancy=29%.

It can be seen from the performance curves that the performance rates of two methods merge at some SNR level showing that the additional complexity of DFT-based method does not improve the performance beyond that level of SNR compared to the SDFT based methods. Moreover, in low SNR scenarios, the difference between the performance curves is not high enough to justify the additional complexity for the DFT-based methods.

By comparing different methods of SDFT, we can conclude that sign-SDFT has the worst performance while the round-SDFT exhibits better performance than the sign one due to better approximation of the DFT matrix. Sign-sign-SDFT improves the

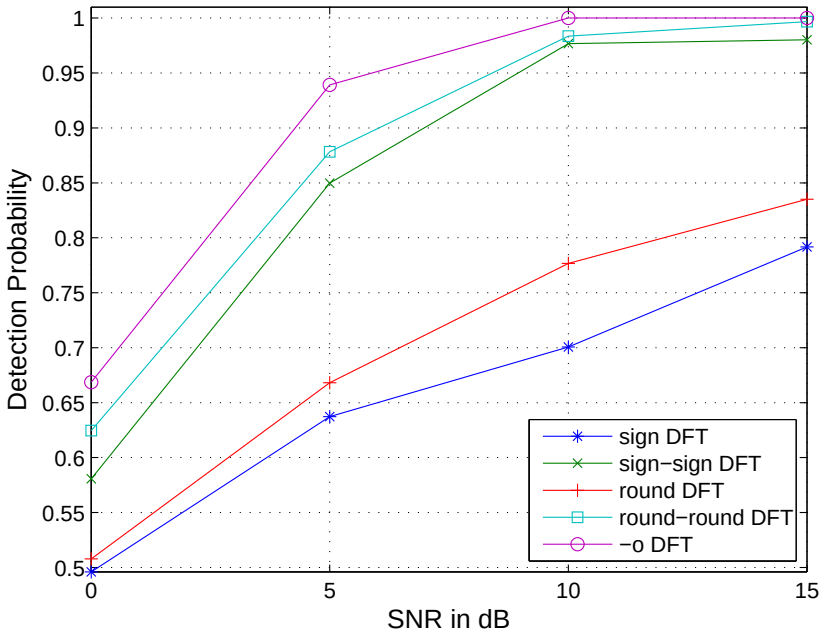

Figure 4.12: The detection rate w.r.t. the strongest subband's SNR for both DFT and SDFT methods using consecutive samples differentiation-base edge detection method. N=1024, M=100, Spectrum Occupancy=78%.

performance compared to sign and round SDFT methods at the expense of increasing complexity. Finally, the round-round-SDFT shows the best performance almost as accurate as the one for DFT-based method.

The detection rates of different rounding thresholds are shown in Figure 4.13. The simulation results show that threshold of 0.615 gives an optimum threshold compared to both threshold of 0.5 which represents the traditional rounding function and threshold of 0.38. The simulation results are derived from 100 non-overlapping frames of 1024 samples each using Welch's method. The received signal has three occupied subbands with spectrum occupancy=78%. The SNR is considered as the

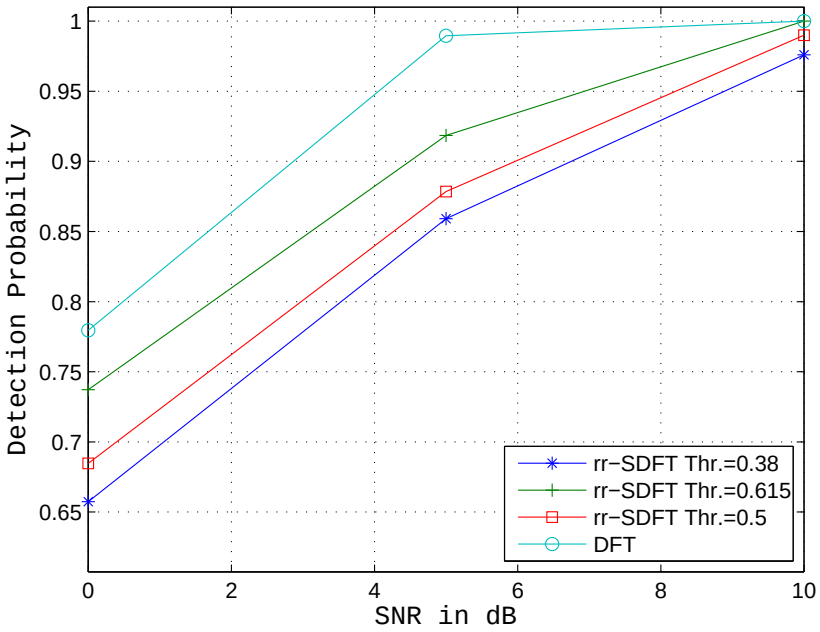

Figure 4.13: The detection rate w.r.t. the strongest subband's SNR for different rounding threshold levels of round-round SDFT method. N=1024, M=100, Spectrum Occupancy=78%.

SNR of the strongest subband and the other two subbands are 2 and 1 dB weaker than the strongest one.

Then, an actual spectrum shaper with the shape of $\text{sinc}^2(\cdot)$ function has been used instead of a rectangular-like filter. For the signal whose PSD shaper is shown in top subplot of Figure 4.14, its PSD are obtained and shown in the middle and bottom subplot of Figure 4.14 for DFT-based and sign-SDFT- based PSD estimation methods. The edge detection rate curves of different SDFT-based methods along with the one for DFT-based method versus SNR are shown in Figure 4.15 for different SDFT-methods. The modified window-averaging edge detection method has been

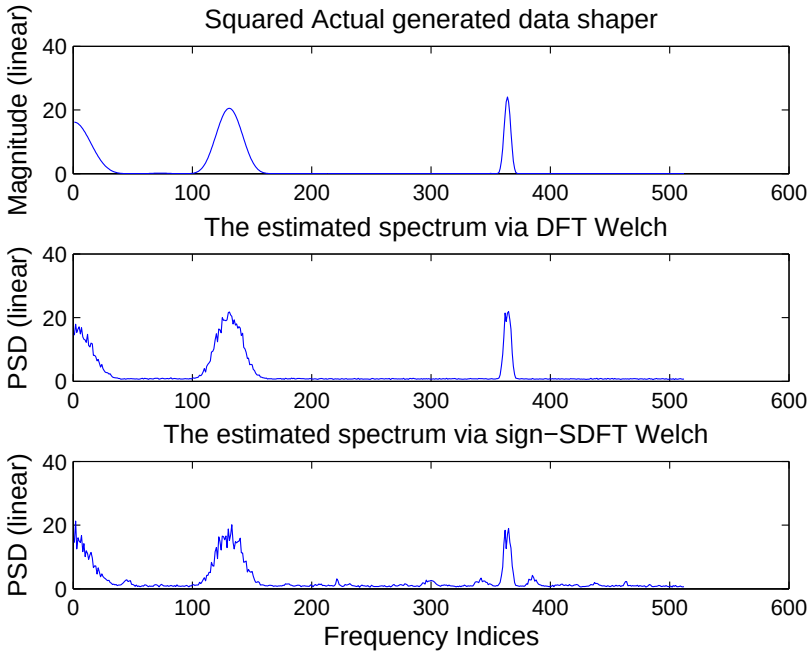

Figure 4.14: PSD obtained by two methods (middle and bottom) along with the spectrum shaper (top). Strongest subband's $SNR = 15$ dB. Spectrum occupancy=29%.

used to detect the edges in this simulation. The SNR is considered as the SNR of the strongest subband and the other two subbands are 2 and 1 dB weaker than the strongest one. The simulation results are derived from 100 non-overlapping frames of 1024 samples each using Welch's method.

It can be seen from Figures 4.14 and 4.15 that the detection rate curves are very close and different mentioned methods are capable of detecting the edges with similar performances especially in higher SNR scenarios.

Simulation results and mathematical analysis confirm the comparable performance of the proposed simplified methods despite the reduced complexity.

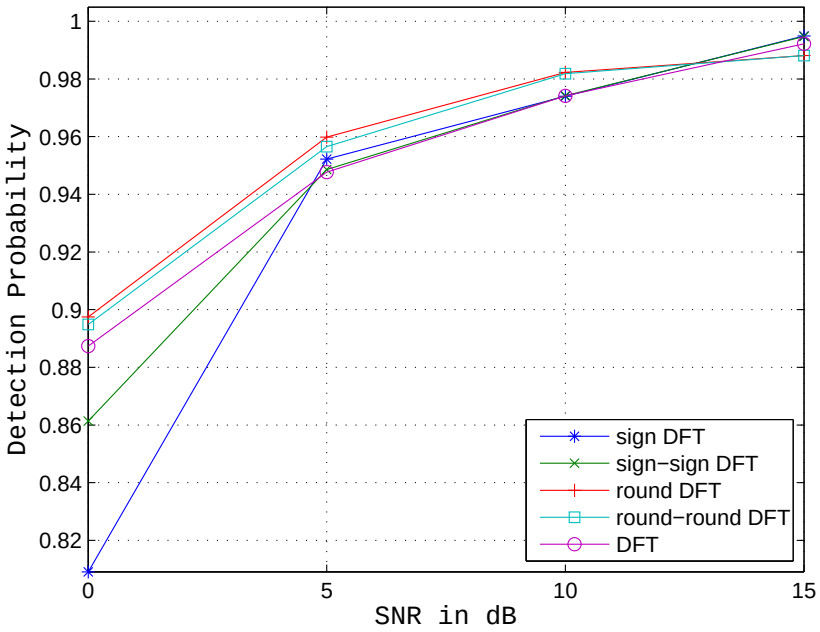

Figure 4.15: The detection rate w.r.t. the strongest subband's SNR for both DFT and SDFT methods with $\text{sinc}^2(\cdot)$ spectrum shaper using modified window-averaging edge detection method. N=1024, M=100, Spectrum Occupancy=29%.

4.4 Conclusion

In this chapter, new methods of spectrum sensing based on simplified DFT matrices are introduced. The reduced complexity of the simplified DFT matrix is shown and its performance is compared to that of the traditional DFT-based methods. The proposed methods can be used as an alternative for spectrum sensing in CR since, it is the edge locations that are important, rather than the exact shape of the PSD. The simulation results and mathematical analyses are given to compare the new methods performances to that of the DFT-based spectrum sensing method. Simulations show better performance curves in case of low spectrum occupancy making them suit-

able for spectrum sensing in CR where the low spectrum occupancy is a reasonable assumption.

Chapter 5

A Novel Reduced Power Compressive Sensing Technique for Wideband Cognitive Radio

5.1 Introduction

A cognitive radio system (CR) [5, 46] improves the spectrum utilization by allowing secondary users (SU) to access unused licensed spectrum. Moreover, it assesses its environment and adapts its parameters (e.g. the frequency and power of transmission) to reduce power consumption while having a reliable communication. One reason for increased power consumption is due to electromagnetic pollution. As more wideband access systems are designed, the underlying electromagnetic noise floor

increases which in turn requires licensed users to increase their transmit power to maintain required signal to noise ratios. CR adds little if any to the noise floor by allowing secondary users access to the unused bands. Furthermore, by reducing the power consumption of the secondary users themselves, we can significantly increase transmitted data volumes without a large increase in power consumption. Along with reducing peoples exposure to electromagnetic waves, this makes it an excellent candidate for green technology [66].

Irrespective of the above steps, wideband spectrum sensing requires high rate analog to digital (A/D) converters with the associated high power consumption. Compressive sensing is a candidate for reduced power consumption in CR [67].

Compressive sensing uses a sub-Nyquist rate sampler to sense the received signal [35]. It was shown in [68] that despite the sub-Nyquist sampling rate, compressive sensing can recover the signals that are sparse or nearly sparse in one domain with some limits introduced in [69]. In [70], a simple least square reconstruction technique was used to recover the samples. Since the frequency edge vector of the received signal in CR has a nearly sparse nature, compressive sensing can be used to recover the edge locations of the PSD in CR [36]. The recovery algorithm of compressive sensing (l_1 minimization algorithm) is computationally complex, and thus time and energy consuming and cannot be easily implemented for real-time applications such as in CR.

In this chapter, we propose a new algorithm for compressive sensing to be used

in spectrum sensing in CR. We show by simulations and analysis that the proposed sub-Nyquist rate non-uniform sampler allows for accurate detection of the edges of PSD and consumes much less power than the conventional sensing method. The proposed sampler samples only some portions of the received signal and switches off the A/D converter based on a predefined pattern to reduce power consumption. Since the received signal samples are correlated, the missing samples can be estimated. We propose to use expectation-maximization (EM) technique [42, 43] to estimate these samples. It is shown that the combined sub-Nyquist sampler and EM algorithm consume much less power than Nyquist rate A/D converter making the proposed algorithm a viable low-power solution for spectrum sensing and thus extending the battery life of the CR.

5.2 System Model of Compressive Sensing Technique for Wideband Cognitive Radio

The compressed sampling procedure can be expressed in matrix format as

$$\mathbf{x_c} = \beta \cdot \mathbf{x}, \tag{5.1}$$

where $\mathbf{x_c}$ is the compressed sampling received signal vector of size $P \times 1$, $\mathbf{x}$ is the Nyquist rate sampled received signal vector of size $N \times 1$ ($P \preceq N$), and β is the

compressive sampling matrix of size $P \times N$. When $\beta = I_N$ (I_N is the identity matrix of size N), the Nyquist sampling rate is achieved. If $\beta = D_N$ (D_N is the DFT matrix of size N), the frequency domain sampling is obtained. For compressive sensing purposes, we can simply eliminate some rows of the identity matrix to achieve the matrix β of the compressed dimension. This elimination may be done on a random basis as is done in [36]. For example, for a 4×4 identity matrix with compression ratio of 0.75, we have

$$\beta_{3\times 4} = \begin{pmatrix} 1 & 0 & 0 & 0 \\ 0 & 1 & 0 & 0 \\ 0 & 0 & 0 & 1 \end{pmatrix}, \tag{5.2}$$

in which the third row of identity matrix is deleted.

5.2.1 Spectrum Sensing Revisit

In Welch's method, the received signal samples are segmented into M segments of length N. The estimated PSD ($\mathbf{S}$) is achieved by linearly averaging the periodograms of all segments as

$$\mathbf{S} = \frac{1}{M} \sum_{m} \mathbf{S_m}, \tag{5.3}$$

where $\mathbf{S_m}$ is the m^{th} segment's periodogram. The periodogram of each segment is given by

$$\mathbf{S_m} = \frac{|\mathbf{X_m}|^2}{N}, \tag{5.4}$$

where $\mathbf{X_m}$ is the DFT sequence of the m^{th} segment defined as

$$\mathbf{X_m} = [X_{m1}, X_{m2}, \cdots, X_{mN}] \tag{5.5}$$

and we have

$$|\mathbf{X_m}|^2 = \left[|X_{m1}|^2, |X_{m2}|^2, \cdots, |X_{mN}|^2\right]. \tag{5.6}$$

The estimation error variance of Welch's method is inversely proportional to the number of segments (M) involved in the averaging process. We have [25]

$$\sigma_{\mathbf{S}}^2 \simeq \frac{\sigma_{\mathbf{S_m}}^2}{M}, \tag{5.7}$$

in which $\sigma_{\mathbf{S}}^2$ represents the estimation variance of Welch's method and $\sigma_{\mathbf{S_m}}^2$ is the estimation error variance for the m^{th} segment's periodogram.

After PSD estimation, the edges are detected. Different methods of edge detection for wideband spectrum sensing are developed in [39]. A modified version of window-averaging based edge detection technique introduced in section 4.2.1 has been applied in this chapter.

5.2.2 EM Algorithm Procedure

The EM algorithm is an algorithm implementing maximum likelihood estimation. It can be applied to a set of data when their stochastic model is known, although the

parameters of the model might be unknown [43]. The EM is an iterative algorithm which works as follows [43]:

1. Calculate the expected value of the log-likelihood function of the conditional probability distribution of the missing variables given the observed ones. This expected value is considered to be the current estimate of the missing points.

2. Maximize the above-mentioned distribution with respect to the parameters of the estimation such as mean, variance and covariance of the log-likelihood function. The parameters maximizing the distribution are used for the next expectation step.

3. Iterate the above-mentioned steps until convergence.

4. The maximum likelihood estimation of the missing variables is obtained after convergence.

5.3 Estimation of Missing Samples in Compressive Sensing for CR

In this paper, we propose to estimate the missing points of the sub-Nyquist sampled received signal in the time domain by applying the EM algorithm. A non-uniform sub-Nyquist rate sampler is applied to the received signal of $M \times N$ matrix (recall that M is the number of segments and N is the number of points in each segment.).

As is shown in Figure 5.1, the non-uniform sampler works as follows:

1. The sampler provides all samples in the first segment of a set of M_1 segments.

2. For the next $(M_1 - 1)$ segments, the sampler samples only the first N_1 points of each segment and is turned off for the rest of this segment.

3. For the $(M_1 + 1)^{\text{th}}$ segment, we restart the process by repeating steps 1 and 2.

The fully sampled first segment and the N_1 points in each subsequent segment are used along with the EM algorithm to estimate the missing samples.

Equivalently, for the $(m, n)^{th}$ element of the received signal matrix, the A/D converter is switched on when either $\text{Rem}(m/M_1) = 1$ or $\text{Fix}((n-1)/N_1) = 0$ in which Rem(.) takes the remainder of a division and Fix(.) gives the quotient of a division.

Since the received signal samples are mixed with a Gaussian noise, it is assumed that each segment has a Gaussian distribution. Since the received signal samples are correlated, it is assumed that all segments construct a bi-variate Gaussian distribution with the adjacent segments.

5.3.1 EM algorithm for Bi-variate Gaussian distribution

Let $\mathbf{x_1}$ be the first segment (the known segment) and $\mathbf{x_m}$ be the m^{th} segment of the received signal samples. The first parts of each segment are known and the other parts are unknown and to be estimated by EM algorithm. The estimated missing points converge to their actual value after some iterations in EM algorithm [43].

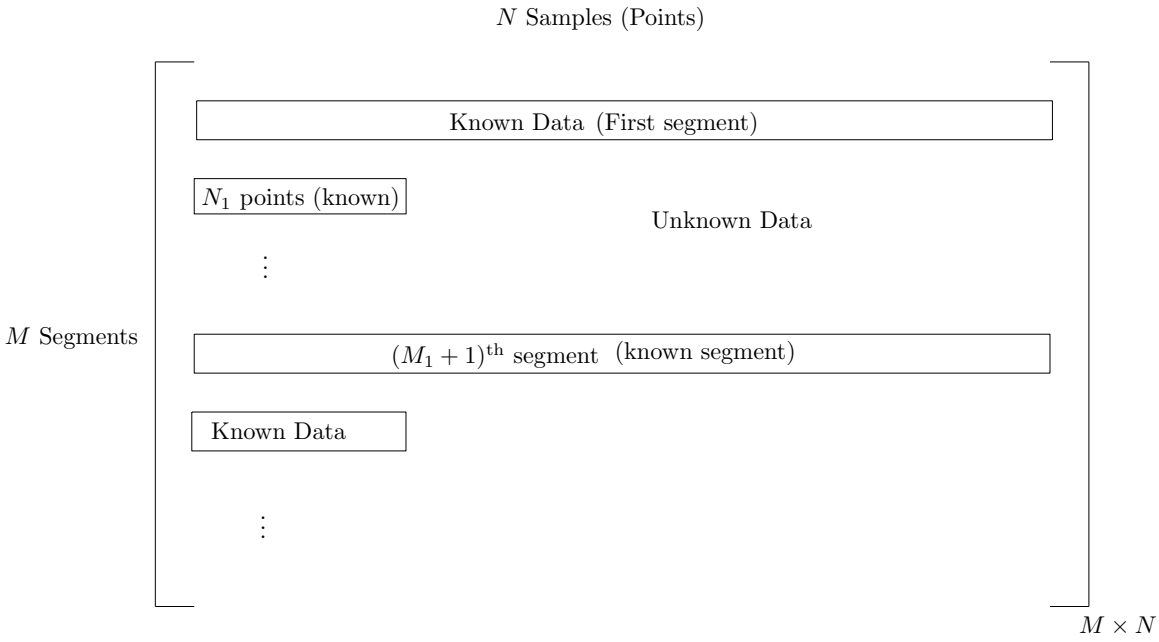

Figure 5.1: Non-uniform sampling pattern.

Since, the received signal samples over consecutive windows are assumed to construct a bi-variate Gaussian distribution, the conditional distribution of missing variables given the observed ones has normal distribution with mean [43] (representing the expected value of missing points of $\mathbf{x_{m+1}}$ in expectation step of EM) given by:

$$\begin{aligned} &\mathrm{E}\left(x_{m+1}(n)\right) = \mu_{m+1} + \frac{\sigma^2_{m,(m+1)}}{\sigma^2_{m,m.m-1}}\left(x_m(n) - \mu_m\right), \\ &n = \{N_1 + 1 : N\}, \\ &m = \{2 : M_1, M_1 + 2 : 2M_1, \cdots, M - 1\}, \end{aligned} \tag{5.8}$$

where μ_m is the mean of the m^{th} segment at each iteration given by

$$\mu_m = \frac{1}{N}\sum_n x_m(n), \tag{5.9}$$

$\sigma^2_{m,(m+1)}$ is the covariance of the m^{th} segment and its consecutive segment given by

$$\sigma^2_{m,(m+1)} = \frac{1}{N}\left(\sum_n x_m(n)x_{m+1}(n)\right) - \mu_m\mu_{m+1}, \tag{5.10}$$

and $\sigma^2_{m,m.m-1}$ is the variance of the conditional distribution of missing variables in the m^{th} segment given the observed ones in the $(m-1)^{\text{th}}$ segment given by [43]

$$\sigma^2_{m,m.m-1} = \sigma^2_{m,m} - \sigma^4_{m-1,m}/\sigma^2_{m-1,m-1}, \tag{5.11}$$

in which $\sigma^2_{m,m}$ is given by

$$\sigma^2_{m,m} = \frac{1}{N}\left(\sum_n x^2_m(n)\right) - \mu^2_m. \tag{5.12}$$

The above-mentioned procedure to estimate the means, variances and covariances of different segments is the maximization step of EM algorithm.

After a few iterations, the unknown elements of each segment are estimated. Each segment is built based on its preceding segment. The preceding segment is either fully known or partially estimated by the EM algorithm. Therefore, it is not necessary to wait for all segments to be received. This makes the proposed algorithm suitable for real time applications as it does not require a large buffer or long processing time. The required processing time depends on the processor speed.

After estimating the missing samples, Welch's method is applied to estimate the

PSD and the edges.

5.3.2 Analysis of Applying EM to Spectrum Sensing

The frequency bin values of each segment using DFT transformation are given by

$$X_{m+1}(k) = \sum_{n=0}^{N-1} x_{m+1}(n) e^{-2\pi jkn/N}. \tag{5.13}$$

From Equations 5.13 and 5.8, we have ($\forall k$)

$$\mathrm{E}\left(X_{m+1}(k)\right) = \sum_{n=0}^{N-1} e^{-2\pi jkn/N} \times \left[\frac{\sigma^2_{m,(m+1)}}{\sigma^2_{m,m.m-1}} x_m(n) + \mu_{m+1} - \frac{\sigma^2_{m,(m+1)}}{\sigma^2_{m,m.m-1}} \mu_m \right]. \tag{5.14}$$

Since $\sum_{n=0}^{N-1} e^{-2\pi jkn/N} = 0$ and by applying Equation (5.13) into Equation (5.14), Equation (5.14) can be re-written as

$$\mathrm{E}\left(X_{m+1}(k)\right) = \frac{\sigma^2_{m,(m+1)}}{\sigma^2_{m,m.m-1}} X_m(k) \quad \forall k \tag{5.15}$$

In the EM algorithm, the expected value of the variable is chosen as its final value ($\mathrm{E}\left(X_{m+1}(k)\right) = X_{m+1}(k)$). Thus we have

$$X_{m+1}(k) = \frac{\sigma^2_{m,(m+1)}}{\sigma^2_{m,m.m-1}} X_m(k) \quad \forall k. \tag{5.16}$$

Based on Welch's method, the PSD is obtained by

$$S(k) = \frac{1}{NM} \sum_{m=1}^{M} \left| X_m(k) \right|^2 \quad \forall k. \tag{5.17}$$

The estimation variance of the EM algorithm -based Welch's method equals that of Welch's method [25]. We have

$$\sigma_{\mathbf{S}}^2 \simeq \frac{\sigma_{\mathbf{S_m}}^2}{M}, \tag{5.18}$$

in which $\sigma_{\mathbf{S}}^2$ represents the estimation variance of Welch's method and $\sigma_{\mathbf{S_m}}^2$ is the estimation error variance for the m^{th} segment's periodogram.

By substituting Equation (5.16) into Equation (5.17), we have ($\forall k$)

$$S(k) = \frac{1}{NM} \left| X_1(k) \right|^2 \left[1 + \sum_{m'=1}^{M-1} \frac{\prod_{m=1}^{m'} \sigma_{m,(m+1)}^4}{\prod_{m=1}^{m'} \sigma_{m,m.m-1}^4} \right]. \tag{5.19}$$

The term $\left| X_1(k) \right|^2$ is equivalent to its expected value $\mathrm{E}\left(\left| X_1(k) \right|^2 \right)$ in the EM algorithm. Thus Equation (5.19) can be re-written as ($\forall k$)

$$S(k) = \frac{\mathrm{E}\left(\left| X_1(k) \right|^2 \right)}{NM} \left[1 + \sum_{m'=1}^{M-1} \frac{\prod_{m=1}^{m'} \sigma_{m,(m+1)}^4}{\prod_{m=1}^{m'} \sigma_{m,m.m-1}^4} \right]. \tag{5.20}$$

It can be seen from Equation (5.20) that the PSD obtained by EM algorithm has a scaling factor (shown in brackets) that is frequency-independent and therefore

the PSD shape obtained after the application of the EM algorithm is not distorted compared to the one obtained by sampling above the Nyquist rate.

5.4 Power Consumption Comparison

The idea behind intermittently switching off the A/D converter is to reduce the power consumption and increase the battery life. To compare the power consumption of compressive and non-compressive methods, we calculate the power consumption of the EM algorithm that is additional to reduced power of the compressive sensing algorithm.

The A/D power consumption is linearly proportional to the sampling rate and thus to the number of received samples in each time frame [71]. Moreover for zero-crossing based ADC, the static power consumption is zero [72]. We have,

$$P_c = C_r \times P_{nc} + P_{EM}, \tag{5.21}$$

where P_c, P_{nc} and P_{EM} are the power consumption of compressive sensing method, non-compressive sensing method and EM algorithm, respectively. C_r is the compression ratio and is given by

$$C_r = \frac{1}{M_1 N}\left((M_1 - 1)N_1 + N\right). \tag{5.22}$$

From Equations 5.8, 6.13 , 6.14 ,and 5.11, the whole procedure to update the missing points based on the EM algorithm requires approximately of $6N \times M$ additions and $4N \times M$ multiplications, a total of $10N \times M$ operations (either addition or multiplications) for each iteration. Therefore, power consumption of EM algorithm is given by

$$P_{EM} = P_i \times O \times I, \tag{5.23}$$

where P_i is the power consumption per instruction, O is the number of operations, and I is the number of iterations. The power efficiency (η) of the system is defined by

$$\eta = \frac{P_{nc}}{P_c}. \tag{5.24}$$

The system is efficient when $\eta > 1$.

5.4.1 Reduced Power A/D Converter System Design Example

Power consumption of two cases of compressive and non-compressive sensing is subject to proper design of the system, especially proper selection of ADC and processor. The proposed system is efficient only if P_c is much lower than P_{nc} ($\eta > 1$) with the proper design of the system. An example is given in this subsection that is one possible design of the system.

Assume we have an A/D converter working at the rate of 100 Msamples/sec.

Assume the received signal consists of $M = 100$ segments of $N = 1024$ points. With this A/D converter, it takes about 1 ms to sense $M \times N \simeq 100,000$ samples of the received signal. With $I = 15$ iterations and $10N \times M$ operations, the EM algorithm requires $15 \times 10 \times 100,000 = 15$ million operations per 1 ms which is equivalent to 15 GOPS (Giga operations per second). A processor with power efficiency of x GOPS/mW, is chosen. We have

$$P_{EM} = \frac{15\text{GOPS}}{x\text{GOPS/mW}} = \frac{15}{x}\text{mW}. \tag{5.25}$$

For a system with a compression ratio of $C_r = 0.1$ and power efficiency of ($\eta > 1$), we have:

$$\eta = \frac{P_{nc}}{P_c} = \frac{P_{nc}}{C_r \times P_{nc} + P_{EM}} = \frac{P_{nc}}{0.1 \times P_{nc} + \frac{15}{x}} > 1. \tag{5.26}$$

Equivalently, we have

$$x > \frac{16.6667}{P_{nc}}\text{GOPS/mW}. \tag{5.27}$$

This will give us the boundary limit on the combination of ADC and processor that a designer can choose.

For example, if we select a 1.2V 250mW 14b 100 MS/s digitally calibrated pipeline ADC in 90 nm CMOS which consumes $P_{nc} = 250$mW [73], then from (5.27), we require a processor with an efficiency of $x = 0.4$GOPS/mW in order to achieve a power savings of a factor of 4 ($\eta = 4$). From [74], it is shown that processors can have

efficiencies up to 17.3 GOPS/mW, therefore the above power savings is achievable with readily available processors.

To verify the applicability of the proposed method, simulation results for the above-mentioned case are presented in the following section.

5.4.2 Complexity Comparison of Compressive and Non-Compressive Sensing Methods

Complexity of non-compressive and EM-based compressive sensing methods are compared in Table 5.1. The complexity order of Welch's method is given by $O(N^3)$ [25] and complexity order of EM algorithm is given by $10INM$ in which I is the number of iterations. M is the number of received signal segments and N is the number of samples in each segment. For the given example, it can be seen that the complexity of EM-based compressive sensing is of the same order as of the non-compressive sensing technique.

Table 5.1: Complexity Comparison Table of Non-compressive and EM-based Compressive Sensing Methods

Method	**Complexity order**	**for the given example**
Non-compressive	$O(N^3)$	$O(10^9)$
EM-based compressive	$O(N^3) + 10INM \approx O(N^3)$	$10^9 + 1.5 \times 10^7 \approx O(10^9)$

5.5 Simulation Results

For a wideband signal with 29% of spectrum occupancy, the simulation results of obtaining the PSD using both compressive and non-compressive sensing methods are shown in Figure 5.2 where the actual frequency shaper filter is shown at the top subplot, the PSD obtained by both compressive and non-compressive sensing methods are shown at the bottom subplot. The signal to noise ratio (SNR) of the strongest subbands in these simulations is $SNR = 2$ dB and the other subband is 3 dB weaker. SNR is calculated individually over various subbands and is defined as the ratio of the signal power in each subband to the noise power in that subband. The simulation results are derived from 100 non-overlapping frames of 1024 samples each using Welch's method. For the compressive sensing method, the whole first segment along with the first 128 points of the other segments are sampled. For $M_1 = M = 100$ segments and $N_1 = 128$, the compression ratio is 13%. The remaining unknown data are estimated using the EM algorithm for 15 iterations. It can be seen from Figure 5.2 that although the PSD for the compressed data has lower values than the non-compressive sensing one, the edges of the PSD are maintained. The power consumption calculations for this case are given in the previous section.

For the signal whose PSD is shown in Figure 5.2, the simulation results of the root mean square error (RMSE) of the edge frequency bins versus the number of iterations of the EM algorithm (used in the new compressive sensing method) is shown in Figure 5.3. Based on Figure 5.3, we use 15 iterations as a reasonable number after

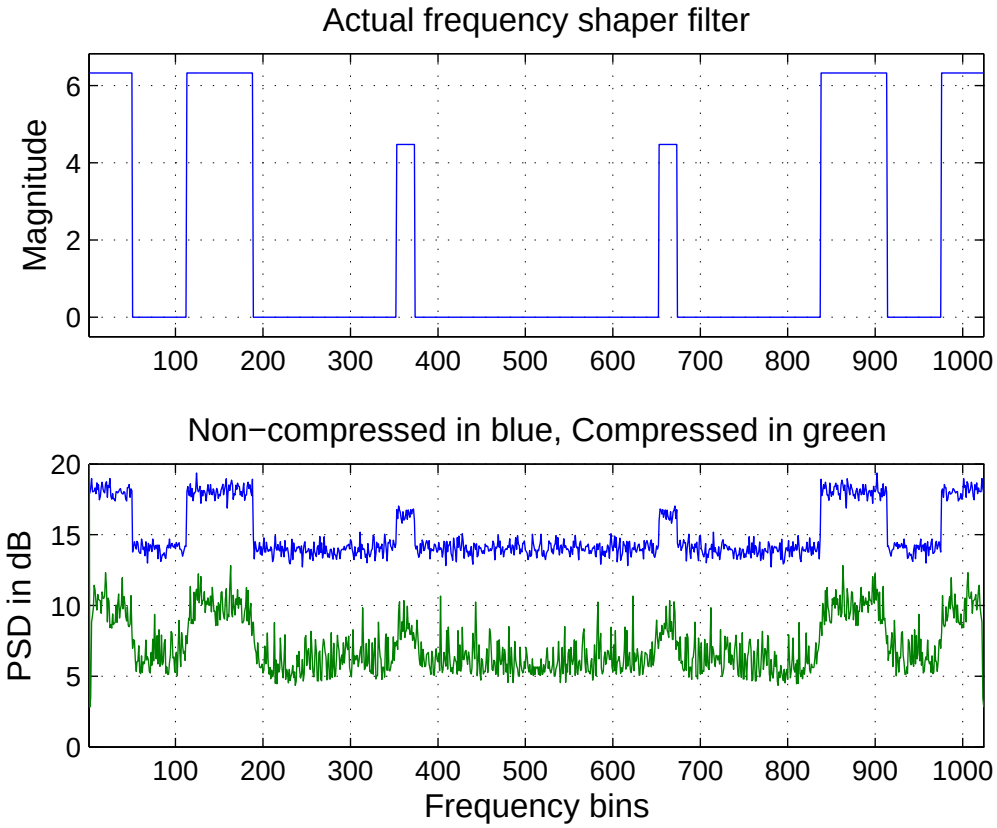

Figure 5.2: The PSD obtained by both compressive and non-compressive sensing methods.

which the EM algorithm can be considered to have converged.

For the case considered in Figure 5.2, the edge detection rate versus SNR curves of compressive sensing technique and non-compressive sensing technique with 100 known segments and 13 known segments (corresponding to 13% of compression ratio) along with the periodogram-based PSD estimation technique, are shown in Figure 5.4. In periodogram-based PSD estimation technique (whose detection rate is shown in the bottom curve of Figure 5.4), only the first segment is involved in the PSD estimation (one known segment). It can be seen that the detection rate of the com-

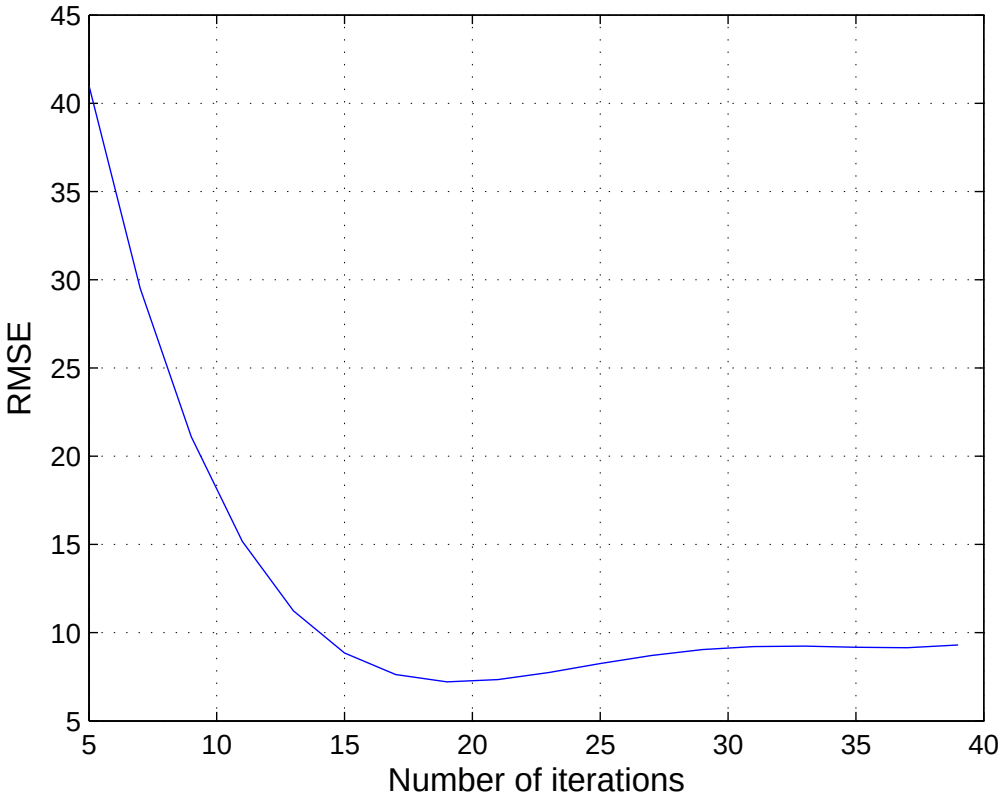

Figure 5.3: The root mean square error of the edge frequency bins versus the number of iterations of the EM algorithm of the new compressive sensing method.

pressive sensing method with 13% of compression ratio, is comparable to that of the non-compressive method and it is better than both the periodogram-based spectrum sensing method and non-compressive sensing method with 13 known segments especially in low SNR scenarios in which any improvement is favorable. We will see in the upcoming simulation results that the more common known points of N_1 will result in better estimation of covariance and thus even better improvement is achieved by compressive sensing technique. In general, any of the above-mentioned designs work efficiently in high SNR scenarios.

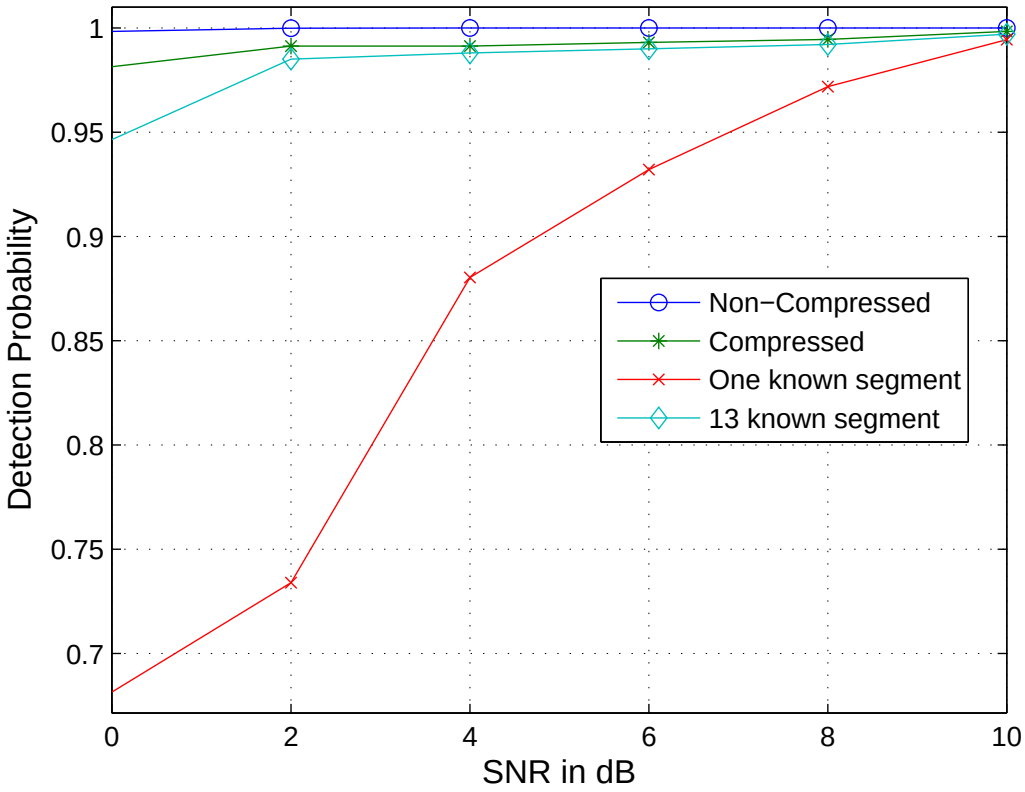

Figure 5.4: Edge detection rate versus SNR curves of both compressive and non-compressive sensing techniques (100 and 13 known segments) along with the one with only first segment involved in the PSD estimation.

We now consider a PSD shaper filter as shown in Figure 5.5. The edge detection rate versus SNR curves of both compressive and non-compressive sensing techniques along with the periodogram-based PSD estimation technique are shown in Figure 5.6. The signal to noise ratio (SNR) of the strongest subbands in these simulations is $SNR = 10$ dB and the other subband is 3 dB weaker. The simulation results are derived from 100 non-overlapping frames of 1024 samples each using Welch's method. For the compressive sensing method, the whole first segment along with the first

128 points of the other segments are available. The compression ratio is 13% for $M_1 = M = 100$ segments and $N_1 = 128$. The remaining unknown data is estimated using the EM algorithm for 15 iterations. Again, it can be seen that the detection rate of the compressive sensing method is comparable to that of the non-compressive method and it is much better than the periodogram-based spectrum sensing method making it a viable alternative.

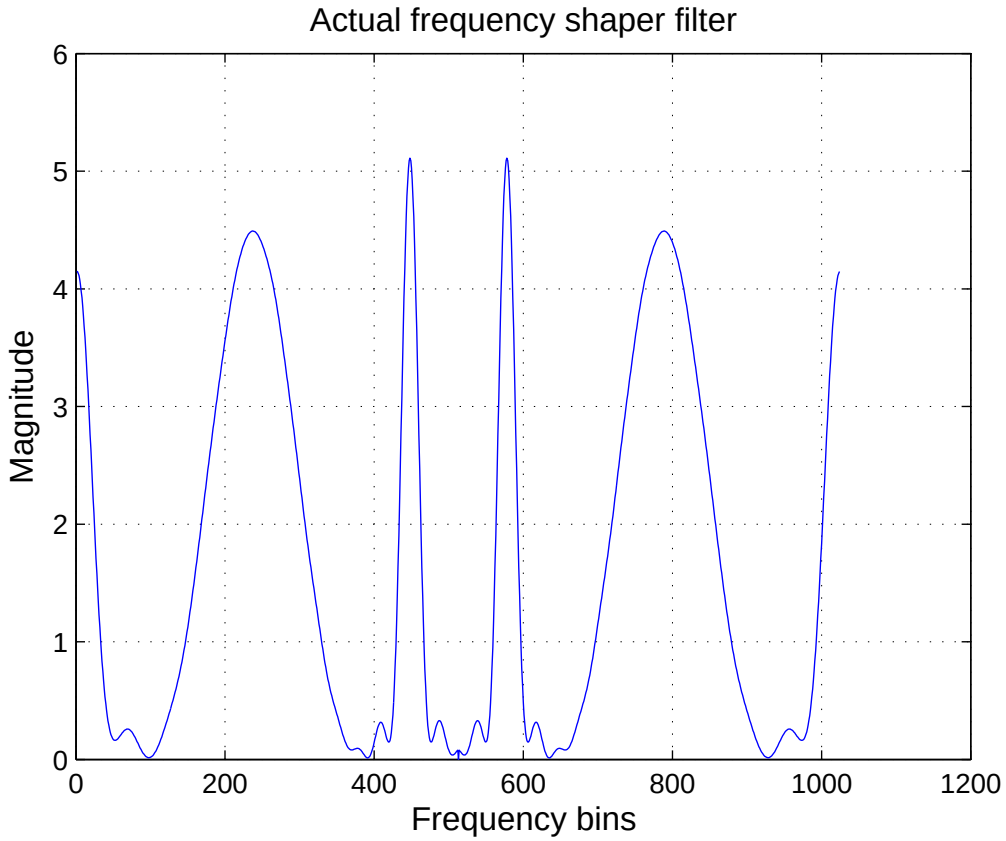

Figure 5.5: A Sinc squared frequency shaper filter.

In order to examine the effects of roll-off factor of the PSD shaper filter on the detection probability, raised-cosine filter is used as the PSD shaper filter. For a low-

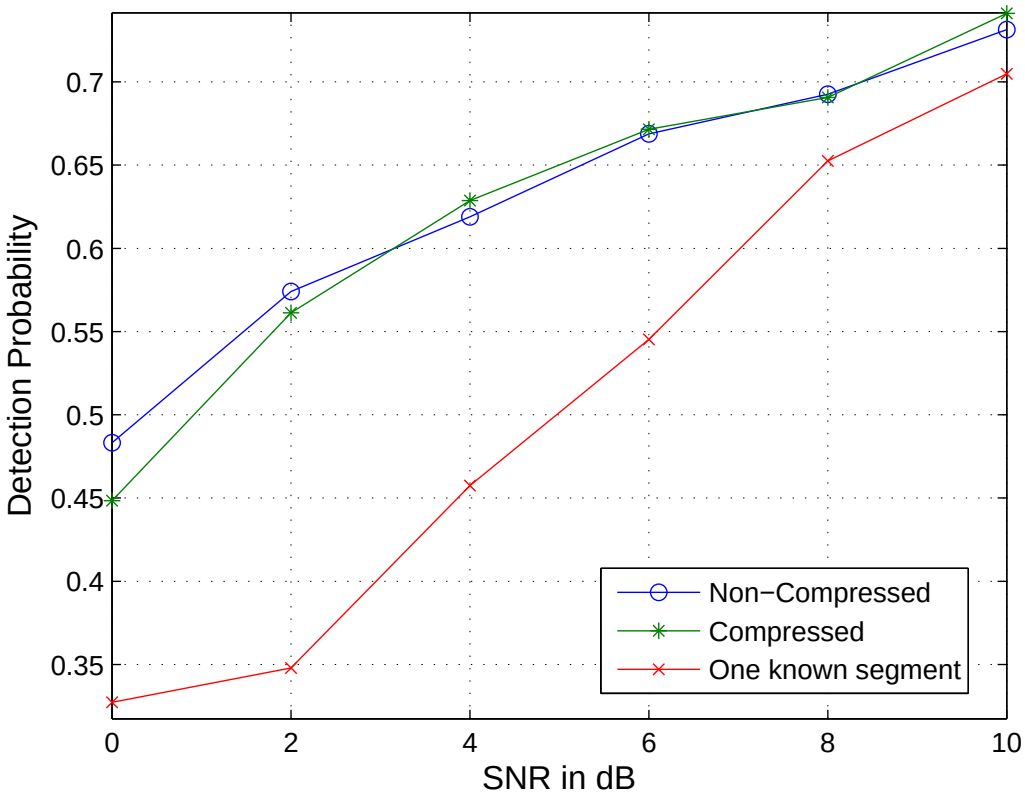

Figure 5.6: Edge detection rate versus SNR curves of both compressive and non-compressive sensing techniques along with the periodogram-based PSD estimation for a PSD with a Sinc square shape.

pass raised-cosine filter given by

$$H(k) = \begin{cases} 1 & k \leq (1-\beta)k_0 \\ \cos^2\left(\frac{\pi}{4\beta k_0}(k-(1-\beta)k_0)\right) & (1-\beta)k_0 < k \leq (1+\beta)k_0 \\ 0 & \text{otherwise} \end{cases} \tag{5.28}$$

in which k represents frequency bin, k_0 represents the cut-off frequency bin of the filter, and β is the roll-off factor ($0 \leq \beta \leq 1$). The edge happens at frequency bin

$(1+\beta)k_0$. For $\beta = 0$, the filter has rectangular-like shape and for $\beta = 1$, it has a cosine function shape.

For a low-pass raised cosine shaper filter with cut-off frequency bin $k_0 = 100$, the edge detection rate versus PSD shaper filter roll-off factor curves of both compressive and non-compressive sensing techniques are shown in Figures 5.7 and 5.8 for $SNR = 0$ dB and $SNR = 5$ dB, respectively. The simulation results are derived from 100 non-overlapping frames of 1024 samples each using Welch's method. For the compressive sensing method, the whole first segment along with the first 128 points of the other segments are available. The compression ratio is 13% for $M_1 = M = 100$ segments and $N_1 = 128$. The remaining unknown data is estimated using the EM algorithm for 15 iterations. Again, it can be seen that the detection rate of the compressive sensing method is comparable to that of the non-compressive method. The detection rate decreases by an increase in the roll-off factor of the PSD shaper filter.

To understand the effects of different structures on the performance, the detection rate of the following scenarios are compared.

1. Case 1: $M_1 = 100$ and $N_1 = 128$; i.e., starting from the first segment, one segment is known in each set of $M_1 = 100$ segments and the first $N_1 = 128$ points of the other segments are known. Its detection is shown in Figure 5.4. $C_r = 13\%$.

2. Case 2: $M_1 = 5$ and $N_1 = 128$. $C_r = 30\%$.

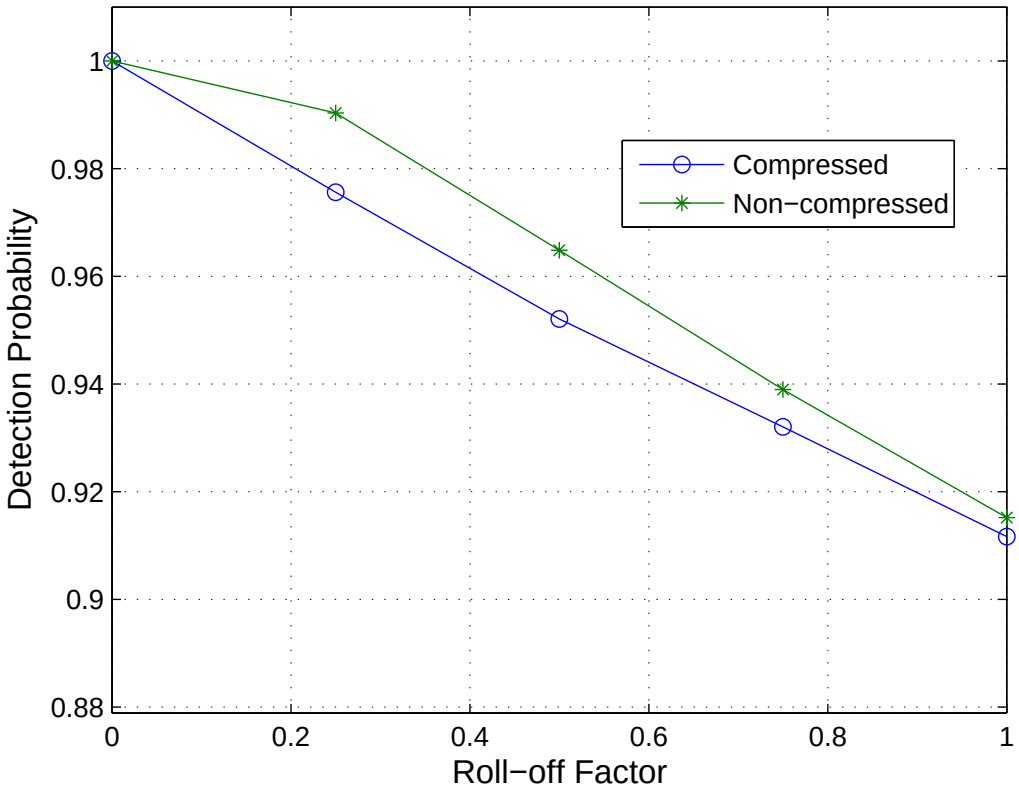

Figure 5.7: Edge detection rate versus PSD shaper filter roll-off factor curves of both compressive and non-compressive sensing techniques.$SNR = 0$ dB.

3. Case 3: $M_1 = 100$ and $N_1 = 256$. $C_r = 26\%$.

The signal whose frequency shaper filter is shown at the top subplot of Figure 5.2 is used for the simulations. The simulation results are derived from 100 non-overlapping frames of 1024 samples each using Welch's method. The edge detection rate versus SNR curves of the proposed compressive sensing algorithm for all compressive sensing cases and the one for non-compressive sensing are shown in Figure 5.9.

For above-mentioned cases, it can be seen in Figure 5.9 that the detection rate increases by both increasing the number of known segments M_1 (case 2) and the

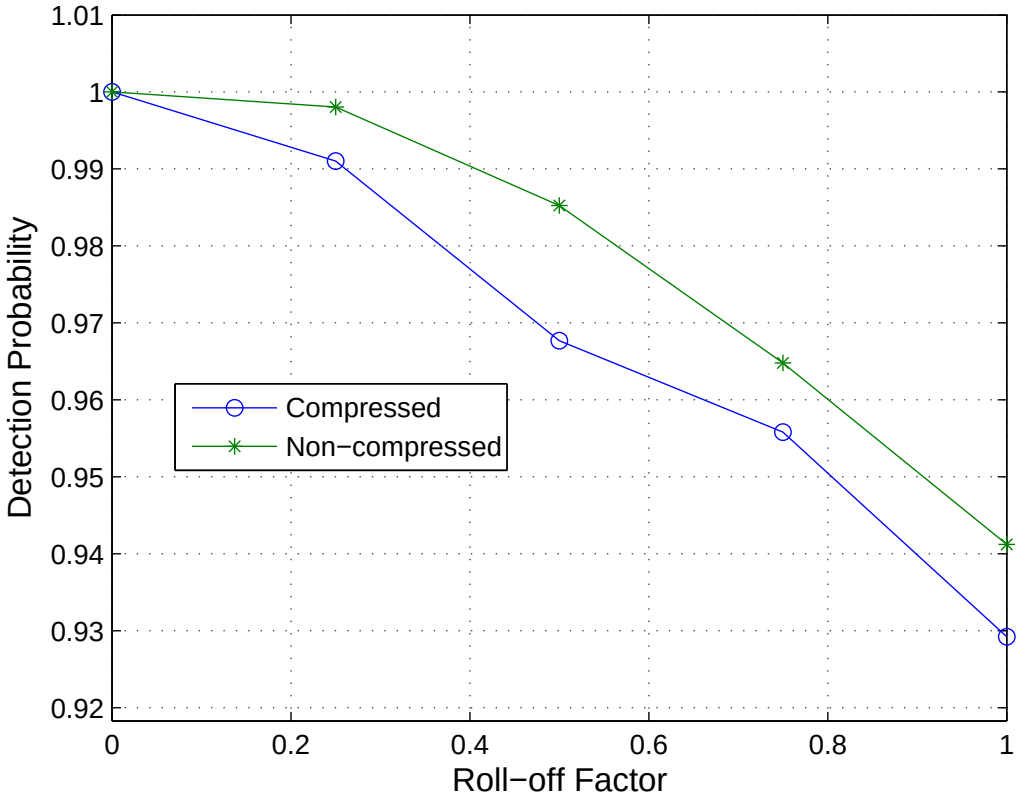

Figure 5.8: Edge detection rate versus PSD shaper filter roll-off factor curves of both compressive and non-compressive sensing techniques.$SNR = 5$ dB.

number of first known points in each segment N_1 (case 3). However, increasing N_1 results in higher detection rate compared to increasing M_1 under the conditions of the above-mentioned cases because a larger N_1 results in more accurate estimation of the covariance of the consecutive segments and thus results in a more accurate estimation of the missing points.

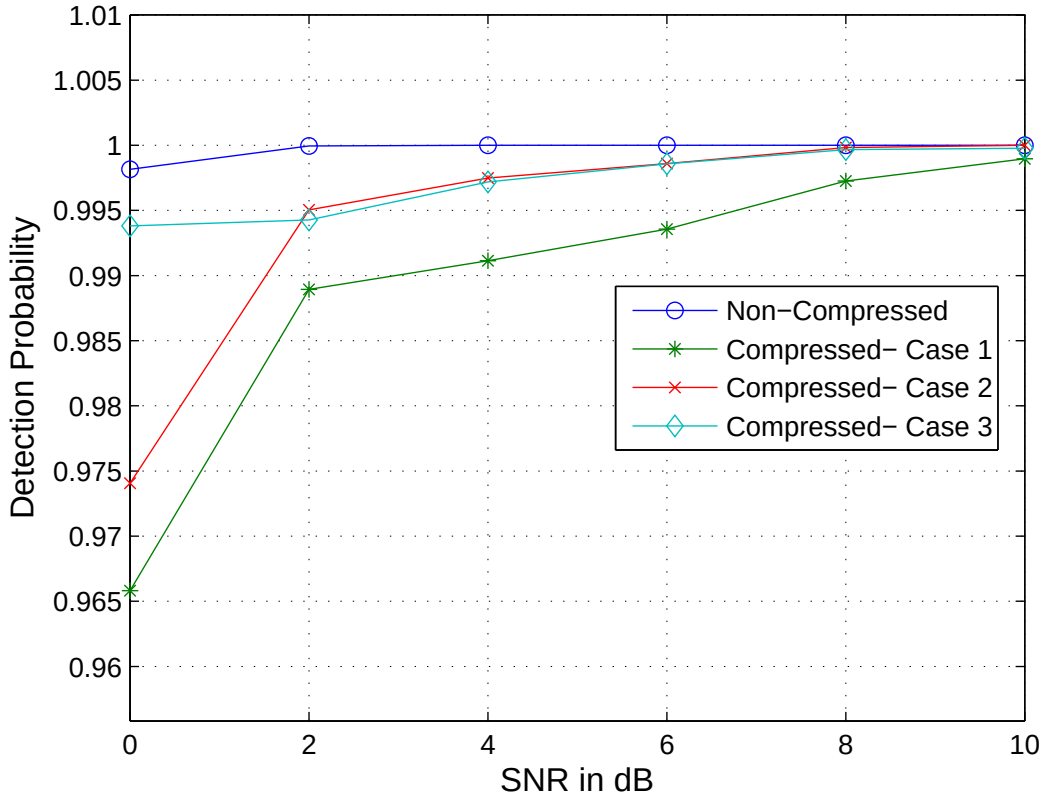

Figure 5.9: Edge detection rate versus SNR curves of compressive sensing algorithm for three compressive sensing cases and the one for non-compressive sensing method.

5.6 Conclusion

In this chapter, we apply a sub-Nyquist non-uniform sampler for spectrum sensing for use in CR. It is shown by simulations and analysis that the proposed sub-Nyquist rate non-uniform sampler is accurate enough to detect the edges of PSD and consumes much less power than the non-compressive sensing method. The proposed sampler samples only some portions of the received signal and switches off the A/D converter based on a predetermined pattern to reduce power consumption. Since the received

signal samples in time domain are correlated, we estimate the missing samples using the expectation-maximization (EM) technique. The analysis of applying EM technique to spectrum sensing shows that the locations of PSD edges are maintained after estimating the missing points of the received signal using EM algorithm. In an example, it is shown that the combined sub-Nyquist sampling/ EM algorithm consumes much less power than Nyquist-based A/D converter thus making the proposed algorithm a viable low-power solution for spectrum sensing. It is shown that although the estimated PSD using the proposed compressive sensing method results in lower values than the non-compressive sensing one, the edges of the PSD are maintained. Since in CR, it is the location of the PSD edges that is important rather than the exact detailed PSD, the proposed compressive sensing method can be used as a low-power solution for A/D conversion in wideband CR. An example shows a reduction of 4.72 mW (76%) for a 100 MSamples/Sec. A/D converter at the expense of 2-3% degradation in detection rate under certain conditions.

Chapter 6

A Novel Multi-Resolution Based PSD Estimation Method Based on Expectation-Maximization Algorithm

6.1 Introduction

As previously mentioned, in Welch's method, the received signal samples are segmented into a few segments. The estimated PSD is achieved by linearly averaging the periodograms of all segments. More averaging leads to lower estimation error variance of the PSD [25]. On the other hand, longer segments lead to a better fre-

quency resolution. Therefore for the same number of received signal samples, there is a trade-off between estimation error variance and resolution.

PSD estimation has very broad applications. For instance, spectrum sensing in cognitive radio (CR) requires an accurate determination of the PSD of the received sequence [5, 46].

In this chapter, we propose a method based on expectation-maximization (EM) [42, 43, 44] algorithm that allows both a better resolution and a lower estimation error variance for the same observation (sensing) time. The idea is based on multi-resolution processing. Assuming that the number of received signal samples is given, first a PSD is obtained using fewer segments with more points per segment. This leads to a PSD with higher resolution (more points in each segment) and thus higher estimation error variance (due to fewer number of segments involved in averaging process). Using the same received signal samples, another PSD is estimated with more segments and fewer points per segment. This PSD has lower estimation error variance (because of more segments) but lower frequency resolution (due to fewer samples in each segment). The expectation-maximization (EM) technique is used to estimate the missing frequency bins of the lower resolution PSD using the PSD with higher resolution. It is shown by simulation that the proposed method improves both the resolution and estimation error variance. Simulation results show better estimation error variance compared to the one obtained by Welch's method. Moreover, the simulations are derived for spectrum sensing application showing the ability of the proposed method to improve

edge detection.

6.1.1 Welch's-based Spectrum Sensing

As previously mentioned, in Welch's method, the received signal samples are segmented into M segments of length N. We will reproduce here the introductory discussion in Chapter 5 for completeness. The estimated PSD ($\mathbf{S}$) is achieved by linearly averaging the periodograms of all segments as

$$\mathbf{S} = \frac{1}{M} \sum_{m} \mathbf{S_m}, \tag{6.1}$$

where $\mathbf{S_m}$ is the m^{th} segment's periodogram. The periodogram of each segment is given by

$$\mathbf{S_m} = \frac{|\mathbf{X_m}|^2}{N}, \tag{6.2}$$

where $\mathbf{X_m}$ is the DFT sequence of the m^{th} segment defined as

$$\mathbf{X_m} = [X_{m1}, X_{m2}, \cdots, X_{mN}] \tag{6.3}$$

and we have

$$|\mathbf{X_m}|^2 = \left[|X_{m1}|^2, |X_{m2}|^2, \cdots, |X_{mN}|^2\right]. \tag{6.4}$$

The estimation error variance of Welch's method is inversely proportional to the

number of segments (M) involved in the averaging process [25]:

$$\sigma^2_{\mathbf{S}} \simeq \frac{\sigma^2_{\mathbf{S_m}}}{M}, \tag{6.5}$$

in which $\sigma^2_{\mathbf{S}}$ represents the estimation error variance of Welch's method and $\sigma^2_{\mathbf{S_m}}$ is the variance of the m^{th} segment's periodogram.

Once the PSD estimation is completed, the spectrum edges are detected. Different methods of edge detection for wideband spectrum sensing are developed in [39]. A modified version of window-averaging based edge detection technique explained in section 4.2.1 has been applied in this chapter.

6.1.2 EM Algorithm Procedure

The EM algorithm procedure is explained in subsection 5.2.2.

6.2 Multi-resolution based PSD Estimation

In the process of PSD estimation, two scenarios of PSD estimation with various resolutions are considered as follows ($M_2 > M_1$):

1. In the first scenario, M_1 segments of N_1 points of the received signal samples are used to obtain a PSD with N_1 frequency bins.

2. Using the same set of received signal samples, in the second scenario, M_2 seg-

ments of N_2 points of the received signal samples are considered to obtain a PSD with N_2 frequency bins. We have:

$$M_1 \times N_1 = M_2 \times N_2 \tag{6.6}$$

It is assumed that $N_1 = R \times N_2$ where R represents the multi-resolution ratio between two scenarios and is considered to be an integer of a power of two $R = 2^n, n \geq 1$. Therefore, in the first scenario, a PSD with higher resolution and higher variance is obtained as averaging is made over fewer segments, whereas in the second scenario, a PSD with lower resolution and lower variance is achieved.

The PSD obtained in scenario 2 is more accurate than the PSD achieved by scenario 1. In other words, the PSD obtained in the first scenario equals the PSD calculated in the second scenario plus the estimation noise due to less averaging in the first scenario. We have

$$\mathbf{S_1} = \mathbf{S_2} + \mathbf{G}, \tag{6.7}$$

in which $\mathbf{G}$ is estimation noise and thus, assumed to have a Gaussian distribution. For simplicity, the joint probability density function of $\mathbf{S_1}$ and $\mathbf{S_2}$ is assumed to exhibit a bi-variate Gaussian distribution. $\mathbf{S_1}$ has N_1 given frequency bins while $\mathbf{S_2}$ has N_2 given frequency bins ($N_1 > N_2$). The remaining points of $\mathbf{S_2}$ ($N_1 - N_2$ points) can be obtained by applying EM algorithm on the two PSD vectors assuming that they have a joint probability density function of bi-variate Gaussian distribution.

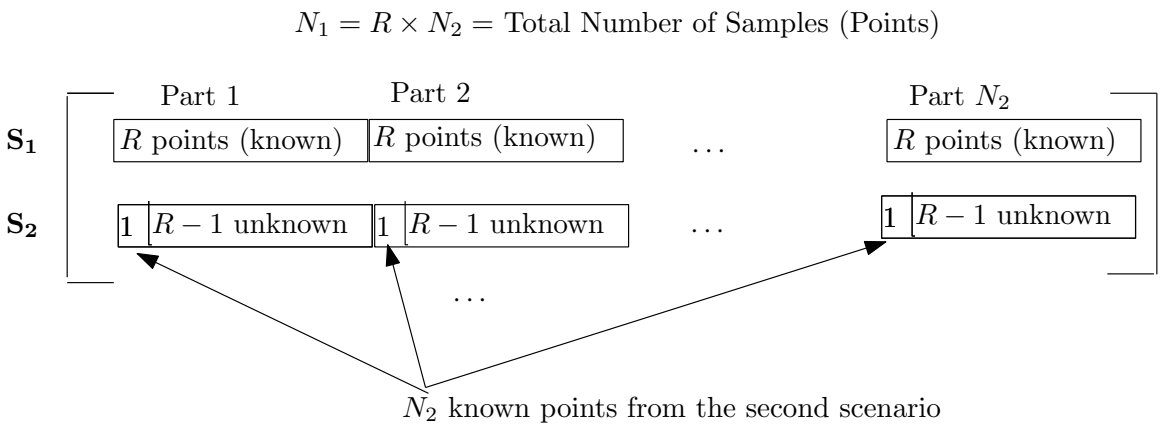

Figure 6.1: Two scenarios with different resolutions to for PSD estimation.

Figure 6.1 shows the above-mentioned scenarios for PSD estimation with various resolutions and estimation error variances. In the first scenario, $\mathbf{S_1}$ has N_2 parts of R known points each (a total of N_1 points). In the second scenario ($\mathbf{S_2}$), each part has 1 known point and $R-1$ unknown points. $\mathbf{S_1}$ has more known points with higher estimation error variance while $\mathbf{S_2}$ has fewer known frequency bins (shown by "1" in each part of R points) with lower estimation error variance. The goal of the proposed algorithm is to estimate the remaining unknown points of $\mathbf{S_2}$ using their associated known frequency bins in $\mathbf{S_1}$ with lower estimation error variance as if all obtained frequency bins are averaged over M_2 segments ($M_2 > M_1$).

The proposed algorithm works as follows:

1. Each part of the estimated PSD along with the following frequency point from its next part (a total of $R+1$ points) are considered.

2. Each above-mentioned $R+1$ points from the first scenario are assumed to construct a bi-variate Gaussian distribution with its corresponding $R+1$ points

from the second scenario.

3. By applying the EM algorithm, the remaining $R-1$ points of each part is estimated using the corresponding known points in both $\mathbf{S_1}$ and $\mathbf{S_2}$.

6.2.1 EM Algorithm for Bi-variate Gaussian Distribution

The joint probability density function of s_1 and s_2 is assumed to exhibit a bi-variate Gaussian distribution. s_1 and s_2 denote elements of vectors $\mathbf{S_1}$ and $\mathbf{S_2}$. We have

$$P(s_1, s_2) = \frac{1}{2\pi\sqrt{\sigma_{s_1}^2\sigma_{s_2}^2 - \sigma_{s_1,s_2}^2}} \times e^{-\frac{\sigma_{s_2}^2(s_1-\mu_1)^2 - 2\sigma_{s_1,s_2}^2(s_1-\mu_1)(s_2-\mu_2) + \sigma_{s_1}^2(s_2-\mu_2)^2}{2(\sigma_{s_1}^2\sigma_{s_2}^2 - \sigma_{s_1,s_2}^2)}}, \quad (6.8)$$

in which $\sigma_{s_1}^2$, $\sigma_{s_2}^2$ and σ_{s_1,s_2}^2 are the variances of s_1, s_2 and the covariance of s_1 and s_2, respectively. μ_1 and μ_2 are the mean values of s_1 and s_2.

It is desired to estimate the unknown points of $\mathbf{S_2}$ using the data given by $\mathbf{S_1}$. The conditional probability density function of $P(s_2|s_1)$ is given by

$$P(s_2|s_1) = \frac{P(s_1, s_2)}{P(s_1)}. \quad (6.9)$$

The maximum likelihood function of s_2 with respect to s_1 is obtained when the first derivative of the logarithm of (6.9) with respect to s_2 equals zero. We have

$$\frac{\partial \ln(P(s_2|s_1))}{\partial s_2} = \frac{\partial \ln(P(s_2, s_1))}{\partial s_2} - \frac{\partial \ln(P(s_1))}{\partial s_2} = 0. \quad (6.10)$$

The second term at the right hand side of the above equation is zero as $P(s_1)$ is not a function of s_2. By substituting (6.8) into (6.10), we have

$$s_2 - \mu_2 = \frac{\sigma^2_{s_1,s_2}}{\sigma^2_{s_1}}(s_1 - \mu_1). \tag{6.11}$$

From the well known properties of Welch's method, we know that $\mu_1 \simeq \mu_2$ [25]. μ_1 substitutes for μ_2 in (6.11). We have:

$$s_2 = \mu_1 + \frac{\sigma^2_{s_1,s_2}}{\sigma^2_{s_1}}(s_1 - \mu_1). \tag{6.12}$$

The above equation is used to estimate the expected values of the unknown points of $\mathbf{S_2}$ in the EM algorithm. The mean, variance and covariance values are obtained locally over the pair parts of $R+1$ points. We have

$$\mu_m = \frac{1}{R+1} \sum_{n=i}^{n=i+R+1} s_m(n), \tag{6.13}$$

in which $n = i$ indicates the beginning frequency bin point of each part. $\sigma^2_{s_1,s_2}$ is the covariance given by

$$\sigma^2_{s_1,s_2} = \frac{1}{R+1}\left(\sum_{n=i}^{n=i+R+1} s_1(n)s_2(n)\right) - \mu_1\mu_2, \tag{6.14}$$

$\sigma^2_{m,m}$ is given by

$$\sigma^2_{m,m} = \frac{1}{R+1}\left(\sum_{n=i}^{n=i+R+1} s^2_m(n)\right) - \mu^2_m. \tag{6.15}$$

Therefore, the EM algorithm is applied over each $R+1$ pair points individually.

The above-mentioned procedure to estimate the mean, variance and covariance values of different parts is the maximization step of EM algorithm. After a few iterations, the unknown elements of each part are estimated.

6.3 Simulation Results

The simulation results are derived for the following cases by applying Welch's PSD estimation method:

1. Case 1 - The HRLV case: Higher Resolution ($N_1 = 1024$), Lower Variance ($M_2 = 80$).

2. Case 2 - The HRHV case: Higher Resolution ($N_1 = 1024$), Higher Variance ($M_1 = 10$).

3. Case 3 - The LRLV case: Lower Resolution ($N_2 = 128$), Lower Variance ($M_2 = 80$).

4. Case 4 - The EM based PSD estimation: A combination of Case 2 and 3.

Case 1 requires 8 times more sensing time than all other cases as it needs more segments to be received.

For a wideband signal with 29% of spectrum occupancy whose frequency shaper filter is shown in Figure 6.2, the PSDs of cases 1, 2 and 3 are obtained and compared to the PSD achieved by the proposed EM-based method (Case 4) in separate Figures 6.3, 6.4 and 6.5, respectively. In this simulation, the EM algorithm uses 10 iterations. The signal to noise ratio (SNR) of the strongest subbands in these simulations is $SNR = 10$ dB. SNR is calculated individually over various subbands and is defined as the ratio of the signal power in each subband to the noise power in that subband. It can be seen from Figure 6.3 that the proposed EM-based algorithm exhibits almost the same PSD shape and fluctuations as the one obtained by higher resolution lower variance (case 1) with only one eighth segments used in the case 1. The comparison of the proposed EM-based method with case 2 (shown in Figure 6.4) shows that the proposed method has less fluctuations and thus lower estimation error variance than the higher resolution higher variance (case 2) with almost the same sensing time. Finally, the proposed method is compared to case 3 (shown in Figure 6.5). It shows that the proposed method introduces higher resolution to the case 3.

Next we consider more closely the estimation error variance of the proposed methods. For the PSD considered in Figure 6.2, the estimation error variance of the dB-scaled PSD versus SNR curves for Cases 1, 2 and 4 are compared and shown in Figure 6.6. It can be seen that the proposed method introduces almost the same estimation error variance compared to Case 1 and much lower estimation error variance compared to Case 2. In [39], it was shown that the estimation error variance of the

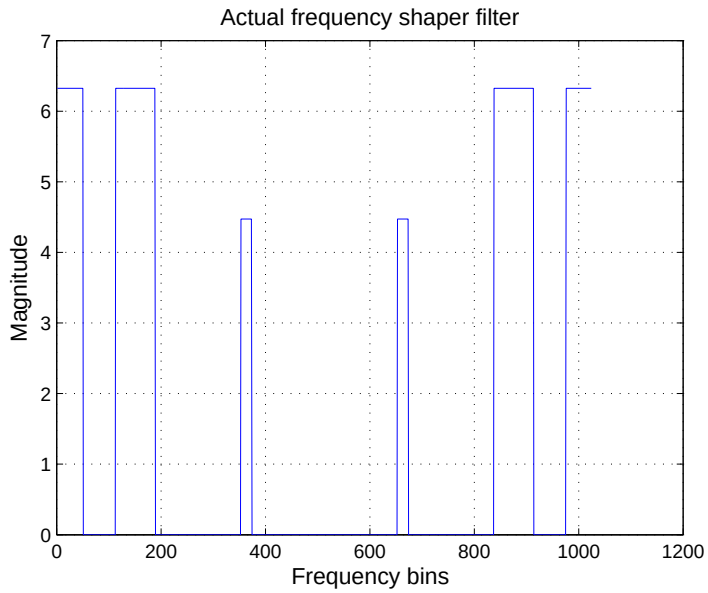

Figure 6.2: The frequency shaper filter used in this simulations.

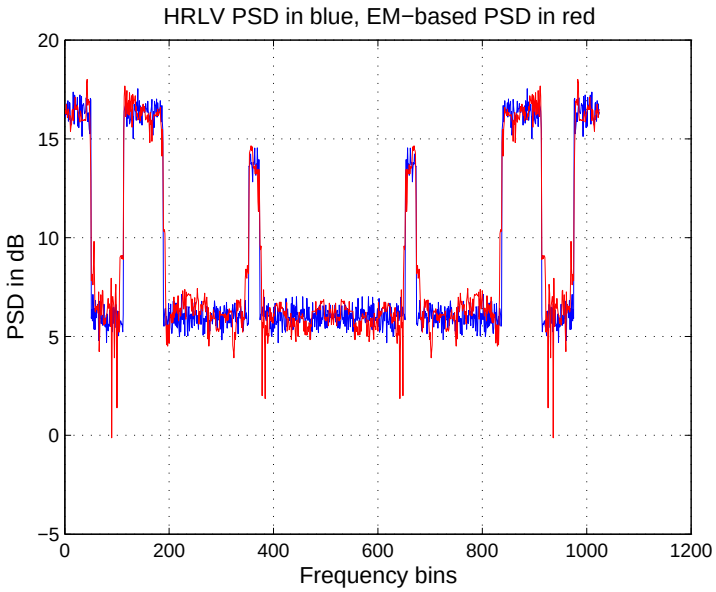

Figure 6.3: The comparison of PSD obtained in Case 1 and EM-based PSD (Case 4).

dB-values of PSD does not change with SNR. Recall that the proposed algorithm requires one eighth sensing time compared to Case 1 and the same sensing time as for

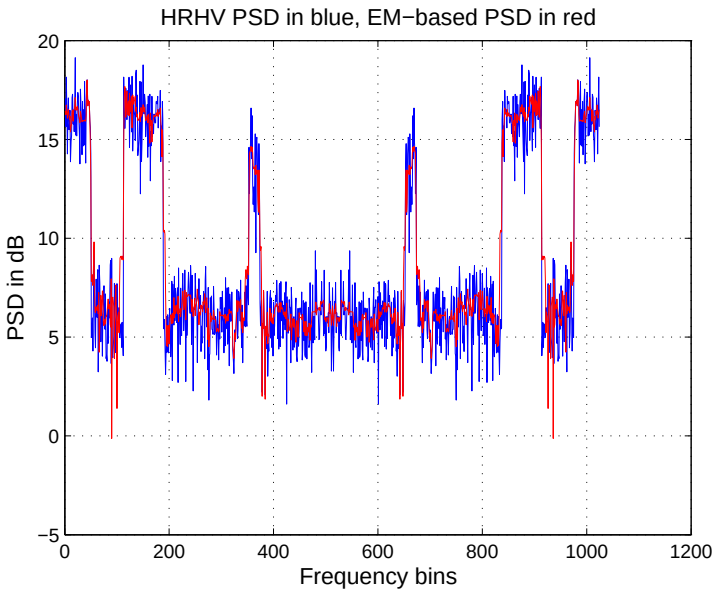

Figure 6.4: The comparison of PSD obtained in Case 2 and EM-based PSD (Case 4).

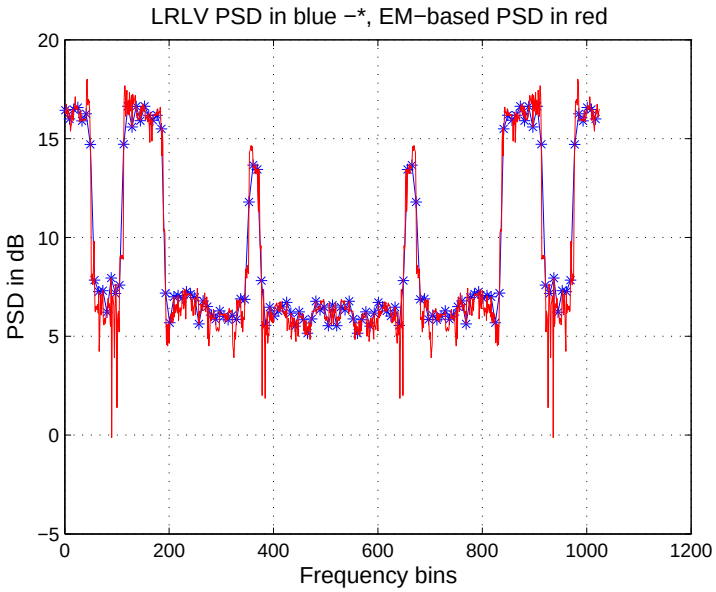

Figure 6.5: The comparison of PSD obtained in Case 3 and EM-based PSD (Case 4).

Case 2. However the proposed algorithm requires more processing time. Therefore, the ability of the proposed algorithm is limited by processing speed of the sensor.

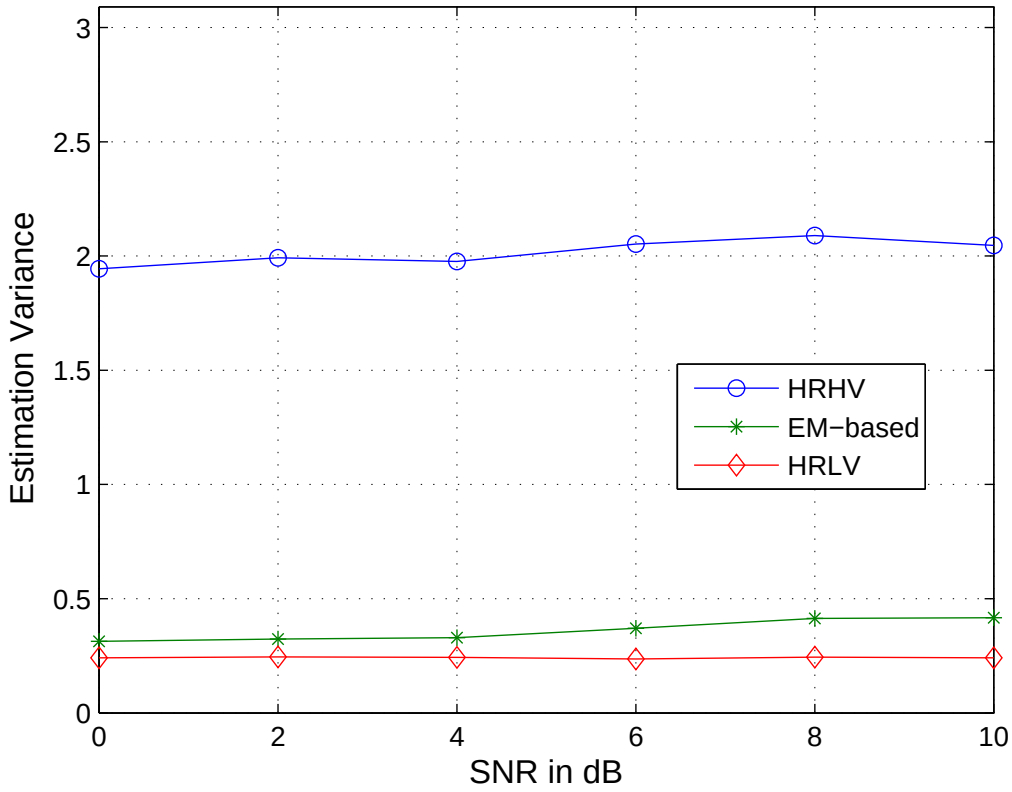

Figure 6.6: Estimation error variance of dB-scaled PSD versus SNR curves of three cases.

Although the proposed method can be used in any PSD estimation application, we applied it to spectrum sensing given its importance. The edges of the PSD are obtained and edge detection rate is used as the performance metric. For the actual PSD shape considered in Figure 6.2, the edge detection rate versus SNR curves of above-mentioned cases are shown in Figure 6.7. It can be seen that the proposed EM-based method performs better that the HRHV and LRLV scenarios. The edge detection rate of HRLV is higher at the expense of 8 times sensing time.

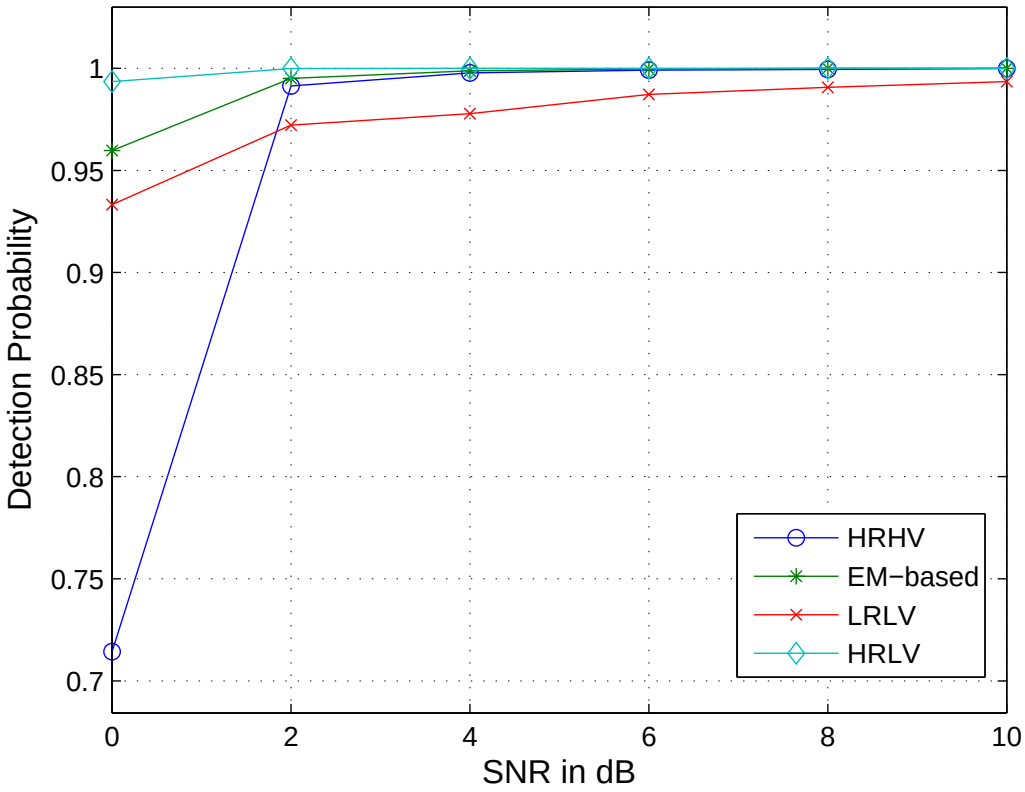

Figure 6.7: Edge detection rate versus SNR curves of all four cases.

To further show the superior performance of the new EM-based PSD estimation method, a PSD with a very narrow band is assumed. The width of the narrow subband is chosen so that it can be detected by a high resolution (Cases 1 and 2) technique and it cannot be detected by the low resolution Case 3. The estimated PSD using parameters of Case 1 is shown in Figure 6.8. The estimated PSD using the low resolution Case 3 along with the PSD obtained by the proposed EM-based method are shown in Figure 6.9. The signal to noise ratio (SNR) of the strongest subbands in these simulations is $SNR = 10$ dB and the narrow subband has $SNR = 7$ dB. In

this simulation, the EM algorithm uses100 iterations. It can be seen from Figure 6.9 that the EM-based method can detect the narrow subband after 100 iterations.

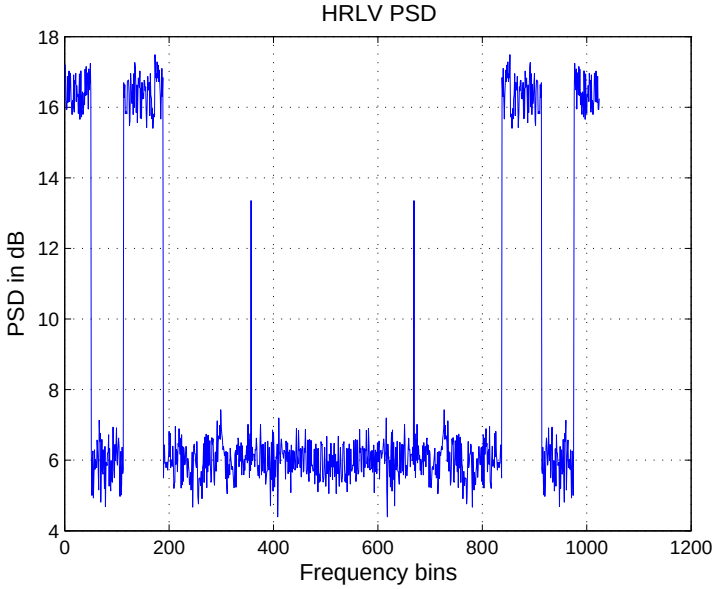

Figure 6.8: PSD with a narrow subband obtained by applying Case 1.

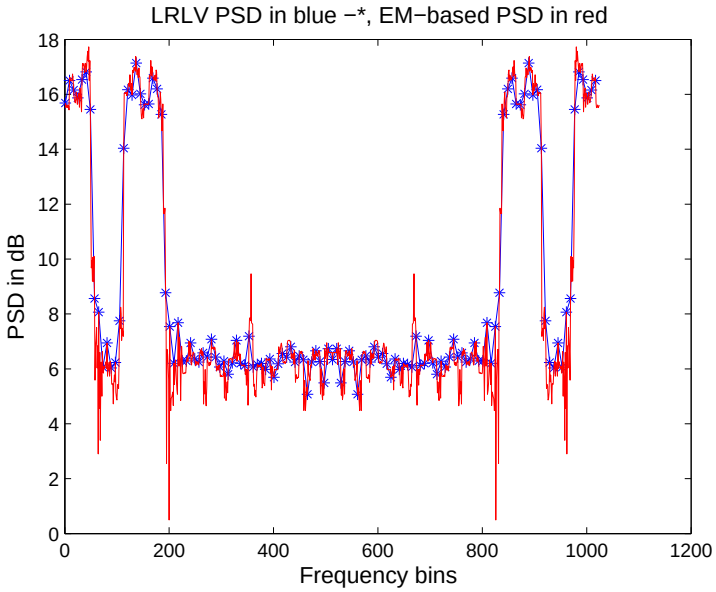

Figure 6.9: The comparison of PSD obtained in Case 3 and EM-based PSD (Case 4) for a PSD with a narrow subband.

6.3.1 Complexity Comparison of HRLV, HRHV, LRLV and EM-based PSD Estimation Methods

Complexity of HRLV, HRHV, LRLV and EM-based PSD estimation methods are compared in Table 6.1. The complexity order of Welch's method is given by $O(N^3)$ [25] and complexity order of EM algorithm is given by $10INM$ in which I is the number of iterations. M is the number of received signal segments and N is the number of samples in each segment. For the given example, it can be seen that the complexity of EM-based PSD estimation is of the same order as of both HRLV and HRHV.

Table 6.1: Complexity Comparison Table of HRLV, HRHV, LRLV and EM-based PSD Estimation Methods

Method	**Complexity order**	**Complexity order of the given example**
HRLV	$O(N_1^3)$	$O(10^9)$
HRHV	$O(N_1^3)$	$O(10^9)$
LRLV	$O(N_2^3)$	$O(10^6)$
EM-based	$O(N_1^3) + 10IN_1M_1 \approx O(N_1^3)$	$O(10^9) + 10^6 \approx O(10^9)$

6.4 Conclusion

In this chapter, we propose a method based on expectation-maximization (EM) algorithm that allows both a better resolution and a lower estimation error variance with the same observation (sensing) time. The idea of this chapter is based on multi-resolution processing. Assuming that the number of received signal samples is given,

first a PSD with higher resolution (more points in each segment) and thus higher estimation error variance (due to fewer number of segments involved in averaging process) is obtained. Using the same received signal samples, another PSD is estimated with lower estimation error variance (because of more segments) but lower frequency resolution (due to fewer samples in each segment). To have both a higher resolution and a lower estimation error variance Using the same number of samples, we applied expectation-maximization (EM) technique to estimate the missing frequency bins of the lower resolution PSD using the PSD with higher resolution. It is shown by simulation that the proposed method improves both the resolution and estimation error variance. Thus the proposed method requires less sensing time than the conventional Welch's method to have a better estimation error variance. The simulations are derived for spectrum sensing application showing the improved performance of the proposed method in improving the edge detection.

Chapter 7

Concluding Remarks

This thesis is concerned with different aspects of wideband spectrum sensing for cognitive radio. Cognitive radio has been proposed to combat the spectrum scarcity problem by utilizing the unused portions of the licensed spectrum. Spectrum is a limited natural resource that is statically assigned to the licensed bodies. Measurements of the licensed spectra show that they are not efficiently utilized. There are at least three major issues in wideband spectrum sensing: PSD estimation, PSD edge detection and power consumption. In this chapter, we briefly review the contributions of this thesis to address these issues and suggest some directions for future research work.

7.1 Summary of Contributions

In this thesis, we first proposed some new methods to detect PSD edges (Chapter 3). We argued that the current proposed edge detection methods are not accurate enough to detect the PSD edges especially when the levels of signal are (very) different in various subbands. It was proposed to employ the dB-scale values of PSD instead of the linear scale values because the use of the dB scale values makes the estimation variance more uniform in bands of different power levels. We verified the superiority of that modification through simulation results and analytical analysis. We also proposed a new edge detection technique based on window-normalization that exhibits better detection rate compared to the conventional methods even after applying the dB-scale modification. Furthermore, another new edge detection method is proposed that smoothes the fluctuations and can detect the noise level of the estimated PSD more accurately. This proposed method utilizes the integer part of window-averaged PSD as its metric to detect presence of an edge. It was shown to have improved detection rates compared to other algorithms. Some of the results from this part of research were presented in [39].

As the second contribution of this research, a new time-to-frequency conversion technique, the simplified DFT, was proposed in Chapter 4. The reduced complexity of the simplified DFT matrix is shown and its performance is compared to that of the traditional DFT-based methods especially in spectrum sensing applications. We studied the performance of the proposed technique through both simulation results

and mathematical analyses. In particular, we showed that SDFT-based spectrum sensing is accurate enough when the spectrum occupancy is low; a reasonable assumption for CR. Furthermore, we evaluated the performance of SDFT techniques via mathematical analysis and derived detection versus false alarm rate curves for the proposed methods in case of a single tone signal. Some of the results from this part of research were presented in [40], [41].

As the third contribution of this thesis, we proposed to apply a sub-Nyquist non-uniform sampler for spectrum sensing to reduce the power consumption (Chapter 5). The idea is based on switching on/off the A/D converter based on a pre-specified pattern. The resulting missing samples are then estimated using EM algorithm. We verified the accuracy of applying EM technique to spectrum sensing through both simulation results and mathematical analysis. The mathematical analysis proves that the locations of PSD edges are maintained using the proposed algorithm. In a typical practical example, it is shown that EM algorithm consumes much less power than A/D converter thus making the proposed algorithm a viable low-power solution for spectrum sensing. We presented some of the results from this part of the work in [44].

As the last contribution of the research, we proposed a PSD estimation method based on EM algorithm that allows both a better resolution and a lower estimation error variance with the same observation (sensing) time (Chapter 6). The idea of this chapter is based on multi-resolution processing. From the same observed samples,

two PSDs are obtained: one with higher resolution (and thus higher estimation error variance), the other with lower resolution (and thus lower estimation error variance). Since these two PSDs are correlated, we proposed to estimate the missing frequency bins of the lower resolution PSD by applying EM algorithm on both PSDs. We verified through simulation that the resulting PSD will then have both lower estimation error variance and higher resolution. The proposed method requires less sensing time (fewer observed samples) than the conventional Welch's method to have a lower estimation error variance. Although the algorithm is proposed for any PSD estimation application, we demonstrate its performance in spectrum sensing. The results of this work are part of a patent application and thus cannot be published beforehand.

7.2 Future Work

In Chapter 3, some new methods to detect PSD edges and determine noise level, are presented. The noise level is assumed to be the most frequent level of PSD in a wideband of interest. Due to more accurate noise level determination in the proposed edge detection methods, the noise level uncertainty is decreased. A decrease in the level of noise uncertainty results in lower SNR wall. One possible research direction is to investigate the SNR wall of the proposed edge detection methods to determine the lowest SNR level that can be detected using proposed edge detection methods. Since the primary signals exhibit negative SNRs at the CR receiver in many cases, the knowledge of SNR walls of the proposed edge detection techniques is helpful.

In Chapter 4, a new simplified DFT time-to-frequency conversion is introduced to reduce the complexity of the DFT technique. It is proposed to be used for spectrum sensing purposes. It is shown that this approximation works well for spectrum sensing purposes due to the low occupancy of the CR spectrum. A possible direction for future work is to investigate the possibility of applying this simplified technique for other applications such as image processing, speech processing and so on. The merits and demerits of applying SDFT to those applications are to be investigated. Moreover, the IDFT is used in the OFDM modulator and DFT is used in the OFDM demodulator. As OFDM technique is chosen for many wireless applications such as fourth generation wireless communications, reducing its complexity might be desirable. One possible future research is to investigate the advantages and disadvantages of applying SDFT in OFDM technique.

In Chapter 5, a sub-Nyquist non-uniform sampler for spectrum sensing is introduced to reduce the A/D power consumption. Since power consumption is subject to the hardware design, a possible future research work is to investigate the proposed algorithm's power consumption for various hardware designs.

In Chapter 6, a novel multi-resolution PSD estimation technique based on EM algorithm is introduced. The proposed algorithm is applied for spectrum sensing purposes. It would be useful to investigate the performance of the proposed technique in other applications in which PSD estimation is required such as audio signal processing, (medical) image processing and so on.

PSD estimation is one important step in many applications including spectrum sensing. In Welch's method, the PSD is estimated through linearly averaging the periodograms of consecutive segments of the received signal samples. One possible direction of future research is to investigate more accurate PSD estimation methods even if more complex, as higher accuracy can decrease the SNR wall.

For spectrum sensing purposes, we need to detect the presence of a primary signal. Whenever a primary signal is present in a frequency bin, the periodogram vector element in that frequency bin follows the non-central chi-square distribution, and it follows the central chi-square distribution when primary signal is not present [46]. Therefore, one possible future direction of the research is to apply a log likelihood ratio hypothesis test to find how far the periodogram distribution is from a central chi-square distribution to possibly detect the presence of a primary signal. We hope that the performance of this method would be better than conventional methods and thus it might be suitable to detect the primary signal presence in lower SNRs.

Finally, in this thesis we worked on the non-cooperative spectrum sensing problem. It is also desirable to consider cases where the cognitive users cooperate to detect spectrum holes.

Bibliography

[1] Federal Communications Commission, "Spectrum policy task force report, FCC 02-155," Nov. 2002.

[2] D. B. Cabric and R. W. Brodersen, *Cognitive Radios: System Design Perspective*. PhD thesis, EECS Department, University of California, Berkeley, Dec 2007.

[3] M. McHenry, "NSF Spectrum Occupancy Measurements Project Summary," Aug. 2005.

[4] J. Mitola, *Cognitive Radio: An Integrated Agent Architecture for Software Defined Radio*. PhD thesis, KTHRoyal Institute of Technology, Dec 2000.

[5] S. Haykin, "Cognitive radio: brain-empowered wireless communications," *Selected Areas in Communications, IEEE Journal on*, vol. 23, pp. 201 – 220, Feb. 2005.

[6] N. Devroye, P. Mitran, and V. Tarokh, "Cognitive decomposition of wireless networks," in *In Proceedings of CROWNCOM*, 2006.

[7] I. F. Akyildiz, W.-Y. Lee, M. C. Vuran, and S. Mohanty, "Next generation/dynamic spectrum access/cognitive radio wireless networks: A survey," *Computer Networks*, vol. 50, no. 13, pp. 2127 – 2159, 2006.

[8] C. Cordeiro, K. Challapali, D. Birru, and N. Sai Shankar, "Ieee 802.22: the first worldwide wireless standard based on cognitive radios," pp. 328 –337, nov. 2005.

[9] C. R. Stevenson, G. Chouinard, Z. Lei, W. Hu, S. J. Shellhammer, and W. Caldwell, "Ieee 802.22: the first cognitive radio wireless regional area network standard," *Comm. Mag.*, vol. 47, no. 1, pp. 130–138, 2009.

[10] S. Mishra, R. Brodersen, S. Brink, and R. Mahadevappa, "Detect and avoid: an ultra-wideband/wimax coexistence mechanism [topics in radio communications]," *Communications Magazine, IEEE*, vol. 45, pp. 68 –75, jun. 2007.

[11] R. Tandra, A. Sahai, and S. Mishra, "What is a spectrum hole and what does it take to recognize one?," *Proceedings of the IEEE*, vol. 97, pp. 824 –848, may. 2009.

[12] I. Akyildiz, W.-Y. Lee, M. Vuran, and S. Mohanty, "A survey on spectrum management in cognitive radio networks," *Communications Magazine, IEEE*, vol. 46, pp. 40 –48, apr. 2008.

[13] A. Ghasemi and E. Sousa, "Spectrum sensing in cognitive radio networks: requirements, challenges and design trade-offs," *Communications Magazine, IEEE*, vol. 46, pp. 32 –39, apr. 2008.

[14] D. Cabric, S. Mishra, and R. Brodersen, "Implementation issues in spectrum sensing for cognitive radios," vol. 1, pp. 772 – 776 Vol.1, nov. 2004.

[15] H. Urkowitz, "Energy detection of unknown deterministic signals," *Proceedings of the IEEE*, vol. 55, pp. 523 – 531, apr. 1967.

[16] S. Enserink and D. Cochran, "A cyclostationary feature detector," vol. 2, pp. 806 –810 vol.2, oct. 1994.

[17] S. M. Kay, *Fundamentals of statistical signal processing: Detection theory*. Upper Saddle River, NJ, USA: Prentice-Hall, Inc., 1998.

[18] Y. Hur, J. Park, W. Woo, K. Lim, C.-H. Lee, H. Kim, and J. Laskar, "A wideband analog multi-resolution spectrum sensing (mrss) technique for cognitive radio (cr) systems," p. 4 pp., 2006.

[19] Z. Quan, S. Cui, A. Sayed, and H. Poor, "Wideband spectrum sensing in cognitive radio networks," pp. 901 –906, may. 2008.

[20] P. Paysarvi Hoseini and N. Beaulieu, "An optimal algorithm for wideband spectrum sensing in cognitive radio systems," pp. 1 –6, may. 2010.

[21] Z. Tian and G. B. Giannakis, "A wavelet approach to wideband spectrum sensing for cognitive radios," pp. 1 –5, jun. 2006.

[22] A. Taherpour, S. Gazor, and M. Nasiri-Kenari, "Wideband spectrum sensing in unknown white gaussian noise," *Communications, IET*, vol. 2, pp. 763 –771, jul. 2008.

[23] T.-H. Yu, S. Rodriguez-Parera, D. Markovic and, C, and D. Cabric and, "Cognitive radio wideband spectrum sensing using multitap windowing and power detection with threshold adaptation," pp. 1 –6, may. 2010.

[24] P. Welch, "The use of fast fourier transform for the estimation of power spectra: A method based on time averaging over short, modified periodograms," *Audio and Electroacoustics, IEEE Transactions on*, vol. 15, pp. 70 – 73, jun. 1967.

[25] A. V. Oppenheim and R. W. Schafer, *Discrete-Time Signal Processing*. Upper Saddle River, NJ, USA: Prentice Hall Press, 2009.

[26] C. D. Chinard G. and G. M., "Sensing thresholds in ieee 802.22-06/005/r3," May 2006.

[27] R. Tandra and A. Sahai, "Snr walls for signal detection," *Selected Topics in Signal Processing, IEEE Journal of*, vol. 2, pp. 4 –17, feb. 2008.

[28] S. M. Kay and S. L. Marple, "Spectral analysis- a modern perspective," vol. 69, pp. 1380–1419, Aug. 1981.

[29] S. Haykin, "The multitaper method for accurate spectrum sensing in cognitive radio environments," pp. 436 –439, nov. 2007.

[30] B. Farhang-Boroujeny, "Prolate filters for nonadaptive multitaper spectral estimators with high spectral dynamic range," *Signal Processing Letters, IEEE*, vol. 15, pp. 457 –460, 2008.

[31] V. Blaschke, T. Renk, and F. Jondral, "A cognitive radio receiver supporting wide-band sensing," pp. 499 –503, may. 2008.

[32] R. Plassche, *CMOS Integrated Analog-to-digital and Digital-to-analog Converters, 2nd Ed.* Boston: Kluwer Academic Publishers, 2003.

[33] B. Brannon, *Software Defined Radio - Enabling Technology*. London: John Wiley and Sons, 2002.

[34] E. Candes and M. Wakin, "An introduction to compressive sampling," *Signal Processing Magazine, IEEE*, vol. 25, pp. 21 –30, mar. 2008.

[35] D. Donoho, "Compressed sensing," *Information Theory, IEEE Transactions on*, vol. 52, pp. 1289 –1306, apr. 2006.

[36] Z. Tian and G. Giannakis, "Compressed sensing for wideband cognitive radios," vol. 4, pp. IV–1357 –IV–1360, apr. 2007.

[37] Z. Quan, S. Cui, and A. Sayed, "Optimal linear cooperation for spectrum sensing in cognitive radio networks," *Selected Topics in Signal Processing, IEEE Journal of*, vol. 2, pp. 28 –40, feb. 2008.

[38] J. Unnikrishnan and V. Veeravalli, "Cooperative spectrum sensing and detection for cognitive radio," pp. 2972 –2976, nov. 2007.

[39] Y. Miar and C. D'Amours, "Novel spectrum edge detection techniques in wideband spectrum sensing of cognitive radio," in 22$^{\text{nd}}$ *Annual IEEE Symposium on Personal Indoor Mobile Radio Communications, PIMRC 2011.*, pp. 456–460, 2011.

[40] Y. Miar, C. D'Amours, A. Yongacoglu, and T. Aboulnasr, "Simplified dft: A novel method for wideband spectrum sensing in cognitive radio," in *New Frontiers in Dynamic Spectrum Access Networks, DySPAN 2011. Fifth IEEE International Symposium on*, May 2011.

[41] Y. Miar, C. D'Amours, and T. Aboulnasr, "Simplified dft: A novel method for wideband spectrum sensing in cognitive radio," in *Submitted to IEEE Transactions on Vehicular Technology*.

[42] T. Moon and W. Stirling, *Mathematical Methods and Algorithms for Signal Processing*. Prentice Hall, 2000.

[43] T. K. G McLachlan, *The EM algorithm and extensions*. Wiley series in probabilities and statistics, 1997.

[44] Y. Miar, C. D'Amours, and T. Aboulnasr,, "A novel compressive sensing technique for wideband cognitive radio to reduce a/d power consumption,," in *Revision submitted to EURASIP Journal on Wireless Communications and Networking, Special issue on Green Radio, March 2012.*

[45] E. Hossain and V. K. Bhargava, *Software Defined Radio: Architectures, Systems and Functions*. New York, USA: Wiley, 2003.

[46] E. Hossain and V. K. Bhargava, *Cognitive Wireless Communication Networks*. Springer, 2007.

[47] P. Pawelczak, S. Pollin, H.-S. So, A. Bahai, R. Prasad, and R. Hekmat, "Quality of service assessment of opportunistic spectrum access: a medium access control approach," *Wireless Communications, IEEE*, vol. 15, no. 5, pp. 20 –29, 2008.

[48] C. Raman, R. Yates, and N. Mandayam, "Scheduling variable rate links via a spectrum server," in *New Frontiers in Dynamic Spectrum Access Networks, 2005. DySPAN 2005. 2005 First IEEE International Symposium on*, pp. 110 –118, 2005.

[49] L. Cao and H. Zheng, "Distributed spectrum allocation via local bargaining," in *Sensor and Ad Hoc Communications and Networks, 2005. IEEE SECON 2005. 2005 Second Annual IEEE Communications Society Conference on*, 2005.

[50] J. Huang, R. Berry, and M. Honig, "Spectrum sharing with distributed interference compensation," in *New Frontiers in Dynamic Spectrum Access Networks, 2005. DySPAN 2005. 2005 First IEEE International Symposium on*, pp. 88 –93, 2005.

[51] A. Ghasemi and E. Sousa, "Collaborative spectrum sensing for opportunistic access in fading environments," in *New Frontiers in Dynamic Spectrum Access Networks, 2005. DySPAN 2005. 2005 First IEEE International Symposium on*, pp. 131 –136, 2005.

[52] Q. Zhao, L. Tong, and A. Swami, "Decentralized cognitive mac for dynamic spectrum access," in *New Frontiers in Dynamic Spectrum Access Networks, 2005. DySPAN 2005. 2005 First IEEE International Symposium on*, pp. 224 –232, 2005.

[53] A. Goldsmith, S. A. Jafar, I. Mari, and S. Srinivasa, "Breaking spectrum gridlock with cognitive radios: An information theoretic perspective," 2008.

[54] R. Menon, R. Buehrer, and J. Reed, "Outage probability based comparison of underlay and overlay spectrum sharing techniques," in *New Frontiers in Dynamic*

Spectrum Access Networks, 2005. DySPAN 2005. 2005 First IEEE International Symposium on, pp. 101 –109, 2005.

[55] K. Gilhousen, I. Jacobs, R. Padovani, A. Viterbi, J. Weaver, L.A., and I. Wheatley, C.E., "On the capacity of a cellular cdma system," *Vehicular Technology, IEEE Transactions on*, vol. 40, pp. 303 –312, May 1991.

[56] Federal Communications Commission, "Fcc first report and order: Revision of part 15 of the commissionss rules regarding ultra-wideband transmission systems," ET Docket No. 98-153, Apr. 2002.

[57] W. Gardner and C. Spooner, "Signal interception: performance advantages of cyclic-feature detectors," *Communications, IEEE Transactions on*, vol. 40, pp. 149 –159, Jan. 1992.

[58] W.-Y. Lee and I. Akyildiz, "Optimal spectrum sensing framework for cognitive radio networks," *Wireless Communications, IEEE Transactions on*, vol. 7, no. 10, pp. 3845 –3857, 2008.

[59] A. Papoulis, *Probability, Random Variables and Stochastic Processes*. McGraw-Hill Europe; 4th edition, 2002.

[60] H. Jokinen, J. Ollila, and O. Aumala, "On windowing effects in estimating averaged periodograms of noisy signals," *Measurement*, vol. 28, no. 3, pp. 197 – 207, 2000.

[61] S. Mallat and W. Hwang, "Singularity detection and processing with wavelets," *Information Theory, IEEE Transactions on*, vol. 38, pp. 617 –643, Mar. 1992.

[62] A. Hossen, "Power spectral density estimation via wavelet decomposition," *Electronics Letters*, vol. 40, no. 17, pp. 1055 – 1056, 2004.

[63] M. Jiang and S. Pfletschinger, "Power spectral density estimation of noisy signal based on wavelet," in *Industrial Electronics, 2007. ISIE 2007. IEEE International Symposium on*, pp. 1612 –1616, 2007.

[64] Y. M. Q. C. P. So, H.C.; Chan, "Comparison of various periodograms for sinusoid detection and frequency estimation," in *Aerospace and Electronic Systems, IEEE Transactions on*, vol. 35, pp. 945–952, 1999.

[65] S. M. Proakis, John G, *Digital Communications*. Boston : McGraw-Hill, 5th ed., 2008.

[66] J. Palicot, "Cognitive radio: An enabling technology for the green radio concept," Jul. 2009.

[67] J. Laska, W. Bradley, T. Rondeau, K. Nolan, and B. Vigoda, "Compressive sensing for dynamic spectrum access networks: Techniques and tradeoffs," in *New Frontiers in Dynamic Spectrum Access Networks (DySPAN), 2011 IEEE Symposium on*, pp. 156 –163, may 2011.

[68] E. Candes, J. Romberg, and T. Tao, "Robust uncertainty principles: exact signal reconstruction from highly incomplete frequency information," *Information Theory, IEEE Transactions on*, vol. 52, pp. 489 – 509, feb. 2006.

[69] Y. Jin, Y.-H. Kim, and B. Rao, "Limits on support recovery of sparse signals via multiple-access communication techniques," *Information Theory, IEEE Transactions on*, vol. 57, pp. 7877 –7892, dec. 2011.

[70] D. Arianandа and G. Leus, "Wideband power spectrum sensing using sub-nyquist sampling," in *Signal Processing Advances in Wireless Communications (SPAWC), 2011 IEEE 12th International Workshop on*, pp. 101 –105, june 2011.

[71] E. Vittoz, "Future of analog in the vlsi environment," in *Circuits and Systems, 1990., IEEE International Symposium on*, pp. 1372 –1375 vol.2, may 1990.

[72] L. Brooks and H.-S. Lee, "A zero-crossing-based 8b 200ms/s pipelined adc," in *Solid-State Circuits Conference, 2007. ISSCC 2007. Digest of Technical Papers. IEEE International*, pp. 460 –615, feb. 2007.

[73] B. Murmann, ""ADC Performance Survey 1997-2011, Available: http://www.stanford.edu/ murmann/adcsurvey.html,."

[74] C.-H. Yang and D. Markovic, "A 2.89mw 50gops 16x16 16-core mimo sphere decoder in 90nm cmos," in *ESSCIRC, 2009. ESSCIRC '09. Proceedings of*, pp. 344 –347, sept. 2009.